Compressive Properties of Aramid Fabrics

David Luís Tomaz da Costa Campos

Thesis to obtain the Master of Science Degree in

Mechanical Engineering

Supervisors: Prof. Pedro Alexandre Rodrigues Carvalho Rosa
Eng. Afonso José de Vilhena Leitão Gregório

Examination Commitee

Chairperson: Prof. Rui Manuel dos Santos Oliveira Baptista
Supervisor: Prof. Pedro Alexandre Rodrigues Carvalho Rosa
Members of the Commitee: Prof. Luís Manuel Guerra da Silva Rosa
Prof. Maria Alexandra Sousa Rodrigues

October 2020

Agradecimentos

É com enorme prazer que expresso os meus profundos agradecimentos a todos os que contribuíram de alguma forma para a realização da presente dissertação de mestrado de engenharia mecânica, assim como para o meu desenvolvimento profissional e pessoal durante estes meses de trabalho.

Em primeiro lugar, ao meu orientador, o Professor Pedro Rosa, pelo incansável apoio, motivação e compreensão durante todo o decorrer da tese que foi essencial para toda a enorme aprendizagem e desafios que me foram proporcionados. Assim como o fornecimento de todos os equipamentos e estrutura que foram imprescindíveis ao desenvolvimento deste trabalho.

Agradeço, também, ao meu Co-orientador, o Engenheiro Afonso Gregório, pelo apoio e boa disposição demonstrando-se sempre disponível a ajudar em qualquer tarefa que sentisse dificuldade ou que necessitasse.

Queria deixar um agradecimento especial ao Pedro Santos, pelo seu apoio e admirável paciência que teve ao longo de todos os meses de trabalho e desenvolvimento da dissertação, disponibilizando sempre tempo para me ensinar e ajudar naquilo que fosse preciso. Salientando, igualmente, o seu incentivo para o bom companheirismo e entreajuda dentro do Laboratório de Maquinagem e Micro Fabrico (LabM3).

Ao técnico do laboratório de tecnologia mecânica, Sr.Farinha, por todo o auxílio prestado e tempo dispensado na maquinagem de peças necessárias. Assim como a todos os elementos técnicos do Núcleo de Oficinas (NOF), pelo apoio prestado a etapas do trabalho que não eram possíveis sem o seu contributo.

A todos os meus colegas de laboratório que se mostraram muitas vezes solidários contribuindo de forma incondicional para o desenvolvimento do trabalho.

Um agradecimento especial aos meus Pais, por todo o inesgotável amor e apoio incondicional durante estes meses de trabalho (tal como em todas as outras etapas da minha vida).

Por último, mas não menos importante, agradeço toda a paciência, amor e carinho singulares da minha namorada, Raquel Figueira.

Institutional Acknowledgements

This work was supported by FCT, through IDMEC, under LAETA, project UIDB/50022/2020.

The project MAMTool entitled “Machinability of Additive Manufactured Parts for Tooling Industry” funded by the Programa Operacional Competitividade e Internacionalização, and Programa Operacional Regional de Lisboa funded by FEDER and National Funds (FCT) is acknowledged (Reference PTDC/EME-EME/31895/2017).

Fibrenamics for supplying the aramid fabric samples.

Laboratory of Machining and Micro Manufacturing, Instituto Superior Técnico, for proposing the theme of this dissertation and for performing the laboratorial experiments analysed in this work.

Co-financed by:

Resumo

Este trabalho tem como objetivo desenvolver um método que permita caracterizar o comportamento do material textil presente num colete à prova de balas quando sujeito a forças de compressão. Para tal, é necessária a montagem de uma máquina que permita realizar ensaios de compressão dinâmicos a alta velocidade.

O foco deste estudo é identificar quais os melhores parâmetros que se adequam ao tecido de aramidas a ser testado, sendo de destaque o uso de aramidas impregnadas com STF (*Shear Thickening Fluid*) no tecido com o objetivo de aumentar a sua capacidade de absorção de energia ao impacto. Há que ter em conta que quando se dá o impacto, parte da energia é absorvida pelo colete, energia dissipada, e outra parte é transmitida através deste, chamada de energia remanescente ou residual que é a detetada pelo sensor de célula de carga da máquina. Deste modo, o plano de ensaios experimentais passa pela variação dos parâmetros da velocidade de impacto e o número de camadas em tecido de aramida seco e impregnado apurando a melhor relação para a capacidade de absorção de energia.

Os resultados mostraram que o número de camadas provou ser um importante fator contributivo para a capacidade de absorção de energia do tecido aramida até certa extensão. Enquanto os aramidas impregnados apresentaram valores de energia residuais inferiores aos das aramidas secas, para o mesmo número de camadas, o que implica que as aramidas impregnadas têm uma capacidade de absorção de energia superior ás secas.

Palavras Chave

Aramida, impacto, energia residual, Hopkinson

Abstract

This work aims to develop a method that allows characterizing the behaviour of the textile material present in a bulletproof vest when submitted to compression loads. To do this, it is necessary to assemble a machine that allows dynamic compression tests to be carried out at high strain rates.

The focus of this study is to identify the best parameters that fit the woven aramids to be tested, particularly the use of impregnated aramids with STF (Shear Thickening Fluid) in order to increase its energy absorption capacity to impact. It should be taken into account that when the impact occurs, part of the energy is absorbed by the fabric material sample, called dissipated energy, and another part is transmitted through this, called the residual energy, the one detected by the load cell sensor of the machine. Thus, the plan of experimental tests goes through the variation of the parameters of the impact velocity and the number of layers in dry and impregnated aramid fabric, in order to determine the best arrangement for optimal energy absorption capability.

The results showed that the number of layers proved to be an important contribute to the energy absorption capability of the aramid fabric until certain extend. While the impregnated aramids displayed inferior residual energy values than the dry aramids, for the same number of layers, which implies that the impregnated aramids have a higher energy absorption capability than the dry ones.

Keywords

Aramid, impact, residual energy, Hopkinson

Contents

List of tables

List of figures

Abbreviations

AEP - Allied Engineering Publication

BFS - Back Face Signature

CAD – Computer Aided Design

CNC – Computer Numerical Command

DAQ – Data Acquisition

GOST - gosudarstvennyy (state standard or governmental standard of Russia)

HSS - High Speed Steel

IBA – Interceptor Body Armor

IST – Instituto Superior Técnico

LED - Light-Emitting Diode

MTV - Modular Tactical Vest

NATO - North Atlantic Treaty Organization

NIJ - National Institute of Justice

NOF - Núcleo de Oficinas

PASGT - Personnel Armor System for Ground Troops

SHPB – Split-Hopkinson Pressure Bar

STANAG - Standardization Agreement

UV - Ultra Violet

STF – Shear Thickening Fluid

Nomenclature

σ - Stress

ε - Strain

F – Applied force

A_i – Instantaneous area

h - Final height

h_o – Initial height

h_i – Instantaneous height

d_i – Instantaneous diameter

d – Final diameter

A_o – Initial Area

c_t – Transverse wave propagation speed

ε_p – Elasticity limit strain

σ_p – Elasticity limit stress

ρ – Specific mass

E_c – Kinetic energy

m - Mass

v - Velocity

A_p –Projectile area

m_d – Mass per unit of vest area

m_p – Mass per unit of projectile area

V_{50} - Speed at which the projectile hits the target with a 50% probability of drilling it

V_0 - Speed with which the projectile hits the target, piercing it but exiting with a zero velocity

E – Young Modulus

$\dot{\varepsilon}_S$ – Test body deformation rate

ε_S – Deformation of the specimen

L_S – Thickness of the specimen

A_S – Area of the specimen section

1. Introduction

The evaluation of the performance of shields is extremely important to ensure the safety of the user in the most diverse activities, both military and civilian. However, this information is often confidential because of the risk it poses to military and civil society, and/or by strong economic interests on the part of companies selling this protective equipment. When performed, this evaluation is generally restricted to purely qualitative aspects, such as the solely verification of the damage produced by the projectile.

This work will focus on the study of the mechanical impact behaviour of bulletproof vests fabric materials, namely plain-woven aramids when subjected to a dynamic compression test transverse to the direction of the fibers in order to simulate the impact of a ballistic projectile. The development of an impact test method, that allows characterizing bulletproof vests woven materials, has a real practical interest in the military economic sector. Since the most common methods practiced today, regarding the quality of vests, go by real firearms in one of the vests of the set making it obsolete from a functional point of view, which does not provide an accurate, precise and scientific conclusion of the vests material quality.

The structure of the dissertation is divided into 5 chapters, being this introduction the first one.

Chapter 2 depicts the state of the art and characterization of materials used in ballistic vests, more precisely aramids, as well as ballistic impacts, shield quality standards, tests and methods used to characterize them and theories and laws present in the literature that are relevant in the development of this study. Finally, it is explained the principle of assembly and operation, and evolution at Instituto Superior Técnico (IST), of the split-Hopkinson pressure bar, which ends up forming the bridge to the experimental development of this thesis.

Chapter 3 describes the entire assembly process of the impact-testing machine, including the function of its various components, as well as the justification for its use, the processes through which it has undergone throughout its design to its final function, and how the relationship between them makes the functionalities of the machine possible.

Chapter 4 displays the experimental results obtained through a variety of tests carried out on dry and impregnated aramid fabrics for different impact velocities and layer stacks in order to determine the optimal energy absorption capability by comparing with the residual energy detected.

Finally, chapter 5 focuses on the conclusions of this study. It also mentions the prospects for future work, i.e., details to be changed in order to improve the efficiency of the machine, as well as possible ideas that allow addressing some of its limitations and flaws.

2. Ballistic Armours

This chapter aims to describe the ballistic principles, the characteristics of the textile materials used in ballistic vests as well as their mechanism. In addition, the methods of ballistic evaluation used and the principles of the split-Hopkinson pressure bar.

2.1. Ballistics

It is relevant to mention the importance of understanding physics behind a shooting of a projectile. Ballistics is the field of mechanics concerned with the launching, flight behavior, and impact effects of projectiles. These field of study is subdivided into four: (i) Internal ballistics, the study of the processes that originally accelerate the projectile; (ii) Transition ballistics, the study of projectiles as they transition to unpowered flight; (iii) External ballistics, the study of the passage of the projectile (the trajectory) in flight; (iv) Terminal ballistics, the study of the projectile and its effects as it ends his flight (U.S. Army, 1965).

Since the experiments are executed in a controlled environment, in which the only event of interest is the impact of the projectile with the specimen, the only subfield to take in consideration is the terminal ballistics. As it was mentioned before, common factors in this subfield include projectile weight, composition, velocity, and shape.

2.1.1. Terminal Ballistics

When the projectile reaches its target, there are high rates of deformation. The high speeds involved induce a localized behaviour where the compressive stress waves created [Zukas, 1982] propagate. It is important to stress the importance of ballistic protection to absorb as much kinetic energy from the projectile as possible.

In order to understand the behaviour of the materials affected by the projectiles, it is sought to characterize the impacts as being high or low speed. Therefore, in order to define this characterization, the following classifications are assigned [Morais, 2011]: (i) Low-speed impact: $v < 250$m/s; (ii) High-speed impact: 500m/s $< v <$ 2000m/s; (iii) Impact on hyper speed: $v >$ 2000m/s.

When considering the interval between 500m/s and 2000m/s, the response of the structure as a whole respond to the impact locally, thus having little relevance in the study of the impact. The structure for this speed range responds to the impact locally, this means that only a small area around the impact zone will offer resistance and take damage.

When the impact speed is greater than 2000m/s and less than 3000m/s, the material has the approximate behaviour typical of fluids, and local pressures would cause tensions higher than the

resistance of the materials considered. If we consider speed higher than 12000m/s will occur the vaporization of the materials at the time of the collision. [Morais, 2011].

Of course, the projectile speed parameter is not sufficient to describe the impact response. It is necessary to know the properties of both projectile and target materials, as well as temperature and other ambient conditions [Justo, 1996].

In order to impose a limit on the target-projectile pair with regard to its penetration, there is some controversy among several researchers in what is called "ballistic limit", however, there are two accepted definitions in the scientific community that identify this limit: (i) The V_0 speed defines ballistic limit as the speed at which the projectile hits the target, piercing it, but exiting with a zero velocity [Morye, 2000]; (ii) V_{50} defines the velocity at which the projectile hits the target with a 50% probability of drilling it [Silva, 2005].

2.1.2. Impact in Textiles

The amount of fiber used in a textile is a determining factor in the impact, since it plays a structural role in shielding. The composites that have fibers closer to each other and with less space between them are the ones that have the highest value of fiber volume fraction in the laminate. For larger volume fractions, the stresses applied on the composite are distributed more evenly and the performance of the component mechanically is superior due to the loads that have been transferred to the fibers, explaining why a modulus of superior tensile strength [Pereira, 2017].

The increase of the amount of fiber is not always synonymous with increased strength of the material and it tends to decrease in value when the binomial between the fiber and the resin is no longer balanced. That happens whenever the resin ceases to facilitate the correct union between the fibers, this phenomenon is visible when the tensile strength begins to decrease in value.

In matrices with a low volume fraction of fibrous material, in which the space between fibers is very significant it is normal to observe that the matrix presents localized deformations and that these tend to promote the rupture of the fiber matrix bond [Crouch, 2017].

As already explained, the dimensions, the volume fraction and the distribution of fibers in the composite are parameters that influence its performance. It is also necessary to take into account the continuity or discontinuity of the fibers. While continuity provides greater impact resistance and dimensional stability, discontinuous fibers are easier to produce at lower costs [Carr and Crawford, 2016].

Not only the volume fraction and continuity, but also one of the important factors to consider in the impact analysis is the orientation of the fibers. The orientation of the fibers in the matrix can be aligned or random, depending on what is intended at the level of the project, the fibers are chosen to be requested to effort preferably along their length. It can even be said that anisotropy grows more significantly with increasing length and increasing the volume fraction of fiber. Depending on how the fibers are oriented, the mechanical properties of this same fiber may be larger or smaller. [Pereira, 2017].

A composite material is the union of two or more materials. In the case of fibers, they are fixed to a polymeric matrix characterized by low density, thermal stability and resistance, promoting better mechanical strength, toughness and rigidity to the structure of the new formed material. At the border in the resin, which connects the two parts and the fiber is where the transfer of loads occurs, an area called the interface, and it is crucial that there is a good adhesion [Duarte, 2019].

During an impact on a target composed of a fibrous material, the fibers of the ballistic panel are subjected to stresses applied by the projectile. The fibers directly affected by the projectile are named after primary fibers responsible for offering resistance to penetration and, therefore, are subjected to the highest stresses, even reaching the rupture stress.

Near the impact area are secondary fibers that suffer deformations, generally lower than the deformations of the primary fibers, not reaching the rupture, dissipating some energy. Due to the projectile's high speeds, ballistic impact is a phenomenon with localized effects that does not affect the entire structure of the panel, hence the area of secondary fibers being restricted to a small radius around the point of impact. This radius will be equal to the distance reached by the deformation waves that are created on impact. Figure 2.1 shows a representation of the event of a ballistic impact in which it can be seen in red the primary fibers and in light blue the area corresponding to the secondary fibers [M.Pasquali, 2015].

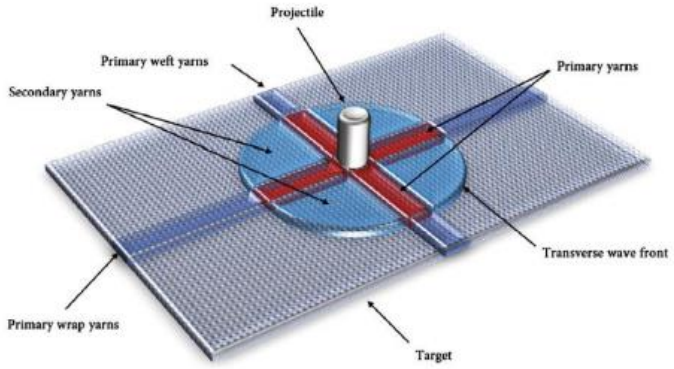

Figure 2.1 - Identification of primary and secondary fibers during a ballistic impact [M.Pasquali, 2015].

In relation to the energy available during the impact, the law of energy conservation dictates that the energy of an isolated system remains constant over time; in other words, energy is not destroyed nor created, only transformed. In the case of ballistic impact, in the target projectile system, the target through various phenomena absorbs the energy carried by the projectile. When the target absorbs all the energy of the projectile, preventing its penetration, it turns out that this kinetic energy is converted into plastic deformation and heat [Santos, 2016].

Within many studies conducted in this area, Smith (1958) took important steps to understand the behaviour of fibers subjected to transverse impacts. In their work, the authors study the stress-strain relationship of a fiber subject to a rapid impact, trying to understand the effect of waves that propagate along the fiber. The authors discuss the propagation of plastic, elastic and transverse waves, establishing equations for their velocities. In particular, the study developed in the understanding and

characterization of the transverse wave created important foundations for further studies in the area of impact at high speeds. The equation (2.1) is the expression used to calculate the velocity of the transverse wave, fundamental to calculate the area affected by the impact and displacements caused on the target [Santos, 2016].

$$c_t = \sqrt{\frac{(1+\varepsilon_p)\sigma_p}{\rho}} - \int_0^{\varepsilon_p} \sqrt{\frac{1}{\rho}\frac{d\sigma}{d\varepsilon}} \tag{2.1}$$

Where c_t is the transverse wave velocity, ε_p the elasticity limit deformation, σ_p tensile stress limit and ρ the volume mass of the material. Figure 2.2 illustrates the directions of strains in ballistic impact.

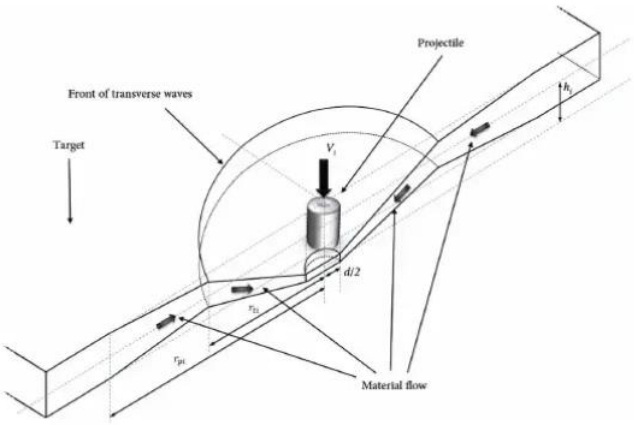

Figure 2.2 - Effects caused by the transverse wave on a fiber. After suffering deformations caused by plastic and elastic waves, the material is pulled to the point of impact by moving transversely [M.Pasquali, 2015].

2.2. Balistic Vests

With the development of firearms and new ways to harm and injure humans, ballistic vests have incorporated various types of materials that play a specific function within the set. The new types of protection are made up of composite materials due to their high strength and/or stiffness in relation to their weight, and a good tolerance to damage [Nayak, 2013][Zhang, 2014]. Bulletproof vests (figure 2.3) are intended to protect the wearer against projectiles of various shapes, sizes and impact velocities [Adanur, 1995]. Aramid and ultra-high molecular weight polyethylene are used extensively as base materials for ballistic vests. These high performance fibers are characterized by high strength, high energy absorption, and low density [Govarthanam, 2016].

Since ballistic vests textile materials are the central product of this study, it only makes sense to present a brief definition of the product they constitute and its historical development.

Figure 2.3 - Example of bulletproof vests of aramid fibers with ceramic plates.

2.2.1. History

The choice of ballistic protection must always be combined with the type of threat to be faced and the user's operability. This means that to improve the efficiency and effectiveness of an armour, it is necessary to make a prior analysis of the threats that will be faced. This notion that interconnects ballistic protection, threat and operability is easily observed through a historical review of the evolution of the personal protections of soldiers [Santos, 2016].

The Greek Hoplites, the most advanced infantry of antiquity, were equipped with helmet, body armour and a shield (hóplon) made of bronze or leather. At the time, this type of armour was effective due to the fact that battles were melee, with short swords or spears, where the shield became very useful. The Roman legion wore a type of segmented armour consisting of overlapping iron bands connected to each other with leather straps that, when not an entire piece of iron, allowed the user to have greater mobility. In the Renaissance, the helmet and medieval steel armour fell into disuse because they were inefficient against the firearms that were beginning to appear [Santos, 2016].

In the second half of the 20th century, new materials appeared because of technological advances. Nylon began to be used in conjunction with other materials to obtain a flexible solution, allowing a reduction of lesions in the pectoral and abdominal area. In 1965, it was developed by chemist Stephanie Kwolek in the company DuPont, known for the fabric Kevlar®, a registered trademark (often confused with a type of material), a type of synthetic fiber of aramid very resistant and light (*DuPont on Kevlar*). This type of fabric is effective against low caliber weapons, but cannot protect against high caliber weapons without the support of a metal or ceramic plate [Bernardi, 2003]. Kevlar® demonstrates superior performance to the materials used so far and is currently used in ballistic applications such as shields, helmets and bulletproof vests. Despite its excellent mechanical properties, Kevlar® itself is ineffective against high caliber projectiles, so there is interest in the development of ceramic inserts applicable to bullet vests. These plates inserted in the vests, similar to what was tried during World War II with the plates made of steel, seek to protect vital parts of the human body and are applied mainly in the abdominal and pectoral area. Application of these plates has become possible due to the fact that

the ceramics currently used have a much lower weight than steel, facilitating their adoption by the infantry [Yang, 1993].

Of course, conventional vests that protect the long range have evolved over time to bridge the flaws of their predecessors such as PASGT (Personnel Armor System for Ground Troops), used in the early 1980s by the United States Army, replaced by IBA (Interceptor Body Armour) in the 2000s with additional protections in parts of the body other than just the thorax, which was then replaced by MTV (Modular Tactical Vest) in 2006, etc. [Pike, 2017].

Besides the focused characteristic of the vests material for this study being the ability to absorb the impact energy of projectiles, it should be bore in mind that the weight and "adaptability" of the vests to the human body is also important. As such, the selection of materials is essential (CBC Defense - Military Ammunition).

2.2.2. Characteristics

When a handgun bullet strikes aramid bulletproof vest, like in figure 2.4, it is caught in a "web" of very strong fibers. These fibers absorb and disperse the impact energy that is transmitted to the vest from the bullet, causing the bullet to deform. Each successive layer of material in the vest absorbs additional energy, until the bullet has been stopped [Malik, 2018].

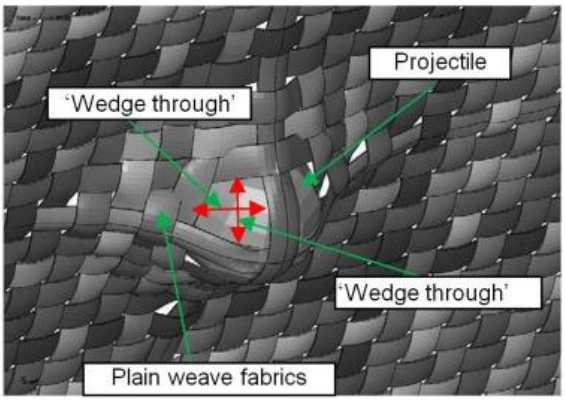

Figure 2.4 - Trapping of ballistic projectile by the plain weave fabrics and ''wedge through'' creation during ballistic impact [Cheeseman, 2003].

The level of ballistic protection is entirely linked to the threat level to be faced. However, it can be stated that there are a number of necessary characteristics common to all materials, regardless of the desired level of protection. One of the most important properties for a ballistic material is its tenacity, which indicates the energy that the material can absorb before rupture. In the case of the ballistic impact of a phenomenon of energy transfers, it is crucial that ballistic material has a high tenacity [Moura, 2011].

The ballistic performances measurement such as energy absorption, trauma values, failure mechanism and ballistic limit velocity of the materials are also affected by the projectile conditions including projectile mass and size, projectile impact trajectory and angle of impact, projectile shape and geometry, projectile nose angle, projectile velocity, etc. [Abtew, 2019].

Out of this list of characteristics, it is relevant to highlight the projectile shape and geometry, like the nose angle, and the angle of incidence in the impact area.

According to research made by Talebi (2009), eleven different models were built with nose angle of the projectile ranging from 30° to 180° with the difference of 15° as shown in figure 2.5 (a). The energy absorption trends were sectioned in four regions by which failure mechanisms and its ballistic resistance are recorded differently in each region, figure 2.5 (b) [Talebi, 2009].

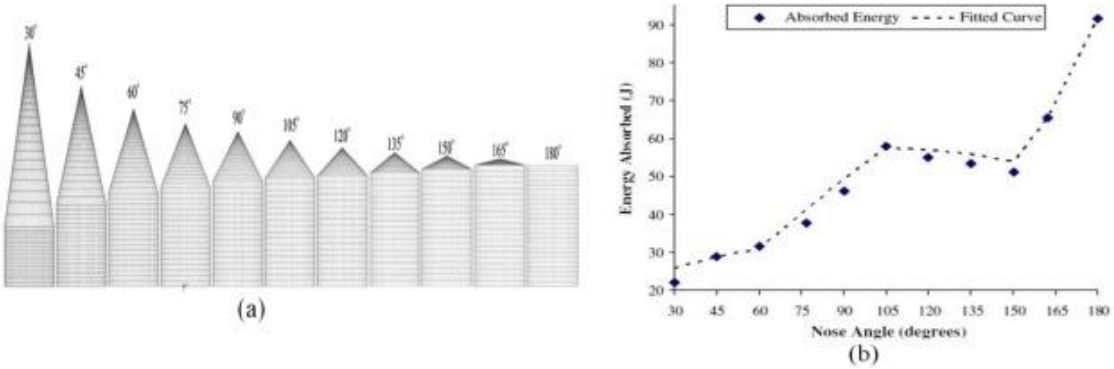

Figure 2.5 - (a) Front view of the conical projectiles with different nose angles and, (b) Energy absorption as a function of nose angle [Talebi, 2009].

In this study, for simplicity of the experiments, the nose angle is maintained at 180º for all the projectiles maximizing the energy absorption, according to the results of the graph on figure 2.5 (b).

Obliquity of projectile is also another projectile condition, which affects the overall ballistic performance and mechanisms of the materials.

One study focused on a change in obliquity of the projectile using wave theory and energy balance analytical model based on the material behaviour just after impact and its surface condition during the ballistic impact. During the study, the researcher considered different energy absorbing mechanisms such as compression in the region surrounding the impacted zone, compression of the target directly below the projectile, tension in the layers, compression in the lateral direction, shear plugging, friction, matrix cracking and delamination. The figure 2.6 represents those mechanisms.

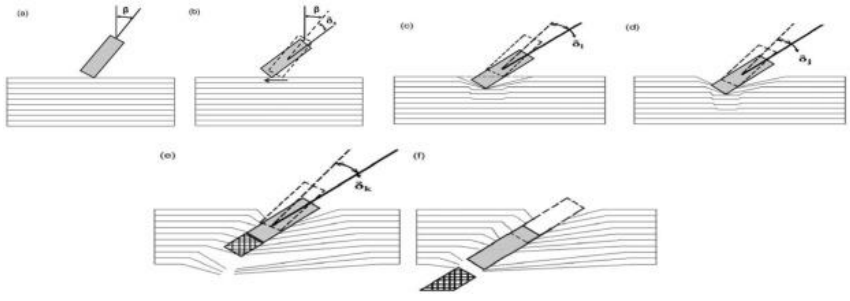

Figure 2.6 - Schematic of an oblique ballistic impact: (a) impact, (b) slipping, (c) compression, (d) penetration, (e) total failure and (f) perforation [Rajagopal, 2014].

While impact test, obliquity can be created in two ways as shown in figure 2.7 (a) and (b). The basket aramid laminates show greater ricochet angle (>75°) than metallic ballistic plate (60°) and possibly lower than plain weave aramid lamination.

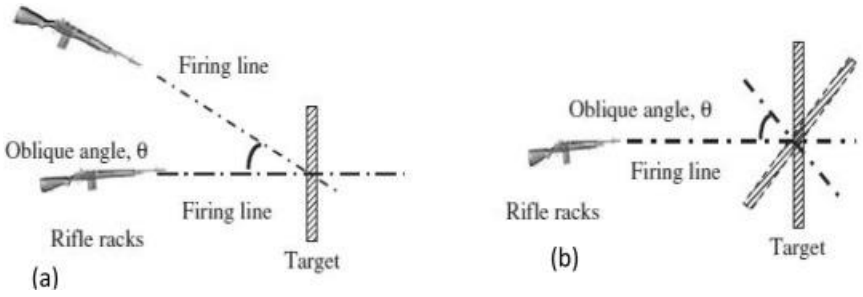

Figure 2.7 - Oblique developing methods (a) Change of firing line, and (b) changed angle of the impact surface [Chu, 2007].

It is important to note that soldiers, during missions, carry a lot of weight in equipment (weapons, ammunition, transmissions, supplies, etc.). Thus, it is necessary that protective equipment be made of light materials. The specific weight is an important factor in the choice of material, which should also have a high stifness and good mechanical strength. These mechanical properties are difficult to reach simultaneously using traditional materials. However, composite materials allow the achievement of balance of these properties, and therefore their application in protective equipment is very attractive [Kumar and Ahmad, 2013]. Once the necessary characteristics of a bulletproof vest are established, it is sought to select the materials with the most suitable properties to comply with these requirements.

2.2.3. Materials

Nowadays, high-performance fibers are typically used in the form of woven, non-woven fabrics or woven or non-woven reinforcements for different ballistic protective applications including ballistic vests. However, in the ancient time, materials such as animal skin, leather and even silk were also used in combination with metal plates in body armour systems to deliver the required protection until the Korean War [Wittman, 1967].

The development of such ballistic materials from high-performance fabrics will greatly depend on high tenacity yarns made from fibers with high modulus, high strength, and excellent anti-degradation traits [David, 2009].

Thanks to the dedicated researchers and companies, now it is possible to fulfil these requirements through using high performance fibers/matrices and layered different type of textile structures such as two-dimensional (2D) and three-dimensional (3D) preforms [Abtew, 2009].

2D Plain weave fabric is the simplest and commonly used 2D woven structure fabrics in the ballistic applications. It is produced by interlacing the two types of yarns, namely yarns run along the length of the fabric (warp) and yarns that run from selvedge to selvedge (weft) based on the predefined checkerboard pattern [Abtew, 2009].

For protection against ballistic projectile or combined threat type, soft vests made of 3D orthogonal woven, 3D angle interlock woven and 3D fully/partly interlaced woven as well as multi-axis 3D woven or knitted preforms have been employed [Bilisik, 2013].

Over the years, it was sought to create a bulletproof vest that could stop projectiles of firearms from both low (i.e., handgun) and high caliber (i.e., carbine). Ballistic Nylon (until 1970) or Kevlar®, Twaron®, Dyneema® or Spectra® (both competitors of Kevlar®) or polyethylene fiber are the most chosen synthetic fibers to manufacture bulletproof vests in the market. The vests from the seventies were made of ballistic nylon and complemented with fiberglass plates, steel, ceramics, titanium and ceramic and fiberglass composites, the last one being the most effective (Forgotten Weapons). In this work we will focus, as stated earlier, on aramid fibers, more specifically Kevlar®.

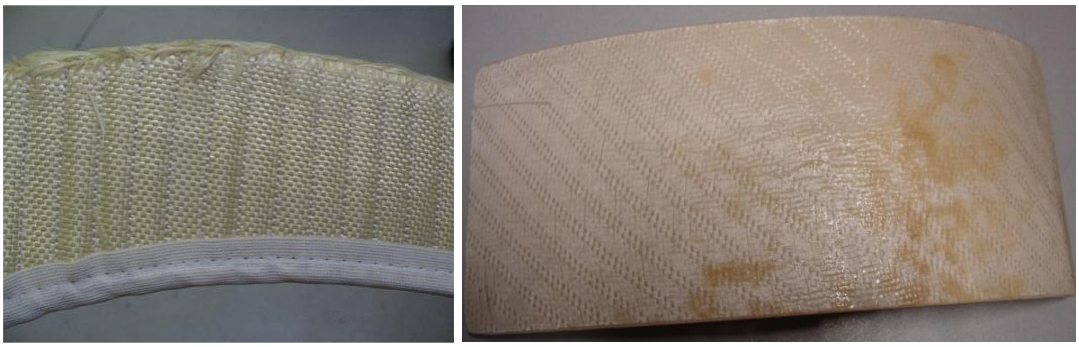

Figure 2.8 - Flexible aramid fiber structure (left) and ceramic tactical plate (right) [Monteiro, 2007].

2.3. Aramids

Aramid fibers belong to the family of synthetic fibers (produced by man through chemical synthesis). Inside the polymers, it consists of a polyamide fiber (of the same nylon family) with carbons in aromatic rings (figure 2.9), hence the name aramid (*aromatic amid*). The chain of molecules of this polymer consists of starch groups (CO-NH) that are strongly aligned according to the axis of the fibers resulting in a greater contribution of chemical bonds to the stifness and mechanical strength of fibers, highlighting them from other synthetic fibers (*Dupont – Kevlar® Techincal Guide*).

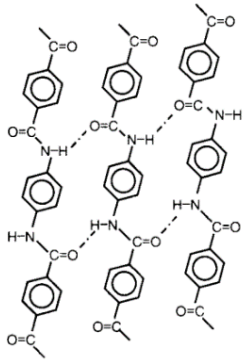

Figure 2.9 - Molecular chain scheme of aramide fibers.

This transfer of stresses between molecules of the same chain is very efficient due to the hydrogen bonds between them making it possible to obtain relatively low molecular weight chains.

Liquid crystal polymer solutions exhibit a unique behaviour when subjected to shear forces. When the solution passes through a spinning plant (or orifice), the molecules, with random directions, are completely oriented in the direction of the cut arising with perfect molecular orientation.

This supramolecular structure is preserved, almost completely, in the structure of the filament due to a relaxation of the orientation of the induced cut. This process proved to be an innovative and low-energy way to guide polymer molecules reaching very resistant fibers (*Dupont Kevlar® Aramid Fiber* – Technical Guide).

2.3.1. Properties

In addition to its excellent mechanical properties with regard to the performance of its function, such as high stress of transfer and rupture tension and low volume mass, it is also important to mention its properties in other branches.

As far as chemical property is concerned, all aramids contain hydrophilic amide bonds, which makes them vulnerable to high humidity environments. Although it varies greatly between products manufactured from aramids, some may be more resistant to organic solvents than others, however strong acids can cause significant mechanical resistance losses in most of these products. The degradation of Kevlar® fibers can occur when exposed to very acidic or basic solutions, i.e, the further away pH value is from 7, the greater the loss of fracture thoughness, and more acidic solutions cause greater loss than basic when equally distant from pH 7, as is notorious in figure 2.10.

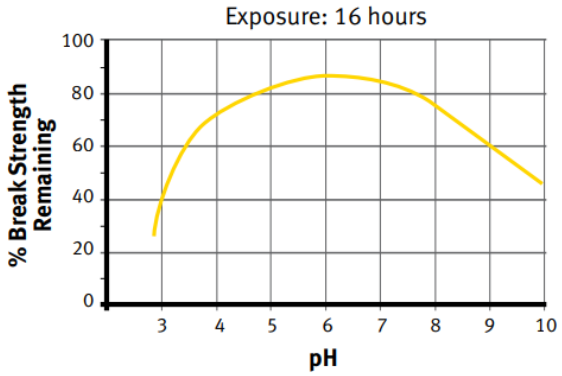

Figure 2.10 - Hydrolytic stability of Kevlar® in water vapor at 154ºC exposed for 16 hours vs pH of water (Kevlar® Aramid Fiber – Technial Guide). Breaking Strength is the term used in the English literature to define the force needed to be applied in order to fracture a particular material.

Also having high levels of triglycerides (derived from the combination of glycerol with acids), it becomes a difficult task to paint products with aramid fibers. The aromatic nature, creating cyclic chemical structures, is responsible for oxidative reactions when exposed to Ultra Violet rays (UV radiation) that leads to a change in color and also loss of mechanical resistance [Fink, 2014].

Aramid fibers are known to have high heat resistance. These do not behave in the conventional way but decompose rather at high temperatures when tested with a temperature increase of 10ºC/min. The decomposition temperature varies with the increase in temperature by time and the duration of fiber

exposure under these conditions. The weight variations of Kevlar® fibers with the increase in temperature vary differently depending on the surrounding substance in which it is found. Figure 2.11 shows thermogravimetric analyses of Kevlar®49 in different atmospheres with temperature increase of 10ºC/min (Dupont Kevlar® Aramid Fiber – Technial Guide).

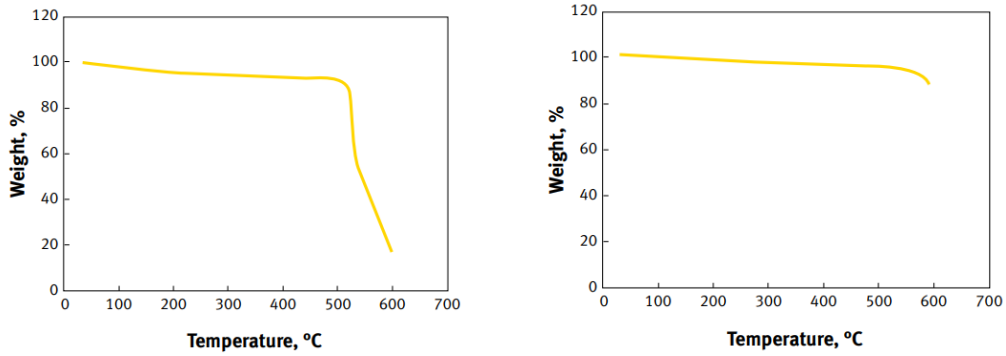

Figure 2.11 - Mass loss of Kevlar®49 with temperature increase at 10ºC/min exposed to a) Air and b) Nitrogen (Kevlar® Aramid Fiber – Technial Guide).

By observing the graphs, it is verified that in air, from ~500ºC, Kevlar®49 fiber abruptly loses mass in percentage, while in nitrogen this loss is almost negligible. These studies by DuPont conclude that not only the type of fiber used and the temperature growth but also the surrounding atmosphere influence the percentage variation of fiber mass in its degradation when exposed to high temperatures. Specific heat, an important thermal property to consider, also varies with temperature as shown in figure 2.12.

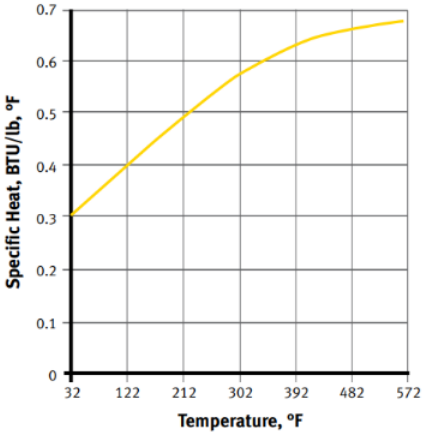

Figure 2.12 - Specific heat variation with the temperature variation of Kevlarfiber®49 (Kevlar® Aramid Fiber – Technial Guide).

There is easily an increase in the specific heat of this fiber with the temperature with a more gradual growth around 0.7 BTU/lb.ºF (2930.758732 J/(Kg.C)) at 572ºF (~300ºC). Finally, a study by DuPont was also carried out that demonstrates the variation of the mechanical properties of some types of fibers influenced by temperature. Figure 2.13 (a) and (b) show the variation of the breakage stress and Young modulus with the temperature for different conditions, respectively.

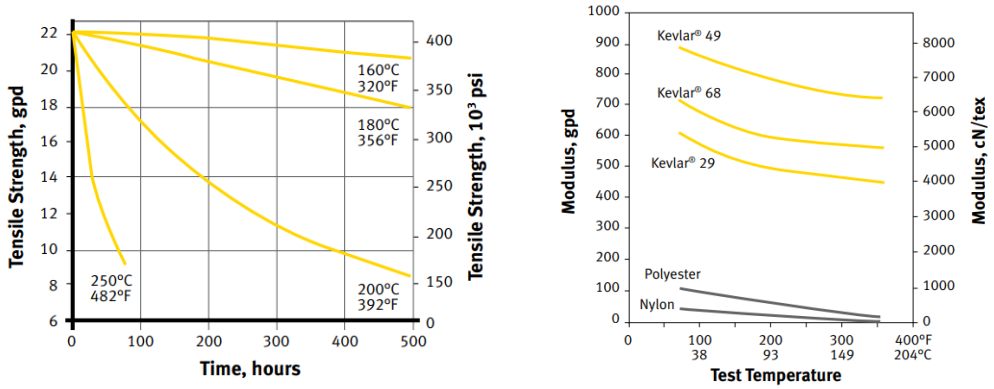

(a) (b)

Figure 2.13 - (a) Variation of breakage stress over time for different temperature values of Kevlar fiber®29; (b) Variation of the Young modulus with temperature for different types of Kevlarfiber® Nylon and Polyester exposed 5 minutes to these temperatures (Kevlar® Aramid Fiber – Technial Guide).

Figure 2.13 (a) concludes that the rupture stress varies more violently over time the higher the temperature. In figure 2.13 (b), despite a large difference in values between fibers, the decrease in the Young modulus with temperature is crosswise identical to all fibers under study. Many of the military missions carried out today are in middle eastern countries where, unlike very hot summers, winters reach negative temperatures of -10ºC including snow, and even lower in mountainous regions (very common in countries such as Afghanistan, Iran, Tajikistan, etc.) where the altitude is higher. These conditions require that vests developed from Kevlar fibers® keep their characteristics within what is physically possible.

Comparing, in table 2.1, the mechanical properties of Kevlar fiber®29 between ambient temperature and arctic temperatures (-46ºC) there is an increase in rupture stress and Young modulus and a decrease in extension.

Table 2.1. Values of mechanical properties inherent to Kevlar fiber®29 at room temperature and artic temperature (Kevlar® Aramid Fiber – Technical Guide).

Property/Temperature	25ºC	-46ºC
Breaking tension (MPa)	2430	2510
Modulus of Elasticity (GPa)	53,9	60,8
Deformation to rupture [1] (%)	4,1	3,9

With the variations at extremely low temperatures, it can be concluded that the lowest temperatures at which humans will need a bulletproof vest, variations in mechanical properties can be negligible to temperature below room temperature.

Regarding the stability of the dimension, Kevlar® fibers do not reduce their size when exposed to hot air or hot water as well as other organic fibers because the coefficient of thermal expansion has a very small negative value in the longitudinal direction, which makes its use possible in a greater versatility of environments.

[1] Maximum deformation before rupture.

Because the minimum oxygen concentration index is high in this polymer, it becomes difficult to combust. Studies have shown that some types of aramids submitted to 300ºC can retain up to 50% of their mechanical strength while remaining in elastic regime when under tension. The aramids also present high crystallinity, which results in negligible expansions at high temperatures.

Aramid yarn have yield traction stresses of the order of 103 Mpa, in other words, approximately five times more than ordinary steel, and when subjected to intense bending levels, present a nonlinear behaviour in the plastic deformation regime. Regarding fatigue stress, no failure is observed, even in conditions of high loads applied, or long cycle times.

It was, in fact, studied that aramid fibers can retain high levels of fracture resistance after fatigue loads compared with other fibers. Yamashita, Kawabata, and Kido (2001) studied stiffness loss by applying cyclic load to aramid fibers (both in compression and traction) and noting that the Young modulus of aramid fibers increases when they are subjected to a load to traction and decreasing when in compression. Figure 2.14 suggests these results [Abdin, 2015].

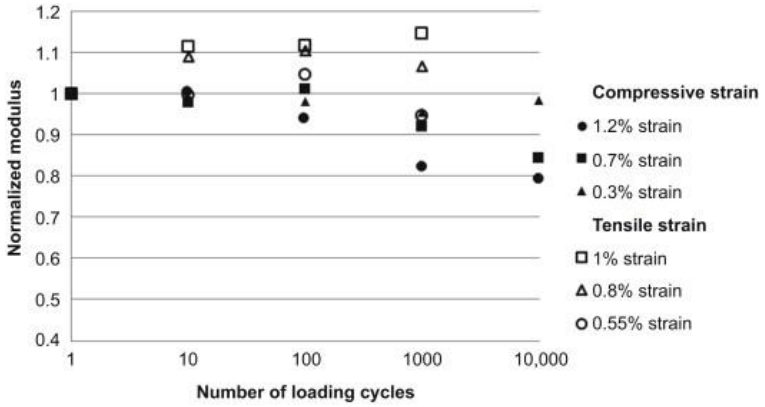

Figure 2.14 - Typical stiffness loss curves for aramid fibers during cyclic loading (Yamashita, 2001). The different behavior is observed during the cyclic load of traction and compression. There is a reduction of the module during compressive load, while there is observed during the cyclic load of traction and compression. There is a reduction of the module during compressive load, while there is an increase during elastic load [Abdin, 2015].

Minoshima, Maekawa, and Komai (2000) conducted a series of tests on a type of aramid fiber, also Kevlar® fiber 49, which proved to have excellent fatigue and relatively low negative slope properties on the S-N curve in log-log charts compared to base metals (see figure 2.15) [Abdin, 2015].

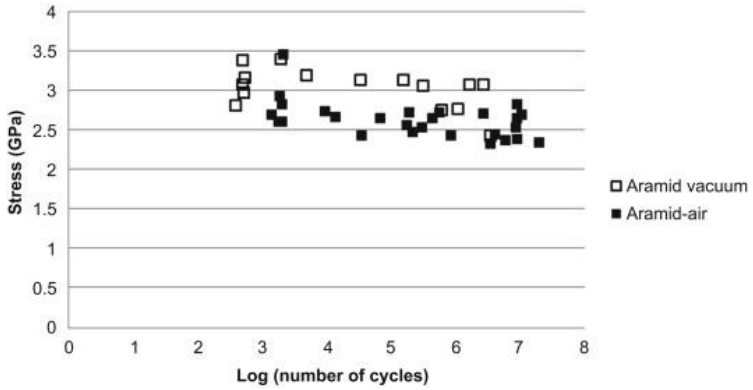

Figure 2.15 - The environment has a strong effect on the fatigue behavior of Kevlar® fibers. Minoshima et al. (2000) showed that the strength and shelf life of 'Kevlar49® ' fibers are significantly reduced when subjected to loading under ambient air conditions, as opposed to vacuum [Abdin, 2015].

In summary, the properties of aramids are known not only for their high mechanical resistance in relation to the stress of compromise, rupture, as well as when subjected to cyclic fatigue efforts with significant loads applied, but also for their resistance to corrosion and abrasion and absorption and organic solvents, providing it with good chemical resistance. They have negligible electrical conductivity and have a melting point of 350-500ºC depending on the aramid fiber product (Kevlar®, Nomax®, etc.) which is relatively high for the functions of this polymer, being little flammable and very resistant to heat. They are, however, sensitive to acids and UV radiation [Abdin, 2015].

Despite very few disadvantages, the aramids absorb moisture with relative ease which leads to them being combined with an epoxy resin system (moisture resistant) creating a more complete composite material. For a qualitative and more detailed analysis of its characteristics with regard to numerical values, Kevlar® presents a range of values between its various fiber products, as shown in table 2.2.

Table 2.2. Properties within the various models of Kevlar® fibers (Kevlar® Aramid Fiber – Technical Guide).

Physical properties	**Density**	**1380 - 1470kg/m^3**
Mechanical Properties	Toughness	2920 - 3000Mpa
	Rupture stress	3620MPa
	Transfer stress	530MPa
	Young Modulus	70,5-112,4GPa
	Tensile Strength	3600MPa[2]
	Poisson Coefficient	0,36
	Fracture strain	3,6-2,4%
Thermal Properties	Specific heat	1,420J/Kg*K (25ºC) 2,010J/Kg*K (100ºC) 2,515J/Kg*K (180ºC)
	Thermal conductivity	0,04 (W/m*K)
	Air decomposition temperature	427-482ºC
	Temperature recommendation for long-lasting uses	149-177ºC
	Melting point	500ºC
Electrical Properties	Electrical conductivity	Has no electrical conductivity

This work focuses only on Kevlar® aramid fiber as general brand. Nevertheless, there are other homologous brands that, for comparison purposes, make sense to refer as their values of their properties as well as to distinguish between the two main types of Kevlar® fiber, 49 and 29, referring to the table in attachment A1.

The tests performed in this work are carried out on a split-Hopkinson pressure bar (explained in more detail in a previous section) based machine, which, despite the tests considered to be dynamic, are identical to conventional compression tests, so it is appropriate to highlight the characteristics of these tests and the behaviour of the tested materials.

[2] In conditions of impregnated epoxy system according to the norm ASTM D2343

The compression test, more precisely uniaxial between right plates, is one of the most used mechanical tests to obtain the stress-strain evolution of a given material. This consists of subjecting a cylindrical specimen to a compressive force, recording the measured force for each displacement increment. In order to measure the force and displacement parameters of the test is used in series with the plates a load sensor and a displacement sensor. Figure 2.16 outlines this type of experiments [Silva, 2005].

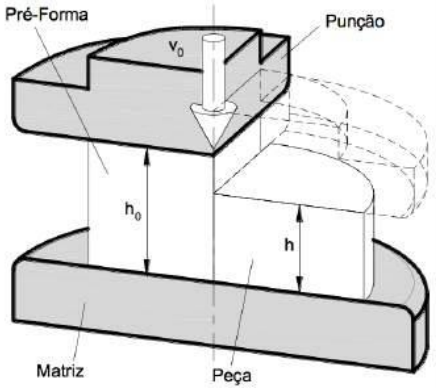

Figure 2.16 - Schematic representation: Uniaxial compression experiment [Silva, 2013].

True stress and strain are defined as expressed in equations (2.2) and (2.3), respectively:

$$\sigma = \frac{F}{A_i} \tag{2.2}$$

$$\varepsilon = -\int_{h_o}^{h} \frac{dh}{h} = ln\left(\frac{h_o}{h}\right) \tag{2.3}$$

Where F is the load applied by the plates, A_i the instantaneous area, h_o the initial height of the sample and h the final height.

Taking into account that the height of the specimen for each instant relates to the displacement, d_i through:

$$h_i = h_o - d_i \tag{2.4}$$

Due to the condition of incompressibility, the instantaneous area of the specimen is given by:

$$A_i = \frac{V}{h_i} = \frac{A_o h_o}{h_i} = \frac{\pi\left(\frac{d}{2}\right)^2 h_o}{h_o - d_i} \tag{2.5}$$

One of the main problems in compression tests is the appearance of a curvature on the lateral surface of the specimen. This phenomenon, called barrel effect, occurs due to the lateral sliding of the material that makes the plastic deformation not homogeneous. This curvature has the main origin in the friction present in the contact surfaces between the specimen and the compressor plates. In order to solve this problem, lubricant is generally applied to the surfaces of the specimen in contact with the plates in order to reduce friction between these two surfaces [Martins, 2005]. In this particular study, this

effect is not considered since the samples to be used are fabric material, therefore there is no need to apply lubricant.

2.3.2. Impregnated Textiles

As discussed earlier, these high performance fibers are characterized by high strength, high energy absorption, and low density. However, to meet the protection requirements for typical ballistic threats, approximately 13–50 layers of fabric are required, which results in a bulky and stiff armour. Although, the bulkiness limits its comfort and has restricted its application primarily to torso protection.

In order to reduce the bulk of the material, aramids can be impregnated with materials or powders with dilatant properties. The results demonstrate a significant enhancement in ballistic penetration resistance [Govarthanam, 2016].

A shear-thickening fluid (STF) is one of these materials [Lu, 2015]. Shear-thickening behaviour refers to a non-Newtonian fluid phenomenon, i.e., the viscosity increases with the shear strain rate. This behaviour is frequently observed in dense suspensions [Brown, 2010]. When nanoparticles are included in a suspension at high volume fractions, the suspended colloidal particles can form hydro clusters when subject to high shear stresses, leading to highly viscous and even solid-like behavior [Lee, 2003].

Shear thickening fluid (STF) impregnated fabrics offer improved ballistic performance against impacts, but the effect becomes not obvious at high impact velocity (e.g. 300 m/s) as reported by some [Lu, 2015].

The concept “liquid body armour” attracted much attention since its discovery [Lee, 2003], which is manufactured by impregnating shear thickening fluid (STF) into ballistic fabrics. STF is able to transfer from the initial liquid state to a near solid state under impact with the critical shear rate [Peters, 2016], which promotes impact energy distribution and dissipation. This transformation is reversible, i.e. the solidified STF will return to the liquid state when the load disappears. Accordingly, this feature of STF has been used to treat high performance fabrics aiming to enhance the performance against impact loading [Lu, 2015].

Many researchers have studied the ballistic resistance of STF impregnated fabric panels. For impact velocities below 300 m/s, the STF impregnated fabric panels were proven to have improved ballistic resistance and absorb more energy [Lu, 2015].

2.3.3. Applications

In order to understand the versatility of this composite, it should be noted that these fibers are also used in many other products in various branches besides the military, such as aeronautics and sport, among other material goods. These materials can be the most diverse from snowboards, tennis rackets, fiber optic cables, cut and heat resistant clothing, such as firefighter equipment, etc. Below, figure 2.17 presents some of the many practical examples of how aramid fibers are used in real life products.

Figure 2.17 - Some examples of applications of aramids in high quality products. (left to right) protective gloves (Safety Gloves.co.uk) and helmets (Security Pro) for hazardous work; Formula 1 fuel tank (Technical F1 – Dictionary); A cutway of Kevlar® reinforced tire (goodyear.com); Kevlar® cable (Applied fiber).

Despite the most diverse functions of these products, these share the same characteristics of these aramids that are their excellent mechanical resistance and low mass as well as a good resistance to high temperatures and durability.

2.4. Methods

The most used analysis models can be classified into two categories [Justo, 1996]:

1) Experimental methods or Empirical methods, which result from the correlation of a large number of experimental observations, and in general, addressing specific cases, not allowing extrapolations;

2) Theoretical methods that are subdivided into: (i) numerical methods that are essentially computational models applied through finite element or finite differences methods, which allow the solution of the equations of the balance of the continuum; (ii) analytically approximate models that seek to simplify reality through hypotheses that describe phenomena through differential, integral, or mixed equations, often based on energy and moment conditions. When delimited by simplified hypotheses, it can be of great use in obtaining phenomenological information about the mechanisms of penetration that other methods do not have [Mestre, 2015].

2.4.1. Armour Tests and Experimental Methods

Ballistics testing is a standards-based process in which products are tested to determine whether they meet the criteria for protection, safety, and performance. Most ballistics testing helps commercial research and development programs as well as law enforcement and military applications [Zukas, 1982].

It is important to note that there are norms and guidelines that regulate their levels of ballistic protection, defining the corresponding ballistic resistance capacity. A standard is a procedure whose follow-up is mandatory and its indications must be respected during the performance of tests on ballistic protection equipment so that such tests are considered valid and official in the eyes of the organization responsible for the standard [Master, 2015]. The guidelines are rules that are not bound by any legislation, consisting of test instructions that are established by public or private instructions. Although not mandatory, they should be taken into account when carrying out ballistic tests [Kneubuehl, 2003].

As already mentioned in other sections, calculating the ballistic behaviour of a shield involves evaluating the kinetic energy of the projectile during impact. The determining quantities for the

characterization of ballistic protection levels are kinetic energy (equation 2.6) and energy density (equation 2.7) of the projectiles, being determined as a function of their mass and velocity [Carlucci e Jacobson, 2010].

$$E_c = \frac{1}{2}mv^2 \tag{2.6}$$

Where m is the mass of the projectile and v his velocity.

$$Kinetic\ Energy\ Density = \frac{E_c}{A_p} \tag{2.7}$$

Where A_p is the projectile transversal area.

Since the velocity in the equation of kinetic energy is v^2, its component has much greater influence than the mass of the projectile, so small variations in velocity can lead to large variations in kinetic energy. Thus, many researchers consider this parameter to determine the analysis of the damage caused in the shield, adopting the previously mentioned definitions of V_0 and V_{50}.

Despite their definition, these two speeds are not evaluated in one way within the various standards existing between the various countries, as these are based on the caliber of the weapon, the distance to which it is fired, the number of shots tested, and the weight of the projectile and the area of the armor affected by the impact (V_{50} Ballistic Test For Armor, 1997). Through dimensional analysis, Cuniff defined a relationship between V_{50} and the parameters for bulletproof vests. This ratio, represented in (2.8), assumes that the impact energy is dissipated in the fracture of the vest fiber wires.

$$V_{50} = \sqrt[3]{\frac{\sigma\varepsilon}{2\rho}\sqrt{\frac{E}{\rho}}f\left(\frac{m_d}{m_p}\right)} \tag{2.8}$$

Where σ and ε are the stress and strain rupture, respectively, ρ the volumic mass of the fibers wire, E his Young modulus, m_d is the mass per unit of area of the vest and m_p mass per unit of area of the projectile [Cunniff, 1999].

There are several standards of vests depending on the countries, VPAM of Europe, GOST of Russia and NIJ (*National Institute of Justice*) of the United States of America. Since NIJ standards are the most used in the world, these standards are taken as a reference in this work.

Even outside the U.S., NIJ test standards are widely used by law enforcement and military forces to evaluate and acquire armor for public service officers. Some countries, such as the United Kingdom, have adopted similar parallel certification programs. The UK Home Office Scientific Development Branch (HOSDB) has a testing and certification program very similar to the NIJ program, but more focused on domestic threats to civil servants in the UK [Monteiro, 2007].

The tests in Portugal are carried out in accordance with NEB/T E-316, NIJ Std 0108.01, NIJ Std 0101.03 among others. The tests are performed by executing three shots in the shield, forming a triangle (norm NATO (*North Atlantic Treaty Organization*) Stanag 4190) [*Test Procedures for Measuring Behind–Armour Effects of Anti–Armour Ammunition*, 1999] as shown in figure 2.18.

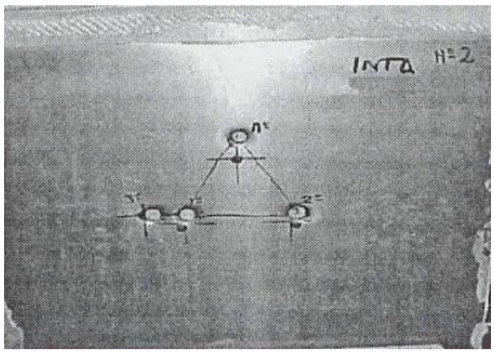

Figure 2.18 - Tests carried out on woven aramid (STANAG 4190, Test Procedures for Measuring Behind–Armour Effects of Anti–Armour Ammunition, 1999).

The rules aim to classify threat levels and their parameters in order to choose the right armor for this. Regarding ballistic resistance capability, the Standardization Agreement (STANAG) 4569 Protection Levels for Occupants of Logistic and Light Armoured Vehicles will follow. STANAG 4569 indicates the ballistic procedures and tests applied to various target systems and uses in its tests greater caliber threats, with the greatest threat corresponding to level VI. In section A.2, you can see the table with the different values of these standards for armored combat cars [Monteiro, 2007].

For bulletproof vests, NIJ0101.04 classifies ballistic vests by protection level based on the caliber of the weapon, the weight of the projectile and its speed. This classification can be best analyzed in the table in the attachments section A.3.

Despite the diversity of firearms and their ammunition, the threat potential is limited to the projectiles energy and therefore by its mass and speed. The characteristics of projectiles typically used in ballistic tests are summarized in section A.4.

Experimental tests initially require the manufacture of the specimens representing the shield to be tested, the structure where ballistic tests will be carried out must comply with a number of standards, as already mentioned, for example: NIJ Std 0101.06 and STANAG 2920, these standards define the procedures to be adopted for carrying out tests on ballistic panels. Despite the standards, there is not a single common physical procedure, i.e. the assembly of the tests can be quite diverse, and can use chronographs and high-speed cameras, for instance [Monteiro, 2007].

However, there are some aspects to highlight in these types of methods. The location of impact of the projectile appears as a point of high importance since the behaviour of the panel is directly dependent on where this impact occurs. An impact made at one end of a panel will result in different protection performance when compared to an impact made in the central area of the panel, as the surface conditions will be different. It is important to note that these tests represent as best as possible what happens in reality [Chu, 2016] [Nayak, 2016].

Figure 2.19 - Example of experimental test on a ballistic panel with 3 impact zones [Nayak, 2016].

In addition to the shots fired against the shields, one of the most common qualitative methods in ballistic research centers is the use of ballistic gelatin. This is a type of gelatinous solution that aims to simulate the density and viscosity of human muscle tissue to analyze the impact of the projectile on it. Once the shot is triggered, a visual inspection of the ballistic gelatin is performed to verify the possible damage caused by the impact. It thus mirrors the expansion results closer to reality, being only a visual inspection method used to quantify the power of impact.

In this technique, the shielding samples to be tested are placed immediately before the gelatin and in contact with it. The samples are conveniently constrained so that the damage to ballistic gelatin best simulates the effect of the impact on the human body. It is possible in this way not only to test armor, but also to improve the performance of projectiles (figure 2.20) [Pinto, 2009].

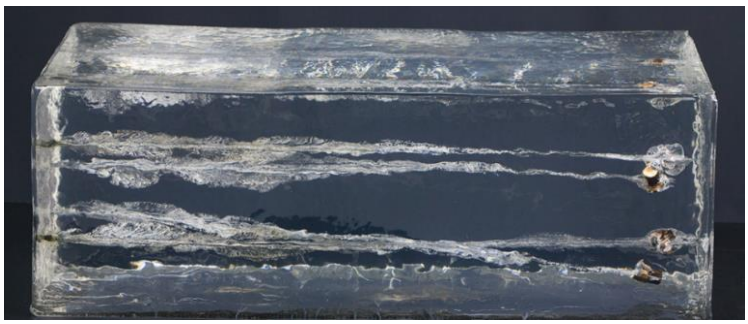

Figure 2.20 - Permanent cavity, resulting from the test carried out in ballistic gelatin (Handgun Self-Defense Ammunition Ballistics Test).

The Allied Engineering Publication (AEP) – 2920 describes the procedures for classifying light ballistic protections from threats such as ammunition and fragments. In this AEP are explained all procedures on ballistic tests and all procedures for assessing their evaluation, in order to evaluate the level of protection of ballistic protection elements. According to this standard, the arrangement of the most conventional test facility for ballistic protection elements should be similar to figure 2.21.

The set up must be constituted by the following components: (i) weapon (or ballistic cannon); (ii) projectile velocity detection and measurement system; (iii) fixing system for panels to be tested; (iv) witness plate; (v) projectile.

The control plate or the BACK FACE Signature (BFS) material must be placed in a way that the distance between the panel and the BFS material represents its actual use.

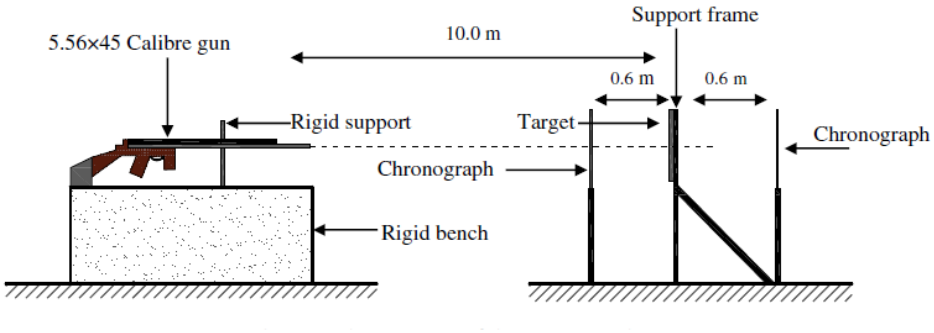

Figure 2.21 - Weapon experience scheme [Mohotti, 2015].

Prior to any ballistic testing, the entire test facility and all panels must be visually inspected for damage during transport. If a defect is observed, the test on that panel should not be carried out and shall be recorded as damaged.

All targets should provide the following information: (i) the serial number; (ii) the target category; (iii) type of ammunition to be used; (iv) identification of the target's inlet and outlet surface.

During ballistic tests, all impacts must be individually marked on each target [Mestre, 2015].

One of the solutions is used by the H.P. White Laboratory, a company dedicated to the evaluation of the armour of the U.S. Army and which is linked to the United States Department of Justice. Ballistic vests are tested qualitatively and quantitatively. To perform the evaluations, a sequential system is implemented, consisting of the firearm (responsible for propelling the projectile), two velocity sensors (allowing to know its value at a certain desired point) and finally the support with the shield to be analyzed (figure 2.22). Through the available sensors, it is possible to make an assessment of the energies involved in the process (*HPWhite – Resources*).

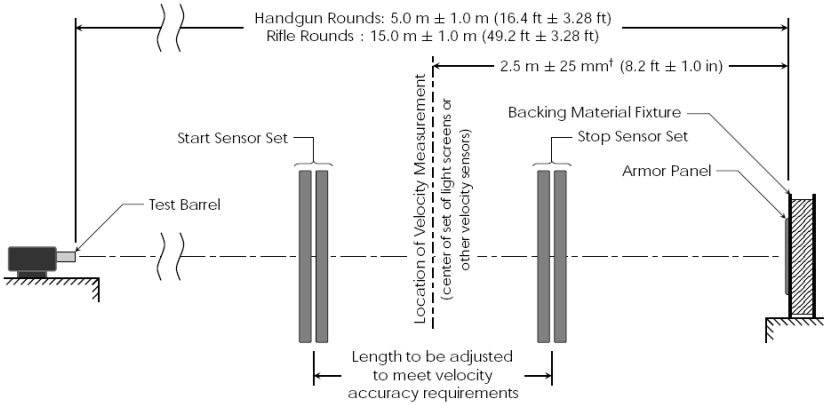

Figure 2.22 - Illustrative scheme of the sequential shielding evaluation system (HPWhite - Resources).

An interesting point in this process is the fact that the shield support is a box containing a homogeneous block of deformable material (modeled clay-based oil), which is placed in contact with the back of the shield (ballistic vest) during the tests. Thus, the "impact signature" is defined, which is reflected by the highest level of indentation suffered in the homogeneous block, which is measured by

the distance parallel to the upper and lower peaks perpendicular to the impact surface (BFS) (figure 2.23) [Pinto, 2009].

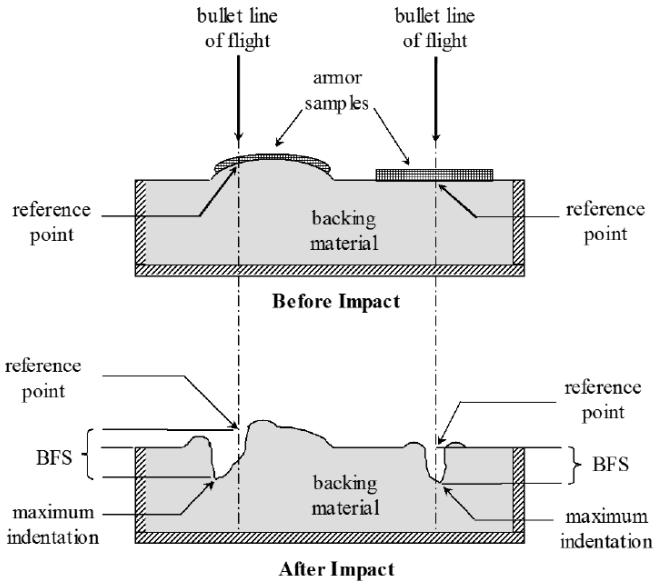

Figure 2.23 - Box armor support containing a homogeneous block of deformable material, before and after the impact of a projectile (HPWhite – Resources).

It should also be noted that in the armour support, the vests surface area is entirely covered by the support, which is as indicated in figure 2.24 (a). The tests are carried out according to NIJ standard–0101.04, already mentioned in previous sections, and six shots are performed (figure 2.24 (b)) [Pinto, 2009].

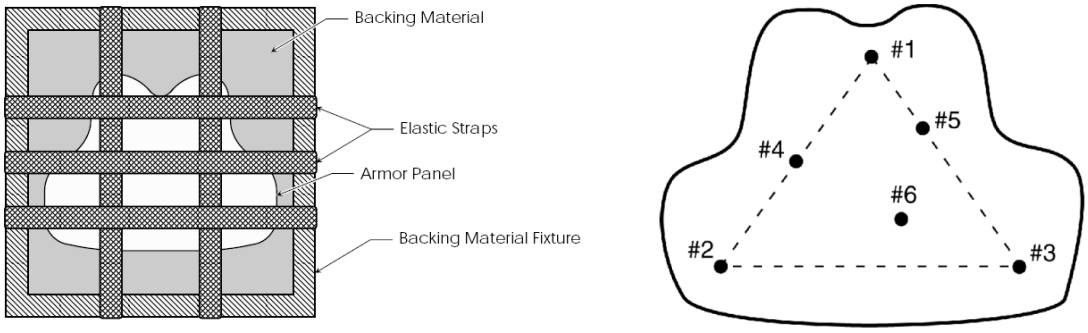

(a) (b)

Figure 2.24 – (a) Vest attachment system on the armor holder. (b) Tests according to NIJ Standard - 0101.04 (HPWhite - Resources).

In this study, it is only sought for an experimental method that allows evaluating the quality of ballistic vests. Analytical or numerical models are not used although it is important to refer briefly to cover the three types of ballistic protection analysis methods.

In IST, it was also studied and developed a method to test the aramid fabric. Flávio Duarte (2019) developed a model of a fixed weapon on a stand, with the use of two chronographs positioned before

and after the target that enable the measurement of the velocity of the impact and the output velocity, velocities that are necessary to calculate the kinetic energy of the projectile and the energy absorbed by the panel produced, following the sequence exposed in the figure 2.25.

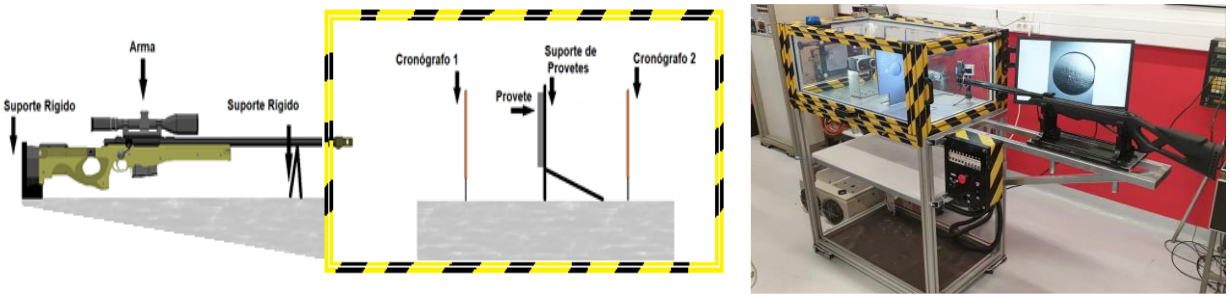

(a) (b)

Figure 2.25 - (a) Representative scheme of the experimental trial; (b) Ballistic testing machine [Duarte, 2019].

The weapon used was the Gammo Whisper Maxxiim 5.5mm caliber rifle, which presents variations in initial speed at the outlet of the barrel, according to the manufacturer's information, which can vary between 120 m/s and 275 m/s depending on the projectile used, these values vary widely due to the huge panoply of projectiles currently available on the market.

The tests were carried out in the laboratory making it imperative to obtain certain conditions that would ensure the safety of the operator as well as the persons present in the laboratory. The structure, in Bosch profile, allows a great capacity for transformation, adaptability and versatility allowing an isolated environment from the outside where the impact occurs. In this capsule were mounted the chronographs, the specimen holder, the camera to shoot in "slow motion". It is possible to find two holes one in each of the side profiles, which allow the passage of the projectile after impact to the projectile collection system, and another where the gun barrel is inserted, this allows any type of gas resulting from the shooting to be confined to the capsule. Access to the interior of the enclosed environment is carried out by raising the front and upper profile of the capsule with the aid of two pneumatic arms installed for this purpose and also to support the structure while data collection or specimen replacement is being carried out. The fixation of these specimens is achieved using two pieces designed and manufactured specifically for this purpose, ensuring the correct fixation of the specimen and allowing to test it in the four quadrants previously characterized, using a mechanical press the two pieces are compressed against each other, in this way we achieve the correct positioning and alignment of the target with the chronographs, with the system of collecting projectiles and with the weapon.

Duarte (2019) also developed a piece, where it was possible to install the support for the weapon ensuring a fixed, stable, horizontal and perfectly aligned shooting position with the entire structure. It was also necessary to design a system that would allow the collection of the projectile after shooting, ensuring that it would be confined to the test space and not put the safety of third parties at risk. This enables the dissipation of the kinetic energy that animates the projectile after impact, characterized by a steel alloy cone that corrects any oscillations of the final trajectory and by a storage compartment.

The chronographs performed the function of measuring and recording the initial velocity of the projectile next to the barrel of the weapon, and the final velocity after the impact on the target. With these

values it is possible to calculate the energy variation that occurs for the different targets tested and compare with the results obtained in the tests performed in the Hopkinson bar and three-point-bending. Two supports were also manufactured in order to attach the chronographs to the work table ensuring a perfect alignment, fundamental so that the projectile does not encounter any obstacles during the test and also to prevent it from hitting any of the chronographs. The alignment was tested using a laser, anticipating what would be the route of the projectile after shooting the gun.

After gathering the elements necessary for the assembly and performance of the tests, two pneumatic arms were coupled to the structure to ensure the support of the structure whenever access to the internal environment of the structure is necessary. A lighting system has been set up to ensure correct lighting of the work table, as it ensures an increase in the quality of the footage taken during the tests, as well as improves the quality of the environment where the test is carried out [Duarte, 2019].

2.4.2. Theorical Methods

As mentioned previously, these models are based on some simplifications whose purpose is to consider only the predominant damage mechanisms, thus simplifying the analytical model without it being no longer valid. Also the characterization of the material is made on the basis of a small number of parameters, and the projectile itself can be considered rigid which implies not considering the energy dissipated by its deformation [Pasquali, 2015].

Many of the existing analytical models are based on energy components. One of them created from a composite material composed of thin glass fibers and laminated carbon fibers, by M.Pasquali (2015), shown in figure 2.1, where the impact energies are divided as follows:

$$E_0^{KP} = E_i^{KP} + E_i^{KC} + E_{i-1}^{PY} + E_{i-1}^{SY} + E_{i-1}^{SP} + E_{i-1}^{DL} + E_{i-1}^{MC} \tag{2.5}$$

Where $i = 1, \dots, l$, E_0^{KP} is the kinetic energy of the projectile before hitting the target, E_i^{KP} and E_i^{KC} are the kinetic energy of the projectile and the conical region of the target displaced by the transverse waves in the interval i, respectively, E_{i-1}^{PY} represents the energy dissipated by the fracture of the primary fibers, E_{i-1}^{SY} represents the impact energy of the secondary fibers until the instant $(i-1)$, E_{i-1}^{SP} is the energy dissipated via shear stress applied by penetration into the perimeter of the projectile, E_{i-1}^{DL} and E_{i-1}^{MC} are contributions of energy absorption due to delamination and fracture of the matrix, respectively up to the instant, $(i-1)$. Finally, l is the last moment of the impact.

There are models with greater simplicity than this being easier to determine, however, this model has the advantage of being more complete with regard to the surrounding energies on impact considering a large evaluation time interval [Pasquali, 2015].

As far as experimental methods are concerned, there are some disadvantages, such as the fact that they are generally destructive, with high duration tests and associated costs. Analytical methods, on the other hand, fail to include all variables of ballistic impact [Duarte, 2019].

Numerical models, on the other hand, have some advantages that other methods exclude. Although they are also based on some simplifications in order to make the treatment of the problem simpler, always trying not to compromise the results obtained, the methods of this model are more practical and seek to represent reality as much as possible [Silva, 2004].

The use of numerical simulation tools allows the acquisition of certain data, including the residual velocity of the projectile, the limit velocity of penetration, the damage patterns of the laminated compound, characterize the intralaminar behaviour (rupture of the fibers or matrix), characterize the interlaminar behaviour (delamination), the crushing of the fibers, the shear connection (shear stress originated by the projectile during drilling), the energy absorbed by each damage mechanism and the material displacement profile (figure 2.26) [Bodepati, 2016].

However, it is important to take into account that the virtual model describing the physical phenomenon may be associated with modeling simplifications, which will necessarily lead to incorrect numerical results, even though the data provided by the user being the most indicated [Mestre, 2015].

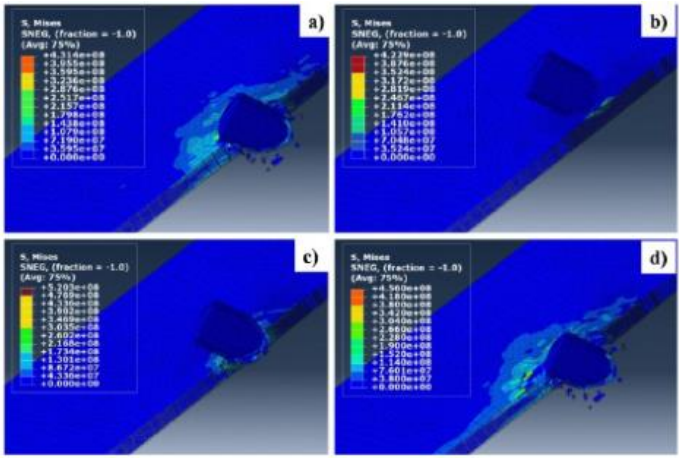

Figure 2.26 - Example of numerical simulation of projectile interaction with target a) 6μs; b) 10μs; c) 16μs; d) 36μs [Bodepati, 2016].

2.5. Split-Hopkinson Pressure Bar

The construction of a structure requires a perfect knowledge of the elastic and plastic properties and behaviour of the materials that compose it, and it should always be borne in mind that these behaviours might vary over time, depending on the various environmental factors in which it is located.

One of the most important properties for the choice of materials is the way they behave when they are subjected to loads. This type of information is collected through destructive tests, in which the most common are those involving reduced strain rates, considered classic tests, where the specimen is slowly deformed. In these tests, the necessary information on the behaviour of materials is not obtained when they are subjected to high strain rates, and for this it is necessary to resort to tests that create these types of conditions, and it is in these situations that the split-Hopkinson pressure bar (SHPB) is used. [Pires, 2016].

2.5.1. Fundaments

SHPB is a device that performs tests of compression, traction, torsion, and is generally used to study the behaviour of materials when subjected to high strain rates [Pires, 2016]. This testing machine is traditionally made by of the following main components: (i) actuator/projectile bar; (ii) incident bar; (iii) transmitting bar; (iv) support structure of the bars (beam); (v) propulsion system; (vi) shock absorber; (vii) measuring system (e.g. strain gauges). Figure 2.27 represents a scheme of a conventional SHPB.

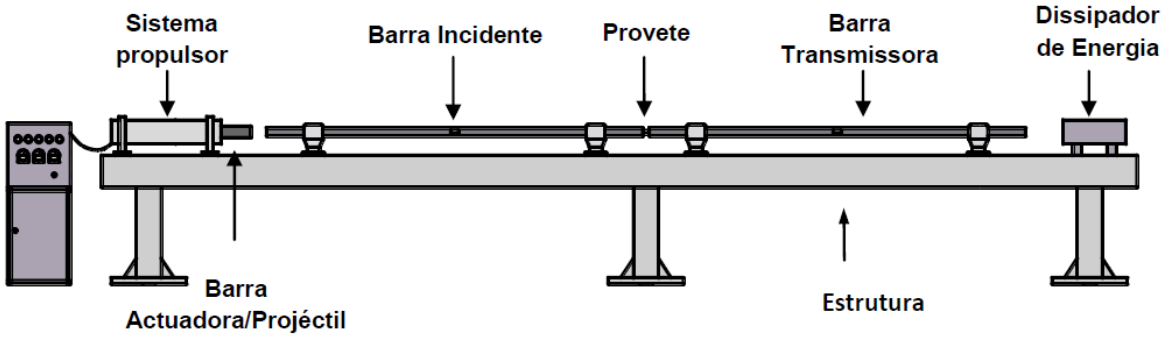

Figure 2.27 - Scheme of a split-Hopkinson pressure bar [Pinto, 2009].

The three bars mentioned must be sized with the same diameter and placed coaxially on the support structure (beam) fixed on guides, taking into account the position of the propulsion system ensuring that such configuration happens. The shock absorber assembled adjacent to the transmitting bar so that it can absorb and dissipate energy as well as shock waves as far as possible from the impact.

For test preparation, the specimen must be placed between the incident bar and the transmitting bar, the measuring systems activated and placed in their proper places, as well as the propellant system used (pneumatic, hydraulic or electromagnetic), must be ready for shooting.

As for its mechanism, a test on the SHPB begins by activating the propellant system used that generates a certain amount of energy that will animate the actuator/projectile bar by initiating its movement in the direction of the incident bar, with an energy transmission at the time of the impact of the two bars. In chain shock effect, the incident bar will pass its energy to the specimen, which in turn passes to the transmitting bar, after suffering the deformation due to impact, concluding with the impact of the transmitting bar on the shock absorber. Assuming, during the various collisions between bars, with regard to the calculation of energy, an energy dissipation between each impact.

For the measurement system, in SHPB, the strain gauges should generally be placed on the incident and transmitting bars (figure 2.28) in order to measure the incident, reflected and transmitted wave pulses, with which, through mathematical expressions that relate with each other, a stress-deformation diagram is obtained for each deformation rate under analysis [Kist, 2014].

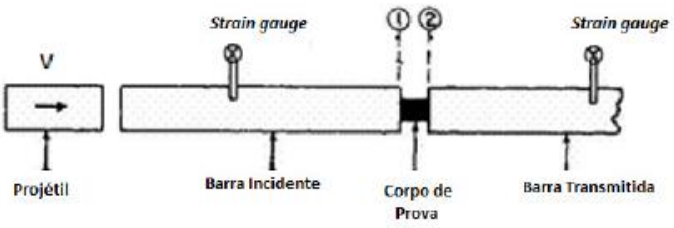

Figure 2.28 - Localised diagram of the specimen area with the fixing of strain gauge [Kist, 2014].

However, due to complex phenomena, the traditionally used reflected pulse technique may be unreliable when determining the specimens' strain [Bazle, 2004]. Non-contact measuring methods, such as high-speed imaging techniques, are often an alternative to the reflected pulse technique. Although, for thin specimens such as fabrics, with undefined shape and ragged loose fibers, the visual data becomes low-quality definition with an unclear-cut "specimen-tool" contour. A novel measuring technique called inductive coil extensometer is then used in this study for measuring the distance between the incident and transmission bar ends, thus improving the accuracy of strain determination. This measuring system will be explained in detail in further sections.

There are several types of destructive tests, which differ from each other by the values of the deformation rates applied in the specimens, and are divided by the following intervals [Ferreira, 2003]: (i) classical, or quad-static, essays – [$\mathbf{0}$, $\mathbf{001}$; $\mathbf{0}$, $\mathbf{01}$]$\boldsymbol{s}\mathbf{-1}$; (ii) tests at medium deformation rates - [$\mathbf{0}$, $\mathbf{1}$; $\mathbf{100}$]$\boldsymbol{s}\mathbf{-1}$; (iii) tests at high deformation rates – superiors to $\mathbf{1000}\boldsymbol{s}\mathbf{-1}$.

However, there is no clear definition of these intervals, as they often depend on the material being studied [Ferreira, 2003].

The most current and used SHPB was developed in 1962 by U.S. Lindholm which aimed to achieve strain rates between 100 s−1 and 5000 s−1, where the duration of the test was equivalent to most explosions, ballistic impacts, among other scenarios, which had applications in many areas of interest both at the military level, as at the civil level [Split Hopkinson Pressure Bar Apparatus - An Historic Mechanical Engineering Landmark, 2006].

2.5.2. Evolution of the SHPB in IST

At Instituto Superior Técnico, several experimental studies were developed over the years aimed at the study of mechanical behaviour of various materials, especially ballistic components, through tests at the split-Hopkinson pressure bar.

In 2007, Pedro Monteiro used a Hopkinson Pressure Bar (figure 2.29) as a laboratory methodology to quantify, in addition to traditional indicators, the remaining energy transmitted through ballistic vests.

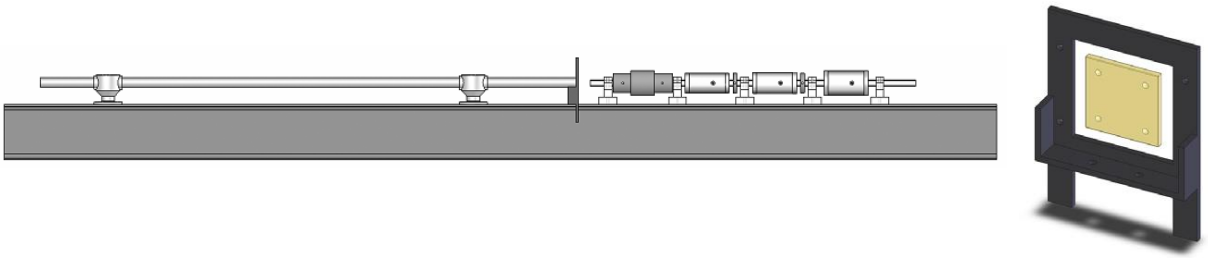

Figure 2.29 - Split-Hopkinson pressure bar model (left) and 3D model of armor sample support (right) used in the study by Pedro Monteiro, 2007 [Monteiro, 2007].

The structure is composed of a rigid beam where two supports are installed for the high-strength steel transmitting bar with 1500 mm in length by 25 mm in diameter, so that it moves only along the impact axis. For the adaptation to the shielding tests, a support for shielding samples was fitted, designed with the aim of ensuring a good alignment of the shielding tests with the impact axis. The large quadrangular space thus created allows a great flexibility in the level of sampling, being possible to test samples with various dimensions.

For the propellant system in this study, an electromagnetic trigger was used composed of three independent coils, each connected to the respective condenser bank that allows a systematic acceleration of the projectile [Monteiro, 2007].

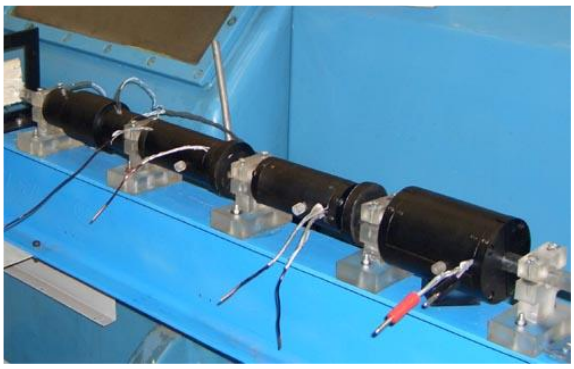

Figure 2.30 - Electromagnetic trigger [Monteiro, 2007].

The model used turns out to be a simplification of a SHPB in order to make its use practical. The transmitting bar is held only by two supports and the projectile directly reaches the ballistic sample by the electromagnetic trigger, i.e., there is no usual incident bar as intermediate.

In 2009, another study was carried out by José Pinto, an incident aimed at studying the remaining energy transmitted to ballistic vests, similar to the study by Pedro Monteiro, but with a different methodology.

This structure of SHPB presents a greater complexity relative to that of the previous study. In this assembly, the first part consists of: main structure of the trigger (serves as support and fixation to the trigger); secondary trigger structure (gives greater stability, rigidity and height to the trigger, still functioning as power bank warehouse).

The second part is where the Hopkinson bars are installed and is where the ballistics tests themselves are carried out, being designated as the main structure of the apparatus. In this structure

are mounted the following systems: incident bar (which have coupled the projectile of caliber 9 mm or 5.56 mm), bearings of the bars and their clamps, the transmitting bar (with extensions for reading the deformations), the support for the shielding samples, the respective fixation device and the support, the target and the displacement sensor [Pinto, 2009].

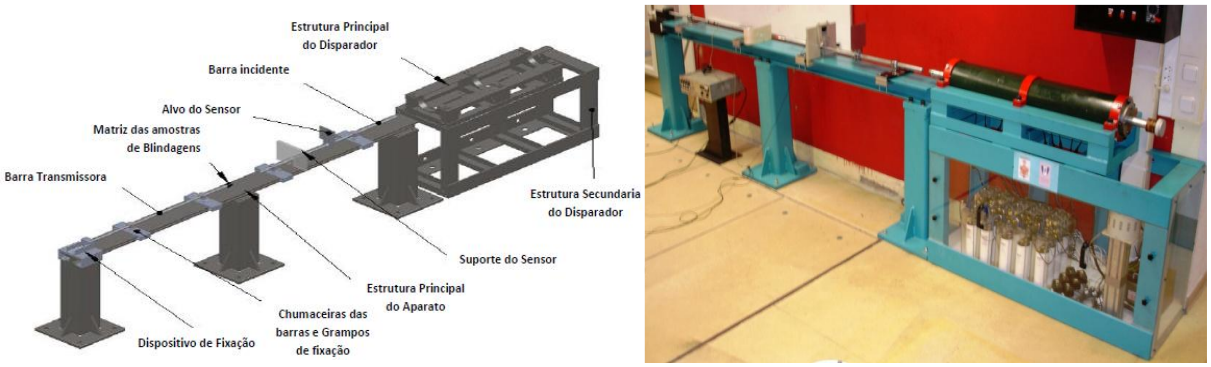

Figure 2.31 - (left) 3D model of the ballistic test bench; (right) Real split-Hopkinson pressure bar of the study by José Pinto, 2009 [Pinto, 2009].

The basic concept of the operation of the electromagnetic trigger consists in the incorporation of several ferromagnetic cores in the impact bar, corresponding to one coil each, thus allowing a sum of forces originating from each of the coil/core assemblies, and the shooting is carried out simultaneously. The operation is characterized by the simultaneous and rapid passage of an electric current through each of the coils, using the high voltage power bank. The passage of the current through the coils leads to the creation of a magnetic field, which causes the ferromagnetic nuclei to move to the center of the respective coil. This is because the coil, acquiring a magnetization inverse to that of the coil field (figure 2.32), magnetizes when a nucleus approaches the field created by the coil [Pinto, 2009].

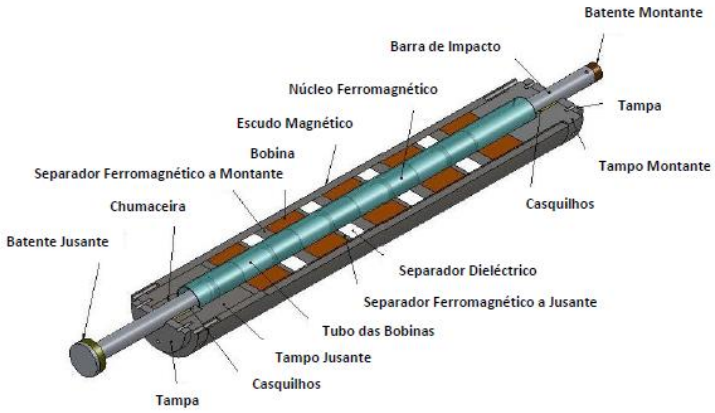

Figure 2.32 - Representation in detail of the electromagnetic trigger - cut view [Pinto, 2009].

This system carries greater complexity than the previous one, including, for example, an incident bar. However, there is a lack of some components that prevent higher impact speeds without damaging the machine. This could be countered with an energy dissipating mass, staples, among other components that contribute to increased rigidity of the structure.

Still within the dynamic tests, Afonso Gregório (2017) developed in LabM3 a drop hammer for medium speeds. This test machine consists of three quadrangular tubes in welded construction with 200, 100 and 50mm of section, in order to allow the use of different masses for the same height. These tubes allow the controlled/guided fall of the masses at a useful height of 2.5m and, from the ground, about 0.5m to allow the assembly of the compression tool. The masses are lifted by means of an electric winch with magnetic hook that, when actuated, releases the mass. This test machine allows a speed range between 1 and 8m/s and a mass range between 1 and 100Kg, allowing you to configure different speed-to-energy ratios. It is important to remember the importance of impact energy control, because the remaining energy of compression will be dissipated in the tool [Gregório, 2017]. Figure 2.33 (a) represents a scheme of this fall hammer.

For high-speed tests, still in the same study, Afonso Gregório (2017) used a pneumatic cannon, essentially composed of a pressure tank and a tube that allows the guidance and acceleration of a projectile, identical to that used in this thesis (explained in the section "Experimental Development"). The drive of a valve allows the pressurized air in the tank to flow into the barrel, propelling the projectile.

The pneumatic gun was installed on a beam to allow the shooting horizontally. The intermediate bar was aligned with the gun barrel and then integrated into the system using a bearing. This bearing was austenitic stainless steel AISI304L and had a central hole, where an acrylic bearing was placed, with the proper clearance to allow the longitudinal movement of the smooth bar, without compromising its guiding.

Afonso Gregório's experimental apparatus (2017), for high speeds, already has an appearance closer to a part of the apparatus of this thesis.

In the next sections, the SHPB developed is explained by highlighting the improvements, differences and adaptations made in order to correct defects and other possibilities that the Hopkinson trials presented in previous studies lack.

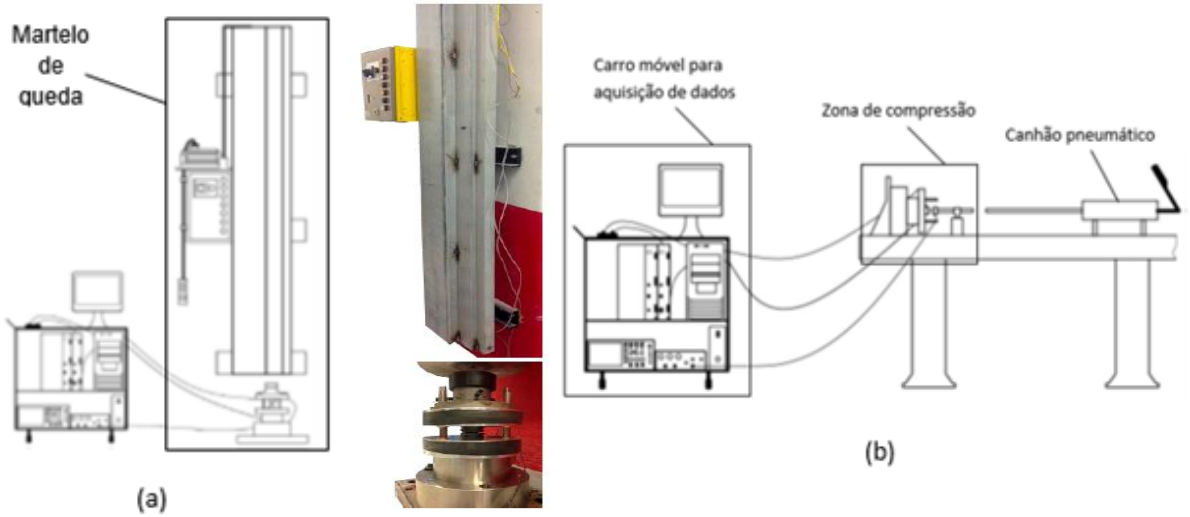

Figure 2.33 - (a) The assembly diagram of the drop hammer used for medium-speed tests and his real representation in the laboratory; (b) Mounting scheme for the pneumatic gun used for high-speed testing [Gregory, 2017].

3. Experimental Development

This chapter describes the materials used during the tests and the entire experimental machine design process adapted to the type of planned tests and all the instrumentation needed to monitor these experimental trials.

3.1. Materials

The tests made on the SHPB resemble the impact of a bullet in terms of energy and velocity, with the tests characterized as uniaxial compressive tests, performed on plain-woven aramid samples. These woven aramids have a weight of 300g/m^2 and a geometry of 100x100mm.

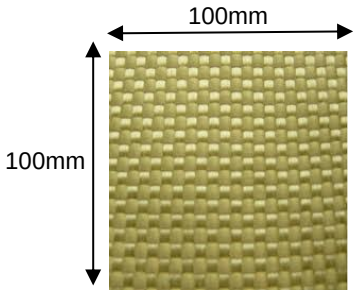

Figure 3.1 - Woven aramid sample with dimensions 100x100mm.

Since the electromagnetic field originated by the two coils is not influenced by non-conducting materials, the plain-woven aramid samples proves to be ideal for this kind of sensor, particularly during the impact tests where visible particles are usually released into the surrounding environment (fibres, binding agents, performance additives, lacquer and various emollients etc.). This fact tends to be extremely useful on impact tests on thin textile fabrics where specimen thickness depends mainly on the number of overlying layers, relative orientation between layers and applied preload before compression testing. In fact, initial specimen thickness can be as low as 100µ and significantly affect by a few grams during the clamping procedure.

3.2. Experimental Machine

As mentioned in previous sections, the machine designed for the tests of this study is based on the split-Hopkinson pressure bar. Figure 3.2 shows the Computer Aided Design (CAD) model and the actual representation of the set. The choice of this machine for this type of test is justified by the kinematic signature of this equipment that allows an impact speed similar to that of an ammunitions projectile, not including its penetrating effect.

One of its components is the propulsion system, which in this case will be a compressed air tank that functions as pneumatic gun. The actuator/projectile bar is a mass that can be exchanged for other

masses with different weights and different materials that, through the pneumatic gun, is shot at a certain speed, regulated by the relative pressure of the air tank, colliding with the incident bar transferring kinetic energy through the impact. The specimen must be between the incident bar and the transmitting bar that is then subjected to a compression force applied by the incident bar animated with the kinetic energy of the projectile. Finally, this energy, after compression of the specimen, is transferred to the transmitting bar that dissipates it into a shock absorber.

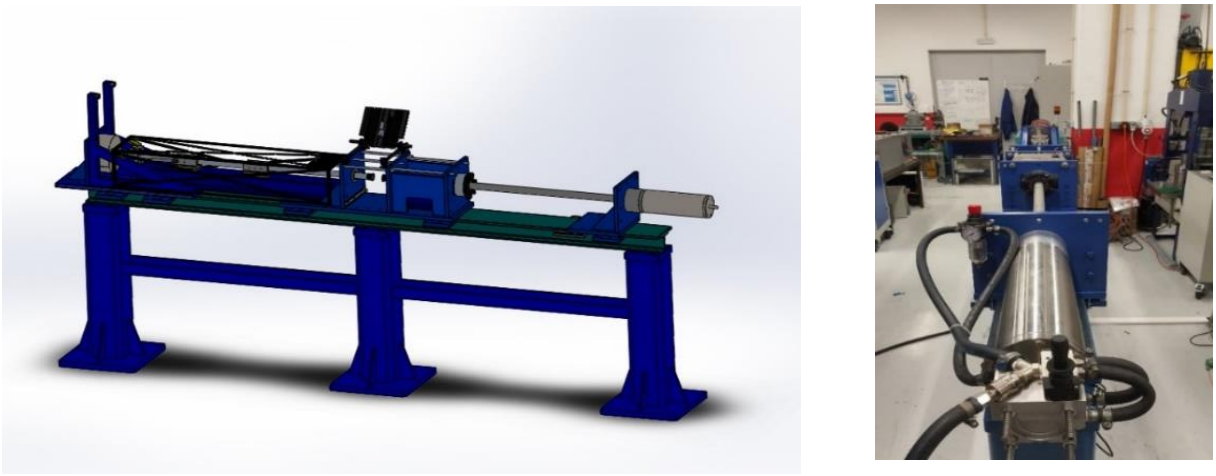

Figure 3.2 - (right) CAD model of SHPB and other equipment involved; (left) Photo of the actual SHPB.

3.2.1. Transmission and Incident Bars

For the vast majority of SHPB, the material used in the pressure bars are steel alloys due to their high mechanical strength and their rigidity [Ramesh, 2008]. However, in order to improve the characteristics of these bars, it was decided to use titanium alloys, since it is essential that the bars have high mechanical strength with the addition of low weight in order to reduce any type of resistance to their movement such as friction.

The transmitting bar has the function of transmitting the residual energy, which was not absorbed by the aramid fabric, to the energy dissipating mass. While the incident bar has the function of receiving the impact of the projectile and, with the kinetic energy provided to the bar in this impact, transmit it to the specimen.

The bars in question must be made of the same material, same diameter, must remain in elastic regime throughout the duration of the test, must be aligned concentrically and friction should be minimized as much as possible, allowing the bars to move freely horizontally.

3.2.2. Shock Absorber

One of the first precautions to take in the construction of this equipment was the design of the energy dissipating mass. The function of this component is to be able to withstand the high energy values transferred to it by the transmission bar, being able to dissipate this energy safely preventing any damage to the machine or present any kind of danger to people near the machine.

Figure 3.3 (a) represents the CAD model of the shock absorber to be installed at the end of the apparatus contrary to the propellant system. Initially, four frontal triangles were used, however, when testing the machine in quasi-static tests it was noted that the shock absorber yielded when reaching a certain pressure value, thus it is necessary to reinforce it with two larger triangles on the face contrary to the smaller triangles.

The central hole of the vertical plate has the dual objective of allowing the assembly of an electromagnetic gun (not included in this study) on the side of the smaller triangles or an energy dissipating mass on the opposite side, as illustrated in figure 3.3 (b).

As mentioned above, this mass will have the functionality of dissipating as much energy as possible from the impact of the transmitting bar.

The material of the boards, triangles and staples used was CK45 commercial steel. It only makes sense to use this steel (the most common commercial steel), due to its good mechanical strength and low price/weight ratio, since these parts constitute the highest percentage of machine weight.

The holes in the horizontal and vertical plates were made in CNC (*Computer Numerical Command*) in the Núcleo de Oficinas (NOF) at the Instituto Superior Técnico, later polished. Once prepared, they were cleaned with acetone to remove the oil on its surface and then painted blue. The technical drawings of the plates, both shock absorber and the sides of the incident bar (explained later) can be found at the end of the attachment section.

The main function of the components in this section is to ensure that the energy present in the impact of the tests is dissipated without damaging any of the machine parts. Figure 3.3 (c) shows all of these components. It is notable that the triangles, both larger and the two smaller (not visible in the figure), are fixed to both the vertical and horizontal plate. The clamps with shims, two on each side, and the beam supporting the transmitting bar are fixed to the horizontal plate and, finally, it is fixed to the base beam.

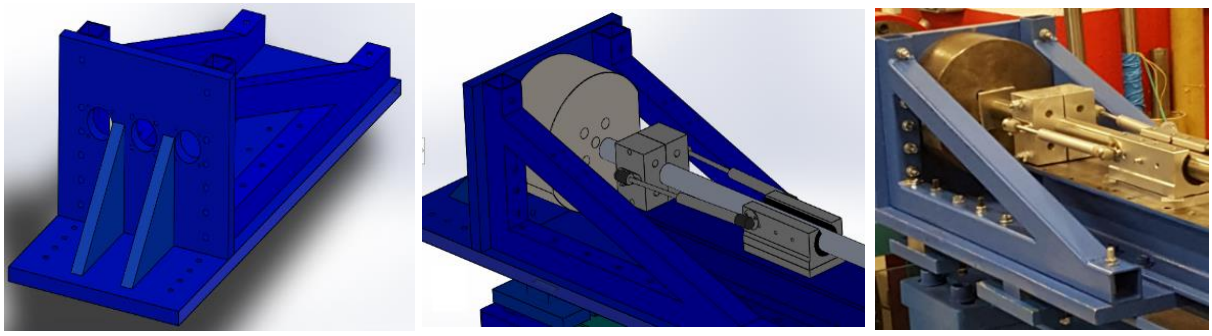

(a) (b) (c)

Figure 3.3 - (a) shock absorber CAD model; (b) CAD model of the shock absorber, its mass, the transmitting bar and additional componentes; (c) Transmitting bar, shock absorber and surrounding components.

In order to plan exactly where each of the pieces should be placed and help understand what parts are, they were drawn in CAD (figure 3.4). In addition to the larger (3) and small (4) triangles, shim clamps (11), energy dissipating mass (2) and vertical plate (1), which give greater structural rigidity to the machine, the transmitting bar (9) is constrained by two bearings (7), which allow it to move horizontally

only, keeping it parallel to the ground and perpendicular to (2), fixed to the beam of the transmitting bar (blue) (8) where it is on a horizontal board (12) that serves as the basis for this entire section , and is finally supported on another base beam (green) (13) covering virtually the entire machine, supported by three pillars (10) fixed to the ground.

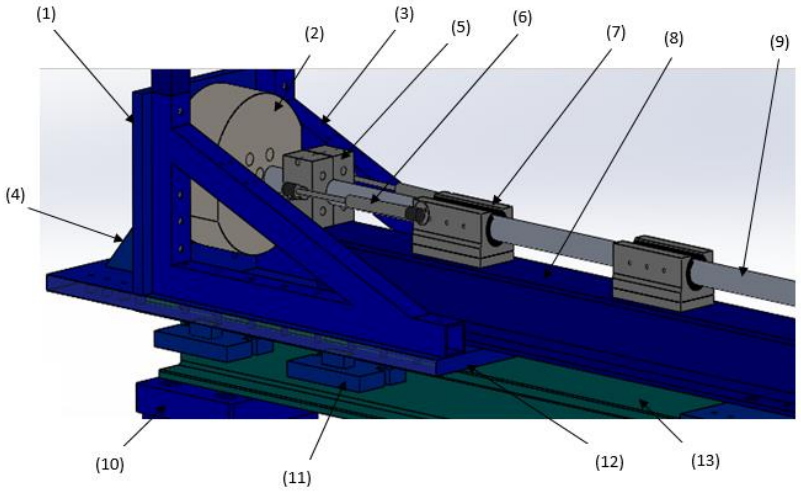

Figure 3.4 - CAD model of the shock absorber section, transmitting bar and surrounding components: (1) Vertical plate; (2) Energy dissipating mass; (3) Large triangles; (4) Small triangles; (5) retaining block; (6) Dampers; (7) Guides; (8) Beam of the transmitting bar (blue); (9) Transmittingr bar; (10) Support pillars; (11) Shim and clamps; (12) Horizontal board; (13) Base beam (green).

After testing the machine, it was verified that the impact of the transmitting bar with the energy dissipating mass led to a rebounce of the bar, i.e., it was verified that part of the energy was reverted back to the bar leading to it moving backwards interfering with the measurements of the extensometer.

To solve the problem, were fixed to the bar two steel parts (5) functioning as retaining ring, connected to two dampers (6), one on each side, with a load of 80N, drastically decreasing the effect of rebounce.

Finally, to ensure the safety of people near the shock absorber, a removable safety net has been installed, with the appropriate indications (keep the safe distance, wear goggles and headphones when subjected to very high pressures), along the entire transmitting bar, preventing any damage due to the loud noise of the impact or the possible hazard of particles from the impregnate or other substances resulted from the bar collision with the aramid fabric.

3.2.3. Zone of Experiments

Both bars have fixed at their end a Fast Steel or HSS (High Speed Steel) each. This steel alloy is widely used in cutting tool coating due to heat treatments that allow the withstanding of high temperatures without losing its hardness properties. This characteristic is essential in SHPB tests, as the impacts applied on this machine generate extremely high temperatures that could lead to the loss of hardness of the material reflecting in a greater wear of the tip of the bars making the results unfeasible.

The assembly process of the HSS to the bars is made by thermal interference, in other words, through the union by interference of two parts to form an integral assembly, in this case, hot process (thermal assembly). This type of interference assembly uses the phenomenon of thermal expansion

during the heating of materials, and contraction during cooling of the same. This eliminates mechanical interference with little to no pressure required for assembly, implying reduction of residual stresses and deformations and ability to control the quality of the union. Some of the other advantages of this process are: (i) the easy reversibility of the process, (ii) controlled and localized heating, (iii) reduction of total processing time and (iv) energy savings.

With a central hole in order to allow the passage of the carbides, two polymeric plates are screwed to both bars in order to serve as the basis for the two coils that act as motion sensors between the bars. The two bars pass through two vertical boards centered by one guide each in order to ensure movement only horizontally, concentric to each other, as shown in figure 3.5.

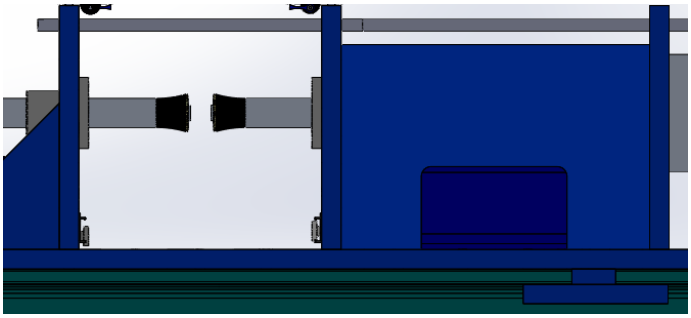

Figure 3.5 - CAD model of the zone of experiments.

When the specimen is in position and proper protective measures are satisfied, the test may be carried out. When activating the propulsion system, the projectile is animated with a V_0 speed, proportional to the pressure generated, which will reach the incident bar, as respresented in the scheme of the figure 3.6. This displacement sensor will be explained in detail in the further section.

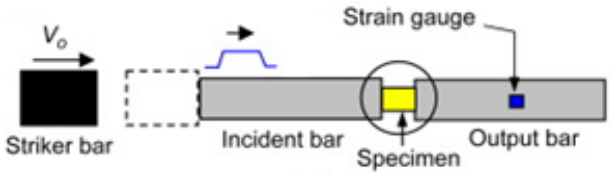

Figure 3.6 - Impact between the bars with spcimen and strain gauge represented scheme.

3.2.4. Sensors

Measurements of the strain and force applied to the specimen are made through the following instrumentation: (i) load cell; (ii) displacement sensor; (iii) data acquisition system.

3.2.4.1. Load Cell

The load cell is used to monitor compression forces and consists of four extensometers. The extensometer is a transducer capable of measuring the mechanical deformations of the specimen through the deformations felt in the transmission bar, where it is installed (Figure 3.7 (a)). When a deformation occurs, the resistance of the strain is changed. It consists of only one wire that zigzags the path between the terminals in order to maximize the length of the wire, and with a minimum cross-sectional area so that transverse deformations do not cause an unwanted variation in resistance, leading to measurement error. In this way, it seeks to reduce the Poisson coefficient as much as possible. The coupling of the strain gauge is made in such a way that the wires are parallel to the direction of deformation of the bar and by drawing a line between the terminals, this must be perpendicular to the tension of interest so that the strain, when deforming, presents wire compression.

However, it is not easy to measure the resistance variations in the load cell because they are very small values, because the magnitude of the ε deformation is small. For this purpose, the configuration of an electrical circuit called Wheatstone bridge is used, which allows the measurement of the value of an unknown electrical resistance by measuring the output voltage of this circuit. This configuration is adopted for the load cell, with the four blade strain gauges in place of the resistances (figure 3.7 (b)).

(a) (b)

Figure 3.7 - (a) blade strain gauge and its components; (b) Configuration of load cell strain gauges in Weathstone Bridge.

The Wheatstone bridge is connected to an amplifier from the manufacturer VISHAY, model 2310B, for load cell conditioning. The amplifier was configured with a gain of 500. It should also be noted that it is necessary to periodically confirm the excitation value of the amplifier and to inform that high gain values make the data acquisition system very sensitive to external disturbances.

For the experiments, it is necessary to do a calibration of the load cell in order to obtain accurate results. It was applied, through a hydraulic propulsion system, a load, in *quasi-static* conditions, on a commercial load cell, with known values. This test establishes a relation between the load applied and voltage generated on the strain gauges.

3.2.4.2. Displacement Sensor

The distance between the compression plates is monitored by two coils (figure 3.8 (a)) that function as two displacement sensors that are based on the principle of electromagnetic induction between coils, i.e., the current imposed on a spiral generates an electromagnetic field that, in turn, will induce an electric current in the opposite coil. Therefore, an increase of measurement accuracy is observed for displacement monitoring of small distances between the compression plates. This current varies with the distance the two coils have between each other, The closer the coils are, the more flux reaches the receiver and the better the coils are electromagnetically coupled. The coil emitting the electromagnetic field was mounted on the movable plate and the induced signal-receiving coil on the fixed plate next to the load cell. This mounting option simultaneously minimizes the electromagnetic coupling between the coil signals and the load cell signals and, increase the accuracy of the measurement by avoiding unwanted contributions from elastic deformations of the tool, the test machine of the reduction of clearances between components during loading during loading.

The coil turns were made of CNC through a printed circuit board (PCB), which contains a copper layer of 40µm. Its surroundings consist of a ring shape with interior diameter 17mm and outer diameter 39mm for compatibility with compression plates.

A study by Pedro Santos (2019) sought to analyze the influence of the number of turns on the emission and reception of the electrical signal, in order to understand what would be the best configuration of the number of turns for this type of tests. According to this study, the parameters that remained constant were the geometry of the outer (50 mm) and interior (18 mm) circumferences. The value chosen for the inner circumference was the same as the diameter of tungsten carbide so that, when the coil was assembled, it entered the compressor plates to avoid dislocations throughout the test. In figure 3.8 (b) it is possible to visualize the configuration of the coil chosen by the author according to his study. This sensor chosen for the compression tests has 11 turns, since it showed a signal 300% higher than the other coils.

After the coils were manufactured, a 1mm dimension hole was drilled in each coil terminal in a drilling machine so that the electrical wires could be welded, which would connect to the data acquisition system. Then, before connecting to the system, the coils were subjected to a layer of polyepoxy resin (better known as epoxy), in order to increase the stiffness of the coil surface in order to protect its integrity from the violent impacts of the tests.

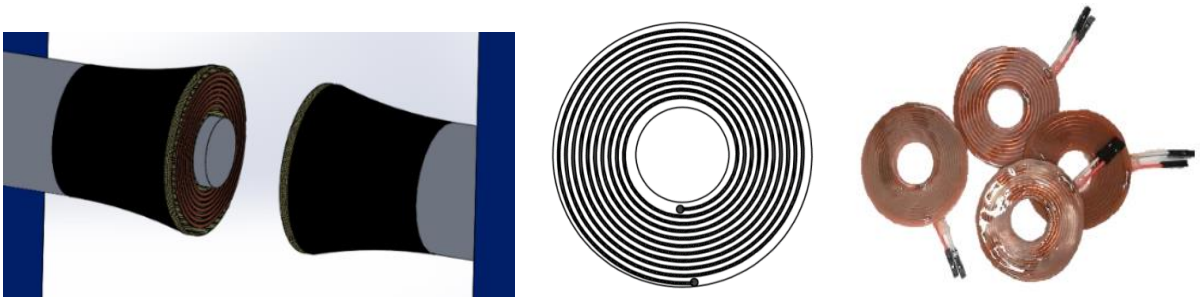

(a) (b) (c)

Figure 3.8 - (a) CAD model of the two coils glued to the compression plates; (b) CAD design of the sensor developed with 11 turns; (c) Coils used in the trials [Santos, 2019].

According to Pedro Santos (2019), the electric current signal that passes through the coils of the distance sensors has to be a high frequency sinusoidal signal with peak-to-peak voltages greater than 10 V, so it was necessary to resort to a function generator. Once the sensors were ready, the emitting coil was connected to a function generator of the manufacturer AIM&TTi, model TG315, while the receiver coil was connected to an oscilloscope of the manufacturer Tektronix, and model TDS220, to observe the AC signal necessary for the establishment of the electromagnetic coupling. Since the signal sent by the function generator is an AC signal and the data acquisition card only receives DC signals, this signal needed to be rectified to a DC signal, so from the signal obtained in the oscilloscope a full wave rectifier was sized to make this conversion. The rectifier consists of a rectifier bridge of four semiconductor diodes in silicon (figure 3.9).

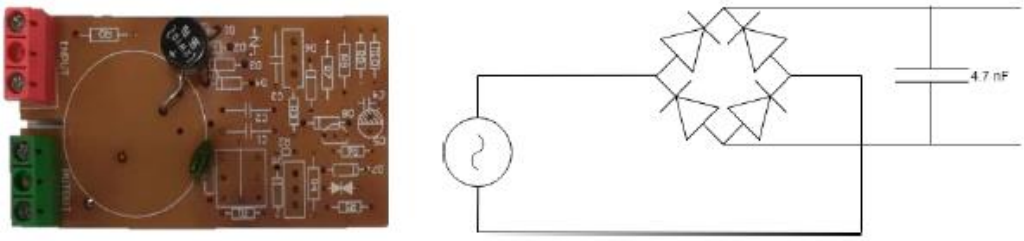

Figure 3.9 - Rectifier [Santos, 2019].

The sinusoidal wave has an alternating current, AC, so the rectification process itself produces a DC current that, although unidirectional, contains current pulses. As such, in order to soften the value of the obtained current, a condenser was placed at the exit of the diode bridge.

It should be kept in mind that, although high capacitance values soften the output signal, they slow down the system response. It is necessary to find a compromise between smoothing the output signal and getting a response in a short time interval, using a condenser with 4.7nF capacitance [Santos, 2019].

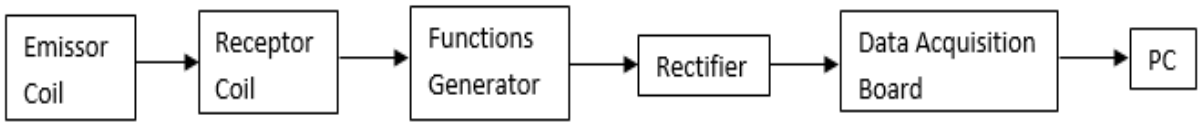

Figure 3.10 - Displacement sensor mounting scheme.

This rectifier plate was subsequently connected to a data acquisition plate in order to record the DC signal measured by the sensors.

Just like the load cell needed a calibration, so does the displacement sensor. In this case, it was used a potentiometer above the incident bar, in such a way that when the bar moved from the impact of the projectile, it would change its voltage. Knowing the distance travelled by the bar upon impact, it is, once again, possible to establish a relationship between voltage and distance travelled between compression plates.

3.2.4.3. Data Acquisition

A data acquisition system consists of a converter (ADC) that converts signals of physical quantities into electrical signals (voltages or currents). A data acquisition card (Data Acquisition - DAQ) of Ni manufacturer, model PCI 6115, was used, which allows the simultaneous acquisition of 4 channels up to 10MHz, 16MS, 12bits up to 42V. This card is connected by cable, two-way, to an NI connection box, model BNC-2120, which allows the use of coaxial cables from displacement and force sensors. Since these signals are characterized by a potential difference between their terminals, they were connected in differential mode, without reference to the electrical network (CS) to avoid noise from it.

The board alone does not have the ability to process the signals, only receives the electrical signals and delivers a digital signal to the output. As such, in order to control the card and record the data acquired on it, it is necessary to develop a program with LabVIEW software. In this program, it is possible to create a graphical interface that allows the user to view the process variables in real time, such as the distance between the compression plates.

All instrumentation necessary for the conditioning and acquisition of electrical signals associated with force and displacement sensors was kept in a mobile car (illustrated in the figure 3.11) to facilitate the entire assembly of the sensor system and data acquisition.

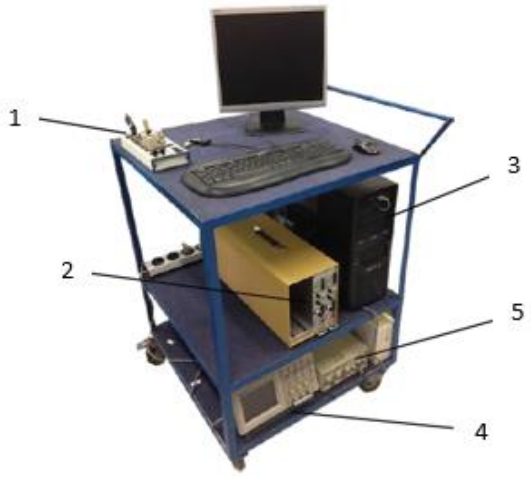

Figure 3.11 - Mobile car with sensory system equipment. 1- Data acquisition board; 2- Amplifier; 3- Computer; 4- Oscilloscope; 5- Generator of functions [Gregorio, 2017].

3.2.5. Muffle Oven

To allow a more comprehensive study of the characteristics of the specimen material, the assembly of a muffle furnace was designed, a type of kiln consisting of a metal chamber with internal coating of refractory material, i.e., capable of maintaining its resistance to high temperatures, which can reach temperatures in the order of magnitude of 1000ºC.

In this way, it will be possible to test samples in SHPB at higher temperatures. In the case of ballistic vests, simulate scenarios conductive to the use of such in environments other than room temperature.

The muffle used is branded Könn GmbH, type STE12SO and number A787/01, and its characteristics are shown in table 3.1.

Table 3.1. Features of the muffle oven.

Nominal temperature (ºC)	1000
Nominal voltage (V/Hz)	25
Nominal power (kW)	750
Nominal current intensity (A)	30

From the previous table it is observed that the rated current intensity is 30 A, however, the network present in the Machining and Micro-Manufacturing Laboratory (LabM3) provides only 16 A.

To overcome this obstacle, a transformer (Variac) of model TDGC2 - 10KVA was used in order to modify the voltage and electrical current levels, keeping the electrical power practically constant. This device works by inducing current according to the principles of electromagnetism, that is, where it is stated that it is possible to create an electric current in a circuit once it is subjected to a variable magnetic field, and it is because it requires this variation in magnetic flux that transformers only operate in alternating current. Therefore, by connecting one of the terminals to the current by a single-phase plug and the other to the oven, surpasses the problem of the incompatibility of the oven with the supplied electrical main.

In the process of integrating the oven into the machine, it is necessary to ensure that it is possible to assemble/disassemble the furnace of the apparatus, thus obtaining two possible configurations. To do this, it was used a set of guides similar to a drawer. The stationary guides are centered and fixed to the two vertical plates of the test zone with the central holes 20 mm from the surface of the horizontal plate, as indicated in the CAD model of figure 3.12 (a). Then, an aluminum plate at the base of the oven was glued with cyanoacrylate and two holes were made on each side where the rivet guides were fixed.

Finally, the oven can be fitted between the vertical plates in such a way as to situate its output and input concentrically with the incident and transmitting bars when necessary, and removed when this is not the case (figure 3.12 (b)).

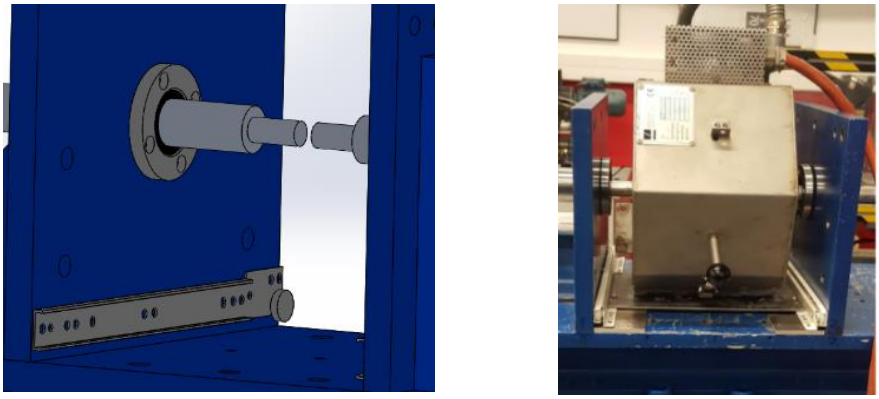

(a) (b)

Figure 3.12 - (a) CAD model of the oven guides; (b)Installation of the muffle in the probe area.

To understand the operation of the oven and how to control the temperature inside, a calibration of the temperature variation with the voltage applied to the transformer was introduced. The equipment used in this study is: (i) muffle oven; (i) transformer; (iii) thermocouple probe; (iv) digital thermometer.

The digital thermometer, model TM-902C, type K, with a temperature measurement range from -50ºC to 1300ºC (figure 3.13 (b)), is connected to a thermocouple probe with a metal cable that is placed inside the oven that will detect its temperature and transmit it to the thermometer (figure 3.13 (a)).

The tests consisted of varying the voltage of the 5V transformer and reading the temperature in the thermometer after 5 minutes. After recording the temperature, turn off the variac and wait for the ambient temperature to reach in the oven. The process was repeated until the 700ºC was exceeded, which were reached at 40V of voltage. The voltage in the transformer was also varied up to 120V, a value at which the electrical frame shoots, to ensure a safety limit.

The procedure for how to use the assembly (transformer and oven) as well as safety measures to be taken and calibration results can be found in the annexes section under "Operating conditions of variac TDGC2 – 10KVA" and "OVEN KONN GmbH - Procedure".

.

(a) (b)

Figure 3.13 - (a) Muffle furnace with thermocouple probe; (b) Digital thermometer.

3.2.6. Pneumatic Gun

The propulsion system chosen for SHPBs dynamic high-speed compression tests was pneumatic gun (figure 3.14). This is essentially composed of a pressure tank and a tube that allows the guiding and acceleration of a projectile. The drive of a valve allows the pressurized air in the tank to flow into the barrel, propelling the projectile.

Figure 3.14 - Pressure thank and valve connected to a tube by a vertical plate.

The energy available for the compression test is related to kinetic energy,E_c, this is a function of velocity and mass of the projectile.

Due to the violence of the impact, the energy of the shot needs to be carefully calculated to prevent the remaining compression energy from damaging any element of the tool or sensors. The pneumatic gun allows it to easily propel projectiles to ballistic speeds (greater than 100 m/s) and, once energy evolves with the square of velocity, high impact energies are easily obtained for small variations of the projectile velocity.

The projectile when animated with kinetic energy travels through the tube, being part of this energy dissipated due to the pressure that the resistance of the air exerts inside in front of the projectile. To minimize this dissipation component, four holes were drilled near the outlet allowing the pressurized air to exit, illustrated in figure 3.15.

Figure 3.15 - Illustration of tube with holes for air outlet.

The tube assembly (5) to the compressed air tank (1) is fixed by a steel cylinder (tank holder) (2) with passing holes on the periphery on one side of the vertical board (3) and the tube fixed by a retaining part (4), on the other side, with the same effect as a "retaining ring", in a way that it does not allow the tube to move during the shooting. The vertical board is fixed on a horizontal board with the help of two small triangles and clamps that secure the assembly to the base beam of the machine. The tube is then attached to a multi-piece bearing. The tube outlet is mounted to the inner ring (8) and the tube ring (9), these in turn are fitted to the male hydraulic support (11) that secures the assembly to the vertical board with a window (10) with the proper clearance to allow the longitudinal movement of the smooth bar, without compromising its guidance. The outer ring (7) is screwed between the male and female hydraulic supports (6). The bearing/bar assembly was then oiled to form a thin lubricating film and reduce friction in the contact interface. The incident bar can be at a distance between 0 and 50cm from the tube outlet. The figure 3.16 represents a CAD model of the parts that make up the pneumatic gun and its assembly sequence. There are two variables that can be controlled, the velocity through the pressure set in the air tank and the mass of the projectile. A valve, visible in figure 3.13, controls the pressure in the air tank. Compressed air can be injected by a conduct present in the laboratory or by the use of a compressor.

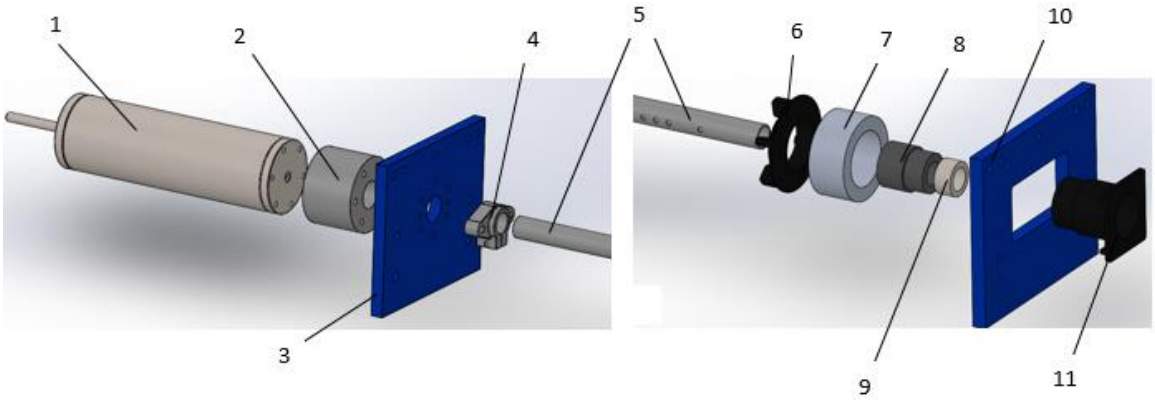

Figure 3.16 - CAD model of the set of mounting parts of the pneumatic gun to the machine: (1) Air thank; (2) Tube holder; (3) Vertical board; (4) Tube retainer; (5) Tube; (6) Female hydraulic support; (7) Outer ring; (8) Inner ring; (9) Tube ring; (10) Vertical board with window; (11) Male hydraulic support.

In the manufacture of the projectiles, on the other hand, it was used brass and steel alloy bars which, taking into account their different densities, were weighed and then machined to change their mass to the desired value. However, cylindrical projectiles must have the diameter as close as possible to the inner diameter of the tube, 30mm, so that the air resistance is minimized and only their length is variable, so the larger mass projectiles have a longer length, explicit in figure 3.17. The desired mass values of projectiles are 250g, 500g, 1000g, 1500g, 2000g and 3000g.

Figure 3.17 - Cylindrical projectiles with masses 250g, 500g, 1000g, 1500g, 2000g, 3000g (bottom to top).

With the length increase of the projectile, it was found that the friction felt in the walls of the tube also increased, which leads to a greater dissipation of energy in the shot despite the increase in mass. To minimize this factor, oil was applied to the surface of the projectiles in order to act as a lubricant. The process of changing the projectile is done through two Bosch profile bars on the sides under the horizontal plate (one on each side) that act as sliding guides along the base beam. When changing projectiles, the user must unscrew the clamps that join the horizontal board with the base beam and then pull the vertical plate backwards in order to move the entire gun assembly backwards. Once in the position of figure 3.18 (a), the projectile in the tube can be removed and its replacement placed and pushed until it is in contact with the tank outlet. When the projectile is in position, the pneumatic gun assembly must be pushed forward in the position of figure 3.18 (b) ready to fire.

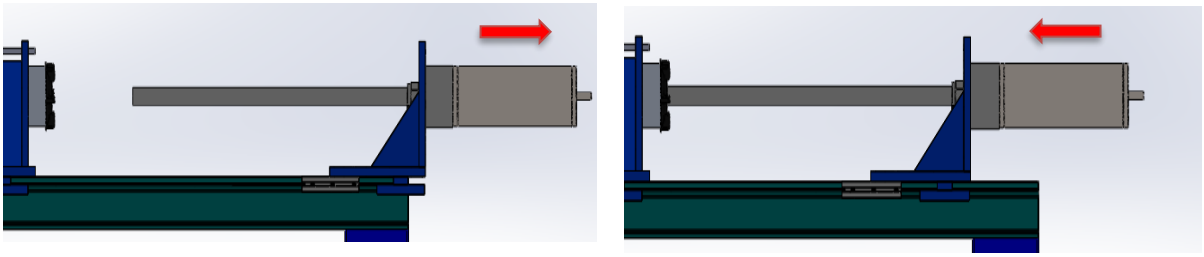

(a) (b)

Figure 3.18 - Pneumatic gun assembly: (a) Projectile exchange position; (b) shooting position.

3.3. High Speed Camera

Dynamic tests are performed at high speeds, so analyzing the various moments over the impact becomes a very difficult task. To study the impact on the specimen in more detail, a high-speed camera was used with the aim of capturing as many frames as possible. The high-speed camera generates a significant amount of heat that must be dissipated to prevent its damage. To do so, it is fixed in the center of a board with a number of fins that allows a greater exchange of heat with the outside.

This structure, in the test area, is installed with four retaining rings on the two vertical boards. Allows the change of the angle and longitudinal and lateral position of the camera. It is to be taken into account the position of the camera in order to frame the specimen and the impact. The set was modeled

in the Solidworks software in CAD, shown in figure 3.19, verifying the best position and angle of the camera.

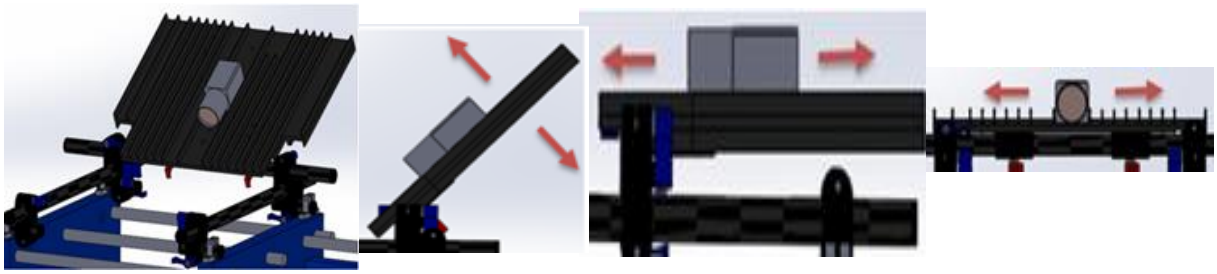

Figure 3.19 - CAD model of the high-precision camera mounted on the dissiater plate and support structure with possible angular, longitudinal and lateral displacements.

3.4. Velocity Sensor

The most significant parameter to evaluate, in order to determine the energy of the impact, is the velocity of the projectile. It was necessary to develop a sensor that measured this velocity, detecting the movement of the projectile at two different points. On the market, there is already instrumentation for this purpose as the case of the ballistic chronograph, a device that measures the speed of ballistic projectiles.

Nowadays, a modern ballistic chronograph consists of two sensory areas, "chronograph windows", optical sensors (photosensors) that detect the passage of the projectile when it passes through the two windows. Subsequently the linear velocity of the projectile is calculated according to the well-known expression:

$$v = \frac{\Delta x}{\Delta t} \tag{3.1}$$

Where Δx is the distance between the two windows and Δt the time from the moment the projectile passes the first window until the moment it reaches the second window (calculated electronically).

3.4.1. Developed Sensor

The given experimental circumstances do not allow the use of the existing ballistic chronograph on the market, so it was necessary to project a speed sensor, with functions similar to those of the chronograph, adapted to this situation that would allow the high values of impact velocity of the projectile to be calculated accurately.

The sensor structure was first developed in a CAD model (figure 3.20 (a)) and then assembled with physical parts (figure 3.20 (b)). The electrical component of the sensor consists of two receptor photodiodes and two emitting diodes (LED). Each photodiode is directed to one of the LEDs, which emit a light concentrated in that direction when connected by the corresponding switches. When the projectile interrupts this beam of light, will vary the voltage originated by the LED on the photodiode. By the same

principle as the original ballistic chronograph, with the connection to an equipment, that detects the voltage variations in time and knowing the distance between the two photodiodes, it will be possible to calculate the speed of the projectile with equation 3.1.

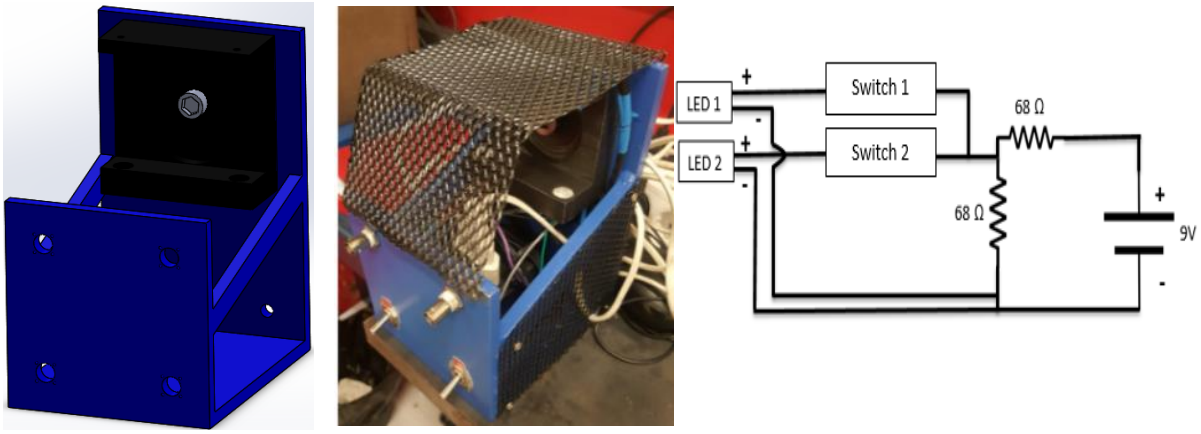

(a) (b) (c)

Figure 3.20 - (a) CAD model of the velocity sensor; (b) Photo of real model of speed sensor; (c) Electrical circuit diagram of LEDs.

3.4.2. Equipment

In order to measure the voltage variations in the receptor photodiodes is used an Agilent Technologies oscilloscope, model DSO1004A, of 60MHz frequency.

One of the photodiodes is connected to channel one and the other to channel two, allowing the oscilloscope to read and show two different signals on the screen. The voltage range of both channels must be tuned to 500mV, taking into account the light intensity of the LEDs, so that variations are visible. In order to be able to capture those voltage variations in time, the range should be 200µs. The procedure of how to define the oscilloscope to capture the voltage variations in the two photodiodes can be consulted in the section of attachments under "Measuring time in the Agilent Technologies oscilloscope, model DSO1004A".

Three 1.5V batteries powered the LEDs used, originally from a cylinder with four LEDs, so their intensity should not exceed 4.5V. The glass present in these LEDs was also used, which focused the light coming from them in a direction increasing the energy provided to the receiving photodiode making the voltage variation more visible in the oscilloscope. With the help of a grinding wheel, two of the necessary LEDs were removed and the grinder redefined the shape of the surrounding polymer to adapt to the sensor.

The transformer used to supply power to the circuit had a voltage of 9V, so it was sought to use resistances to change this value. In the circuit to be used, the two resistances were placed in series and the two LEDs in parallel with one switch each, as shown in the diagram in figure 3.20 (c). Based on the fundamental principles of electrical circuits, it was decided to keep the LEDs in parallel so that the voltage supplied by the power supply altered by the resistances was the same for both LEDs.

It is necessary to ensure that the voltage passing through the LED terminals is higher and close to 4.5V, since the intensity of the LED should be the highest possible, without overpowering it, since the photodiodes do not register very high voltages. The method of trial and error was used in in order to get the right resistances, in a breadboard, reading the stress value between the terminals in a multimeter until reaching an acceptable value. The available resistances used had the values of 10Ω, 15Ω, 22Ω, 33Ω and 68Ω. After the various attempts of different combinations of two resistances, it was concluded that the set of resistances that best adapted to the needs of the sensor was two resistances of 68Ω, which reduced the initial voltage of the transformer by 5V for each LED. The electrical wires were connected to the power supply terminals, resistors, switches and LEDs via a welding iron and then insulated with insulating tape.

3.4.3. Assembly

After the circuit assembly, the receptor photodiodes and LEDs were inserted into a polymeric support in two pairs of concentric holes, in order to create a line of a beam of light.

The mentioned set was then inserted with an M14 screw in a metal support that was later adapted to the necessary functions. At the front, the two upper holes were used to place two BNC inputs that allow the connection to the oscilloscope and in the two lower holes, the two switches were placed to turn the respective LEDs on/off. The electrical cables were placed inside the metal support.

For protection and aesthetic reasons, a protective net was used, with defined measurements, cut with the grinding wheel, with a removable part on the sensor and two others fixed to the sides of the metal support with an entrance on one side for the passage of the electric cable that allows connection with the power supply.

3.4.4. Calibration

The projectile, when shot, moves inside the pneumatic gun barrel, so tracking its movement can be a complicated task. Analyzing the tube structure, taking advantage of the four holes for the air outlet, the sensor is placed so that the tube passes through the structure that supports the sensors and the LEDs so that the beam of light passes through the tube through the holes and is sensed by the photodiodes. In this way, as soon as the projectile is shot it will interrupt the light beam as soon as it passes between the holes, varying the potential difference identified by the photodiodes that is read by the oscilloscope, connected to the BNC inputs of the metal support. Following the steps of the procedure "Measuring time in the Agilent Technologies oscilloscope, model DSO1004A", after the test, it is obtained the time it takes for the projectile to move between the sensors. Knowing that the distance between sensors is fixed (72mm), calculating the speed becomes possible using equation 3.1. The scheme in figure 3.21 represents the operation of the speed sensor in the SHPB tests.

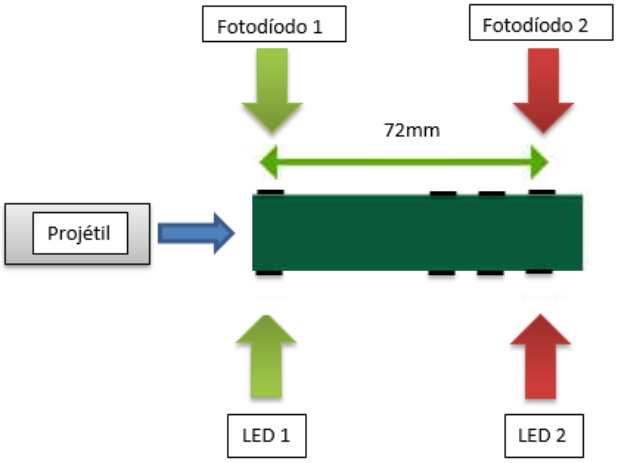

Figure 3.21 - Scheme of the assembly of the projectile and speed sensor in the SHPB.

In order to analyze how the velocity varied with the pressure imposed on the compressed air tank, it was necessary to perform a calibration with different points of pressure for the projectiles considered.

Figure 3.22 is a graph that shows, in a more transparent way, the relation between the projectile velocity and the pressure of the air tank.

Naturally, the lighter projectile will achieve higher velocity values for the same pressure, although it is important to highlight that all the projectiles curves follow the same type of empirical model, i.e., they all progress according to a power equation, which leads to higher increments of pressure in order to increase a unit of velocity. This is due to the fact that the faster the projectile goes inside the gun barrel, the harder it will be for the air inside, in front of the projectile, leave the barrel, which will lead to higher air resistance to the projectile movement. Therefore, the best projectiles to be used are the ones with the highest mass, 3000g or 2000g, since the lighter ones can be a hazard to the machine due to the violent impact intensity for small pressure values.

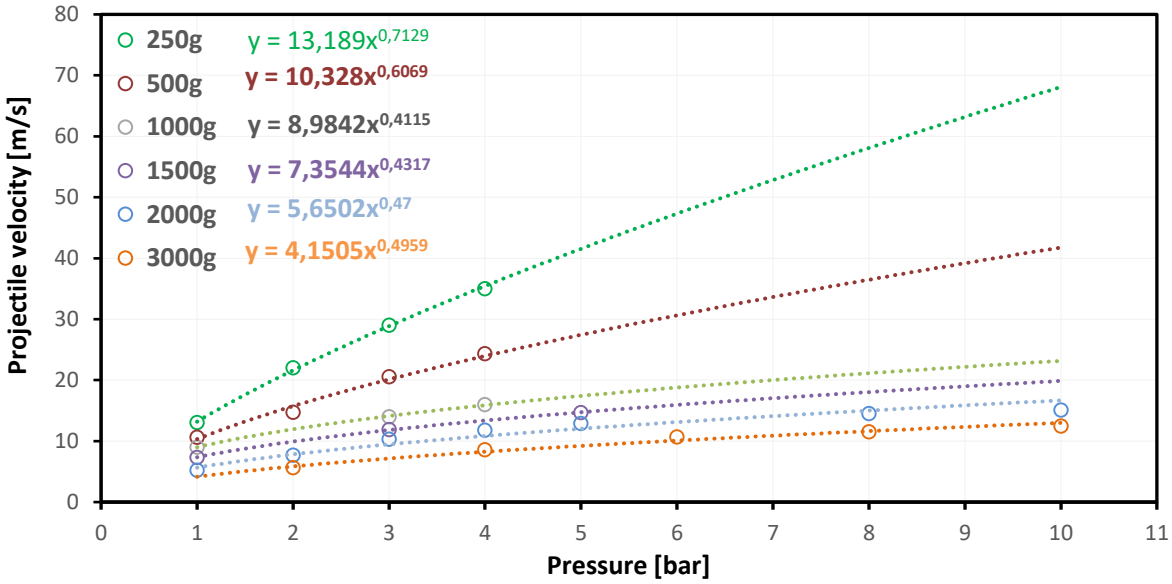

Figure 3.22 - Variation curves of the projectile velocity with the tanks pressure for the different projectiles.

It is also important to bear in mind that the impact energy of the projectile depends only of the pressure applied in the tank, just like a springs release energy depends of the pressure applied to it and not to its mass. According to the figure 3.23, the increase of pressure follows a logarithmic empirical law that leads to higher increments of pressure in order to achieve a unit of energy.

While the velocity of the projectile is related to its mass, i.e., the potential energy is transformed into kinetic energy, as explained before, the heavier the projectile the slower his movement to the same pressure point.

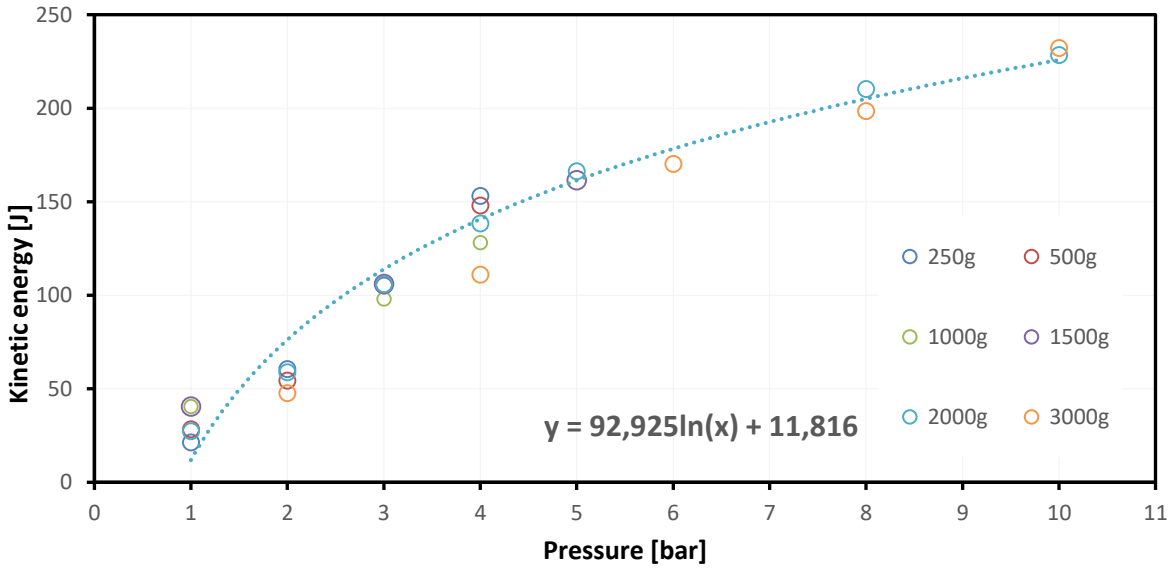

Figure 3.23 - Variation of the impact energy with the pressure for the different projectiles.

4. Experimental Results

The objective of these experimental results is to determine the difference of energy absorption capabilities between dry and impregnated plain-woven aramid for a wide range of layer stacks and different impact velocities at room temperature by comparing the residual energy that passes through the woven.

It is important to keep in mind that the penetration effect of a bullet is out of context in these experiments. It is only considered the energy the bullet carries assuming there is no penetration of the aramid fabric. The figure 4.1 displays an example of aramid fabric after the impact in an experimental test.

Figure 4.1 - Plain-woven aramid after impact test.

In the uniaxial compression tests, through the strain gauges, it is obtained the load values applied to the sample, while with the pair of coils, the displacement values. With the two parameters values collected, it becomes possible to build a graphic load-displacement enabling a better understanding of the relation between both.

It makes sense to vary the number of stacked layers as a parameter when the subject test is textile sample. Since the residual energy of a bulletproof vest upon impact, for instance, is significantly influenced by its textile layers, it is of most interest include this parameter in the experimental research.

4.1. Dry Aramids

The first set of experimental tests was followed by the use of non-impregnated or dry aramids for different layer sets and impact velocities caused by different pressure gradients in the air tank.

The curves, represented in the following graphs, however, follow an unusual representation as function of distance between compression plates. This is due to indefinite geometry of the aramid fabrics being quite different from solid perfectly cylindrical shape of the traditional uniaxial compression specimens that are easy to measure its thickness, unlike woven materials that turn out to be very complicated to establish a thickness value due to its lack of density and rigidity. Nevertheless, residual energy is still calculated by integrating the force-displacement curve per unit of length between the two compression plates. Therefore, from the information drawn from the different curves, it is noted that the absorption capability increases with the impact velocity and number of stacked layers, as it was expected. Further, it will be discussed each velocity condition with dry and impregnated aramids for the different set of layers.

Within each different number stacked layer group, it was tested different velocities for the projectile. It is assumed that the distance between plates as the distance between the moment the compression plates contact the specimen, and the moment they stop. It is important to refer that throughout the tests, the peak force achieved for the different ply numbers vary with the three projectile velocities considered.

At *quasi-static* conditions, the peak force generally increases with the ply[3] number. With 1 layer stack, the peak force is $\approx 23\ kN$, while stacking 16 layers increases the peak force to $\approx 37\ kN$, i.e, there is an increase of 35,1%.

[3] layer of material which has been combined with other layers in order to provide strength

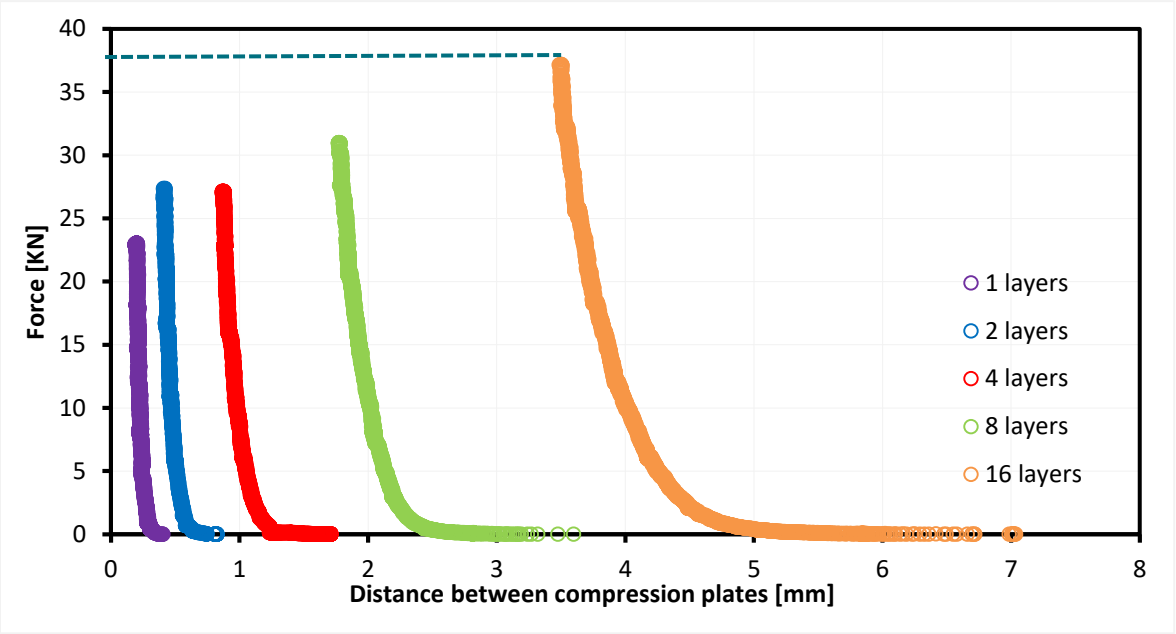

Figure 4.2 - Change of the peak force through the different ply numbers of dry aramid at quasi-static conditions.

Following the principle that the force applied on the aramid fabric increases as the distance between the compression plates decreases, it is natural to assume that the nominal stress will increase as well. The curve on the figure 4.3 describes that fact as compression on the sample increases so does its nominal strain, for all the ply number sets. It is also relevant to mention that nominal stress is insignificant until the nominal strain achieves a value of $\approx 0{,}3$. From there on, the aramid fabric begins to generate a considerable amount of resistant to the compression the plates are applying preventing the sample from increasing its nominal strain. It is also noticeable that the high ply numbers leads to higher stifness values of the composite. That can be proved with the increase of the curves slope with the increase of aramid layers.

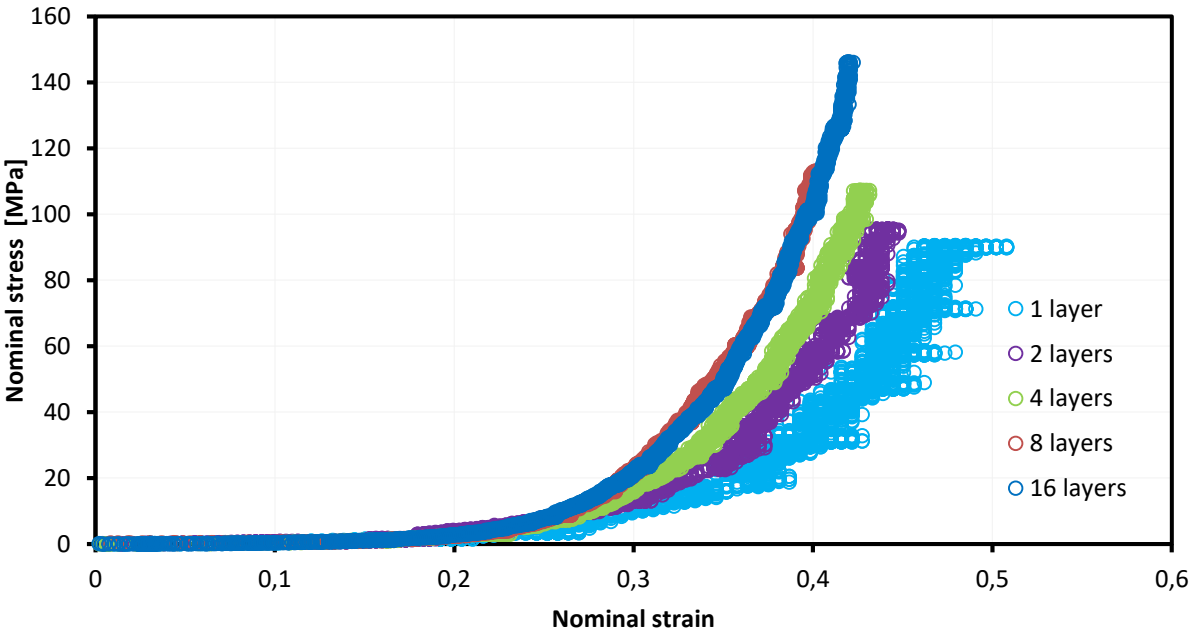

Figure 4.3 - Stress-Strain curve for the different ply number sets at quasi-static conditions.

When testing with 3m/s, with the pressure of 1,7bar in the air tank, the ply number has little to no effect on the peak force. The figure 4.4 shows that particular fact, the peak force remains constant throughout the layer stacks, achieving a value of $\approx 12kN$.

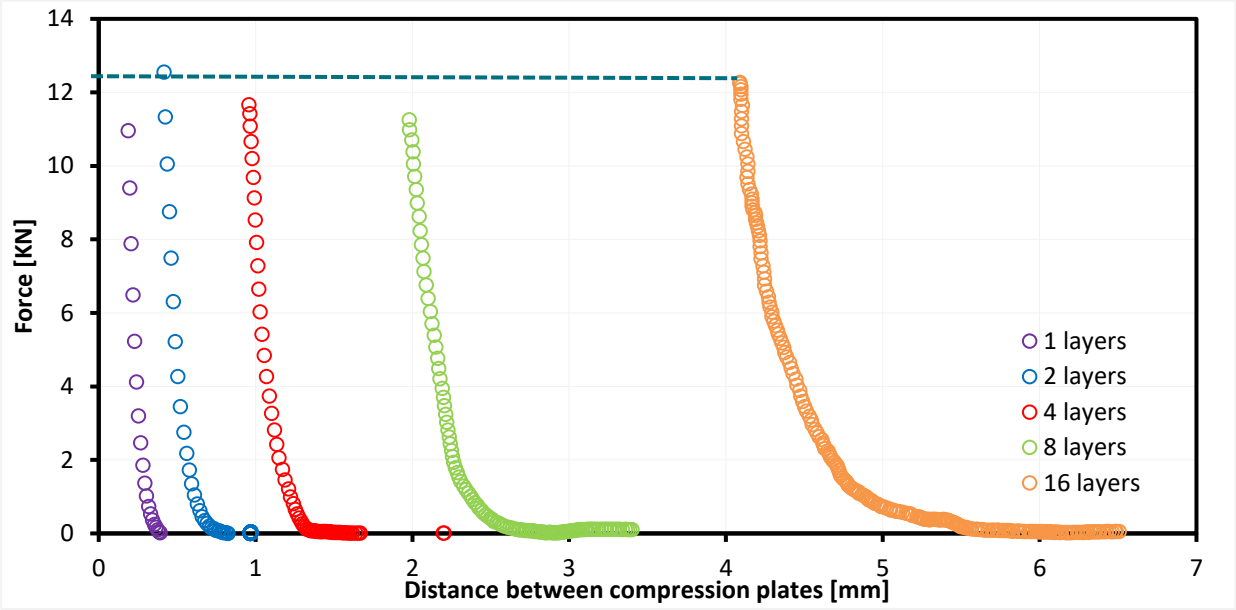

Figure 4.4 - Change of the peak force through the different ply number sets of dry aramids with at 3m/s.

As it was analyzed at *quasi-static* conditions, at 3m/s, the nominal stress also increases with the nominal strain after the $\approx 0{,}3$ value. Likewise, in dynamic conditions, more layers of aramid fabric lead to a decrease of the strain rate.

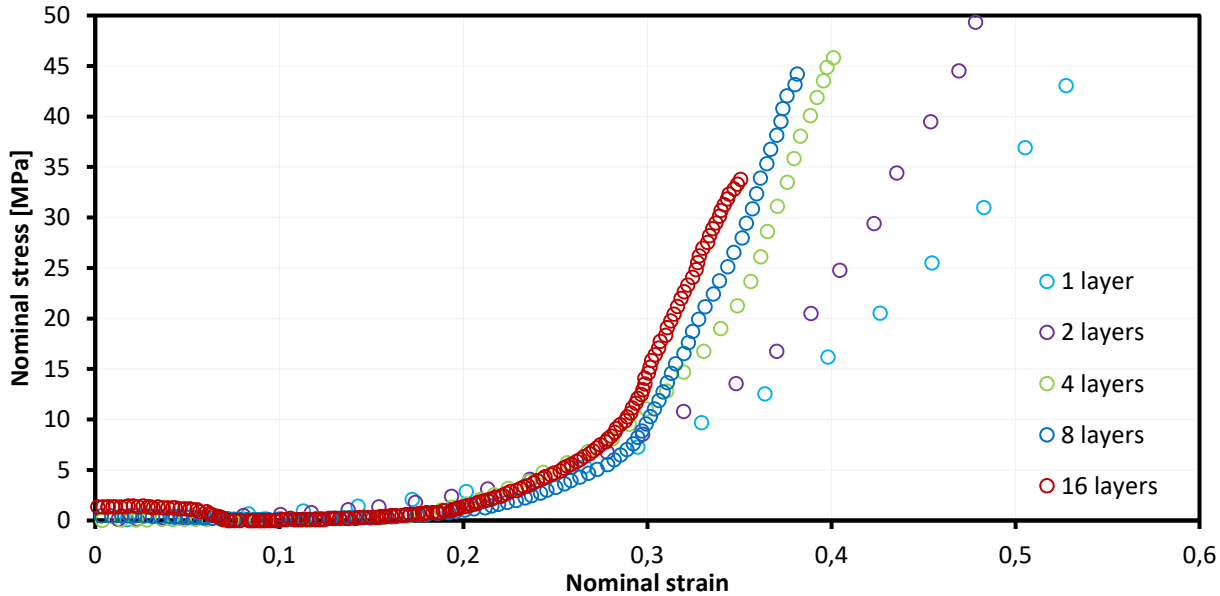

Figure 4.5 - Stress-Strain curve for the different ply number sets at 3m/s.

At 10m/s, with 4bar at the air tank, the peak force is also constant with the ply number but its absolute value increases to $\approx 30kN$, 250% more than at low strain rate conditions. Naturally, higher strain rate conditions lead to a bigger peak force for every layer stack. To prevent possible damages on the apparatus components, it was not performed tests on aramid fabric with one layer at 10m/s, since the sample has a too small thickness and the impact could rapidly become dangerously violent.

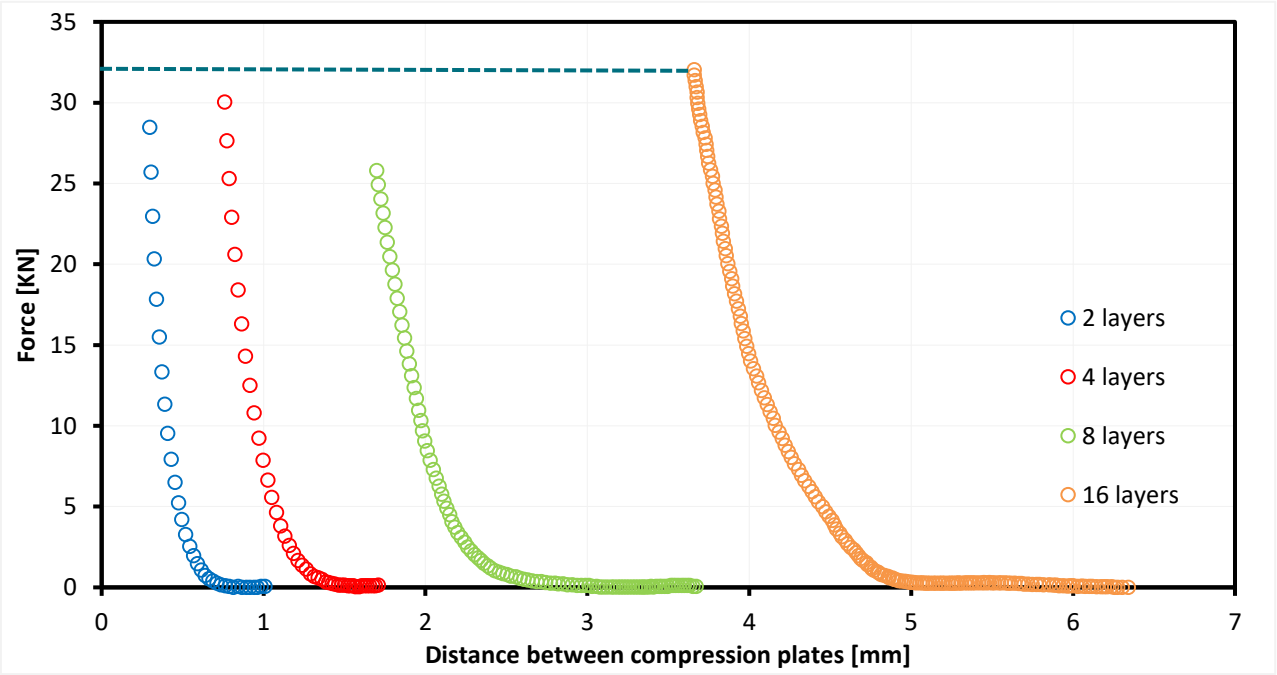

Figure 4.6 - Change of the peak force through the different ply numbers of dry aramid at 10m/s.

With a velocity of 10m/s, the difference of slopes between the different ply number curves of nominal stress-strain is bigger, leading to a wider variation of damping throughout the different layer sets, as it can be observed in the figure 4.7, similar behaviour to the previous strain rate condition.

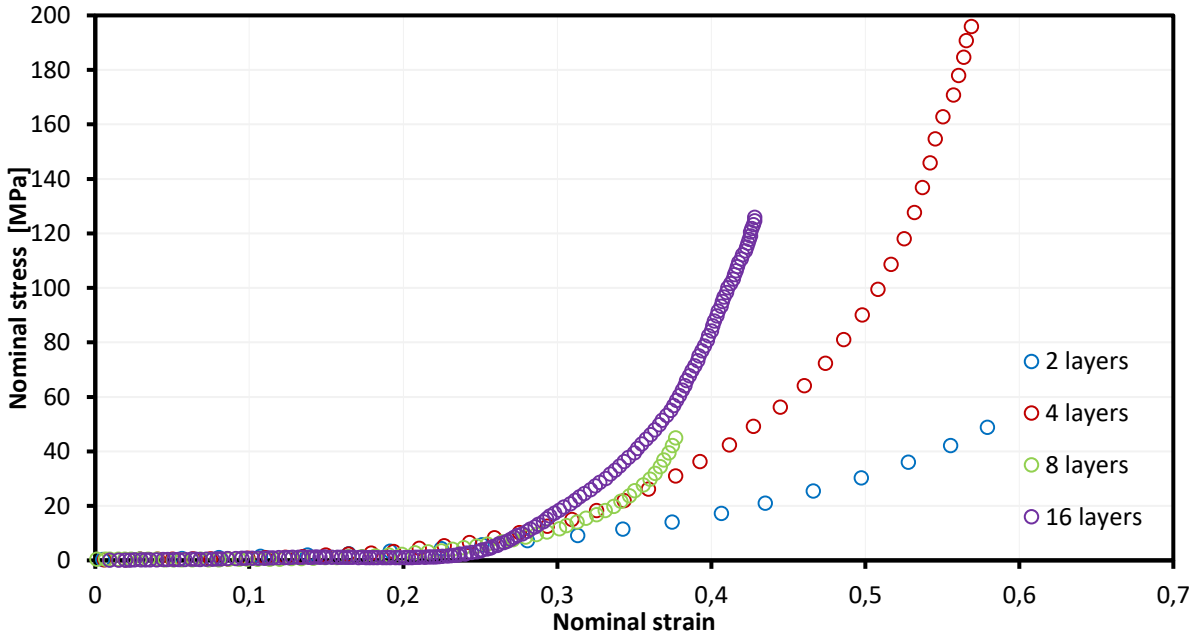

Figure 4.7 - Stress-Strain curve for the different layer sets at 10m/s.

The figure 4.8 represents the variation of residual energy detected by the load cell after the aramid fabric with the ply number at *quasi static* conditions, low strain rate and high strain rate. As well known, the higher the impact velocity, the bigger quantity of energy is envolved and, therefore, the more energy is absorbed and also the one passing through. The residual energy decreases with the increase of the number of layers, ranging values from 1,52J with 2-ply to 0,2 J with 16-ply at 10m/s. However, in order to relate the parameters that influence these remaining energy, it is used a model equation to describe the curves behaviour between layer stacks for every velocity condition.

All the curves share the same characteristic by having an asymptotic behaviour. The ideal case would be the non-existence of residual energy, therefore, the more layer stacks are applied, the closer it gets to that utopia. However, the increments of residual energy decreased will be smaller as the ply number increases, leading to insignificant decreases at very high number aramid fabric layers. This will enable the determination of empirical models that can represent that behaviour.

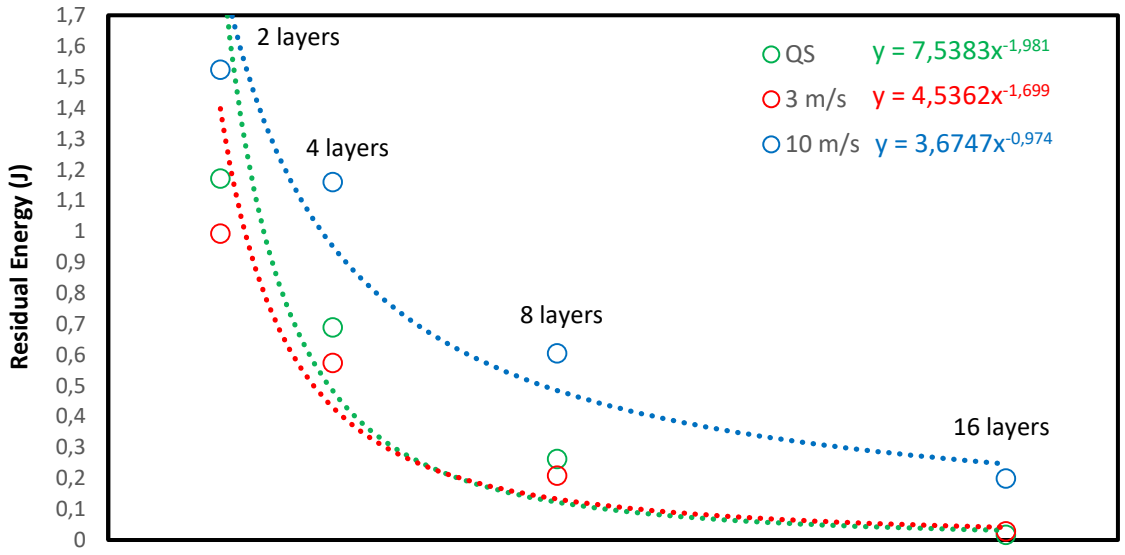

Figure 4.8 - Evolution of the residual energy with the ply number at quasi-static, low strain rate (3m/s) and high strain rate conditions (10m/s) in dry aramids.

4.2. Impregnated Aramids

In order to seek a higher energy absorption capability, it was applied an impregnating agent to the aramid fabric in order to achieve a more rigid structure.

The material employed in the experimental tests was a SiO_2 impregnated aramid fabrics. The SiO_2 nanoparticles based shear thickening fluid (STF) suspension was made by the mixing of SiO_2 nanoparticles (Aerosil 200) and polyethylene glycol (200 M) in a 70:30 ratio. Subsequently the aramid fabrics were impregnated and passed through pressured roles in order to remove the excess of fluid. The load–displacement curves were obtained by means of the same tests in *quasi-static* conditions and dynamic conditions applied to the non-impregnated aramid fabrics.

The figure 4.9 shows the behaviour of the different ply number impregnated aramids when submitted to a load in *quasi-static* conditions. It is relevant to notice that, in these conditions, it does not have a significant difference from the dry aramids in figure 4.2, having approximately the same peak forces for the same ply numbers.

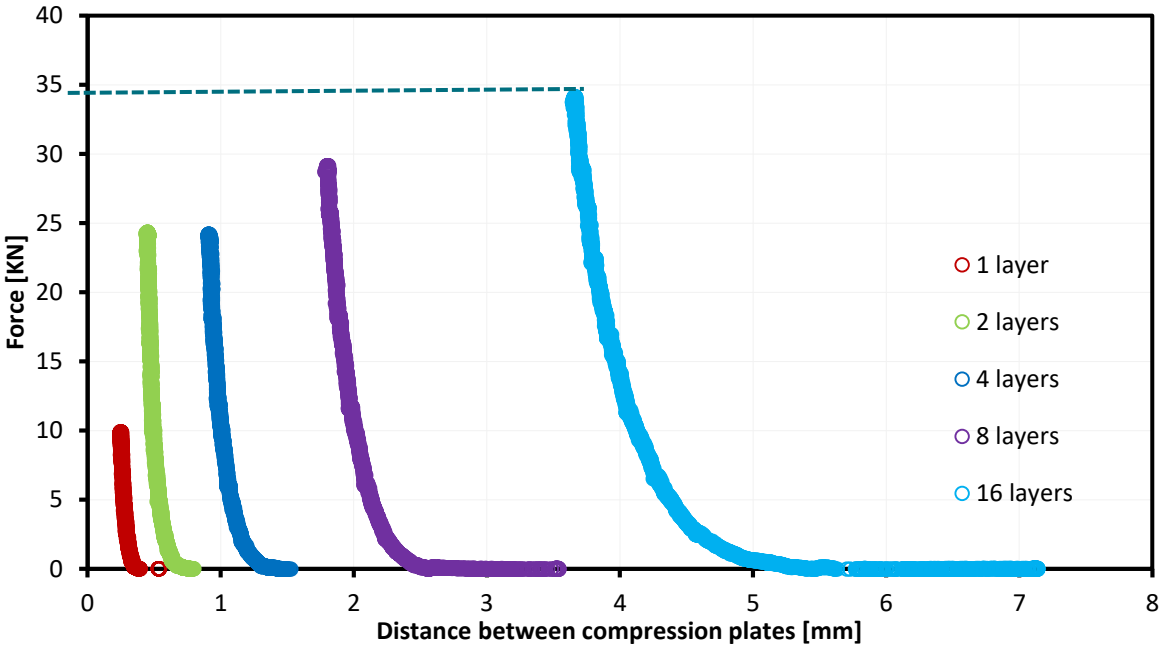

Figure 4.9 - Change of the peak force through the different ply numbers of impregnated aramid at quasi-static conditions.

Regarding the nominal strain-stress, just like the force-distance between plates relation, there is no significant difference between impregnated and non-impregnated aramids at quasi-static conditions. The figure 4.10 proves that fact, displaying lower nominal strain values for higher ply numbers, similar to the ones found in figure 4.3.

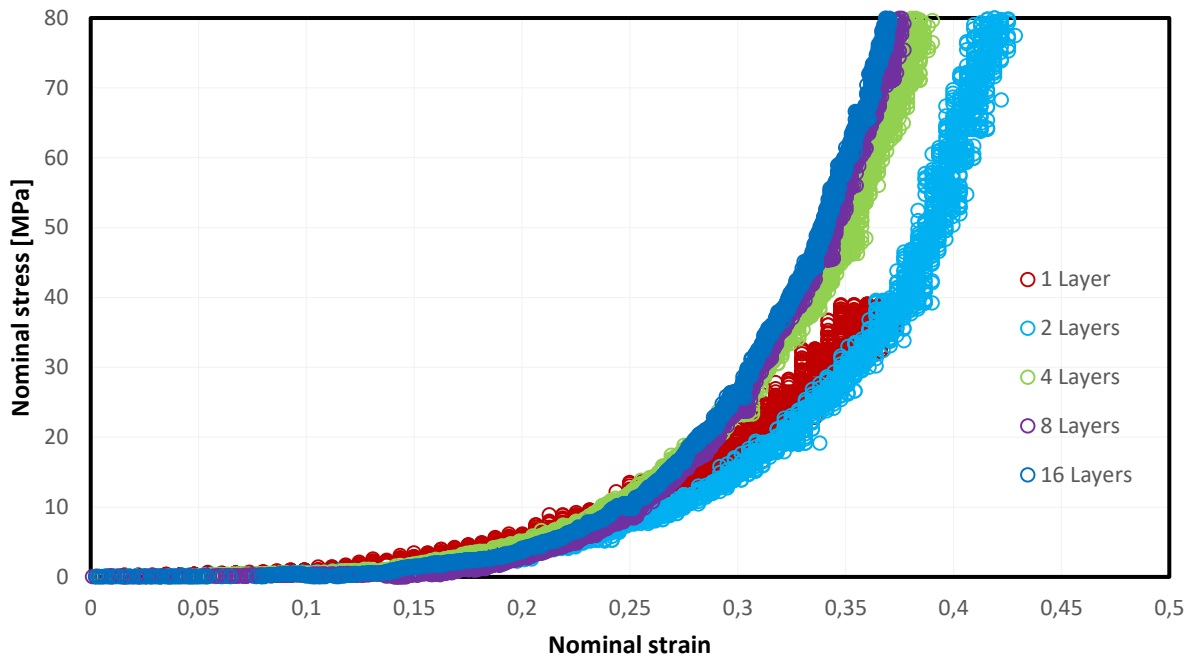

Figure 4.10 - Nominal Stress-Strain curve for the different ply number sets of impregnated aramids at quasi-static conditions.

However, when submitted to dynamic loads with a kinetic component, the impregnated aramids behave differently than the dry ones leading to different results displayed by the experimental tests. The figure 4.11 shows that difference, at 3 m/s, particularly with the 16-ply in which with dry aramids the peak force is $\approx 12kN$, while the impregnated one is $\approx 4kN$, a $\approx 66\%$ decrease. The reasoning behind these results is that the impregnated fluid acts as a solid when submitted to impact, increasing the materials density naturally, increasing, therefore, its capacity to absorb energy. Furthermore, in dry aramids tests, the peak force for low strain rates is constant for all the ply numbers while in the impregnated aramid fabrics, the higher the ply number the lower the peak force.

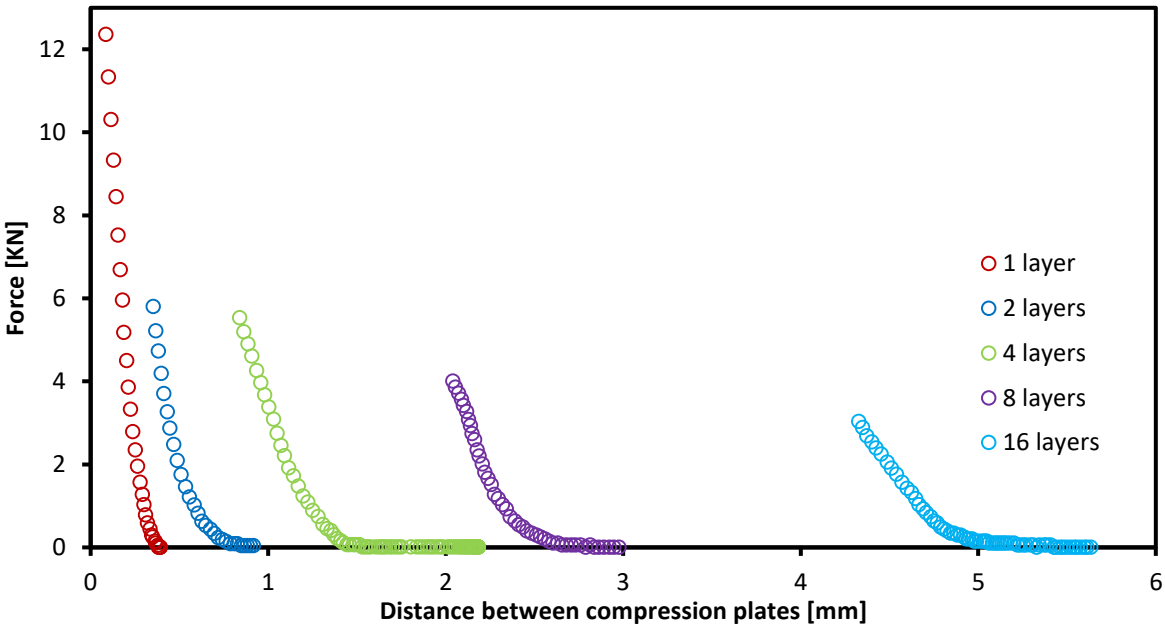

Figure 4.11 - Change of the peak force through the different ply numbers of impregnated aramid at 3m/s.

As expected, in the figure 4.12, the nominal stress achieves lower values for same nominal strain values. This result demonstrates the importance of impregnation of specific nanoparticles in the aramid fabrics in order to increase the resistance of the sample to the impact.

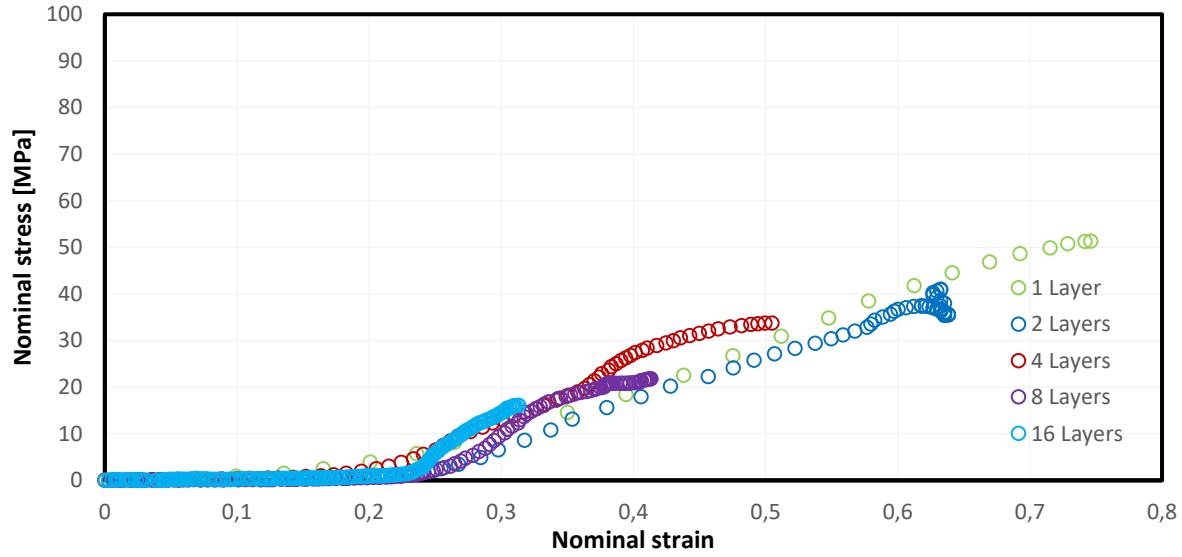

Figure 4.12 - Stress-Strain curve for the different ply number sets of impregnated aramids at low strain conditions (3m/s).

A similar conclusion can be drawn to the high strain rate conditions. As seen in the figure 4.13, the peak force at 10m/s for the 16-ply is $\approx 11kN$, while the non-impregnated aramids is $\approx 30kN$, a $\approx 63\%$ decrease. Showing, once again, that the impregnated aramids lead up to three times smaller peak forces than the non-impregnated ones.

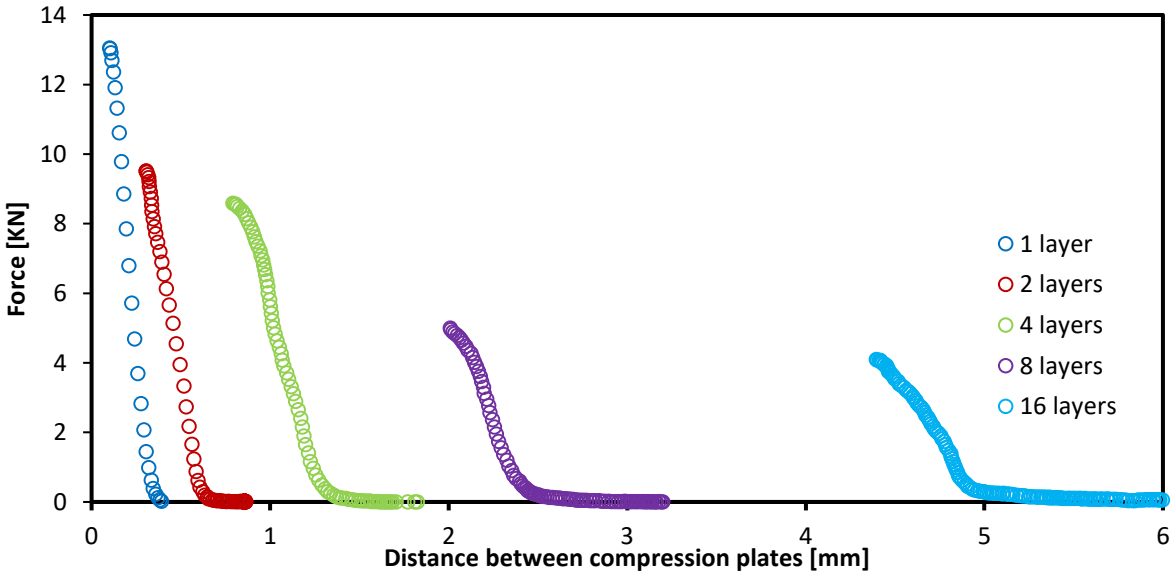

Figure 4.13 - Change of the peak force through the different ply numbers of impregnated aramid at 10m/s.

Even though, at high strain rates, the nominal stress achieves bigger values than the low strain rates, the values are still inferior to the ones observed on the non-impregnated aramids in the same conditions.

Results show the combined influence of displacement and strain rate (quasi-static, low and high strain rate) in the overall load response, and indicate that aramid fabrics presents significant layered structure sensitivity. The nominal flow stress can be determined by the load evolution considering the compression plate's area as a constant value. All calculated nominal stress-strain curves show now good agreement, mainly because there is not an asymptotic value in the experimental data. This is expected to show up as deformation increases and material becomes denser.

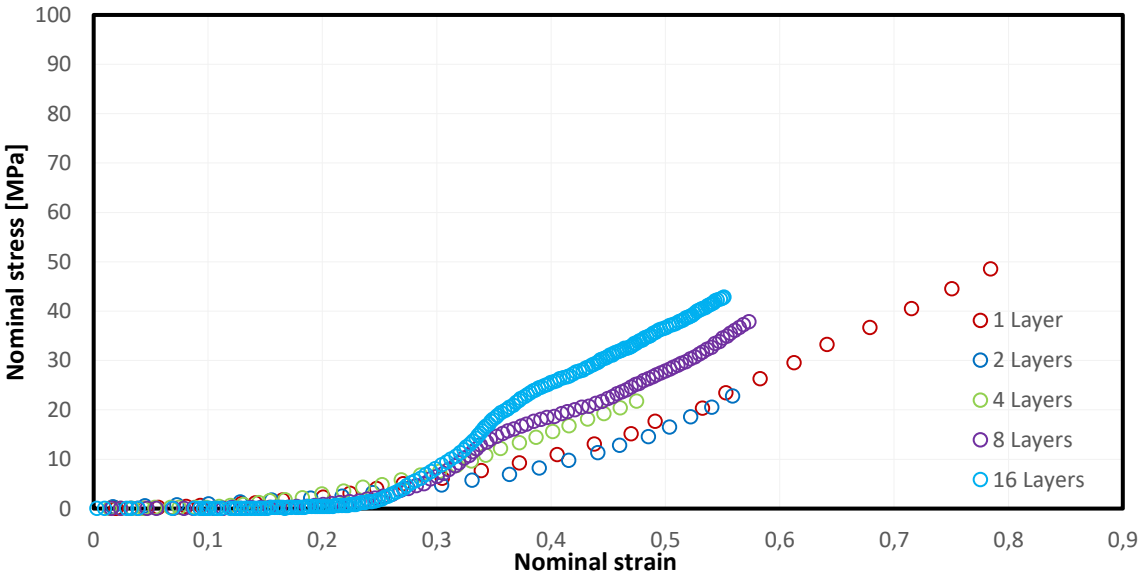

Figure 4.14 - Stress-Strain curve for the different ply number sets of impregnated aramids at high strain conditions (10m/s).

Shear thickening fluid, in this case SiO_2, is a fluid, which behaves like a solid when it encounters mechanical stress or shear. Thus, STF behaves like a liquid until an object strikes or agitates it forcefully, as demonstrate previously.

The impregnated aramids, at *quasi-static* conditions, behave the same way as the dry aramids since the effect generated by the STF only occurs with dynamic loads.

With dynamic loads, the difference between impregnated and dry aramids begins to be noticed due to the effect of STF behaving like a solid when an impact occurs.

The results at high strain rates (10m/s), display higher residual energy values than the low strain rate. Unlike the dry aramids, the impregnated aramids change their behaviour considerably when submitted to high impact loads becoming more stiff and resistant to penetration. The models adopted are also from a power law and has a significant sensitivity to layer stacking that wanes as the number of stack layers' increases.

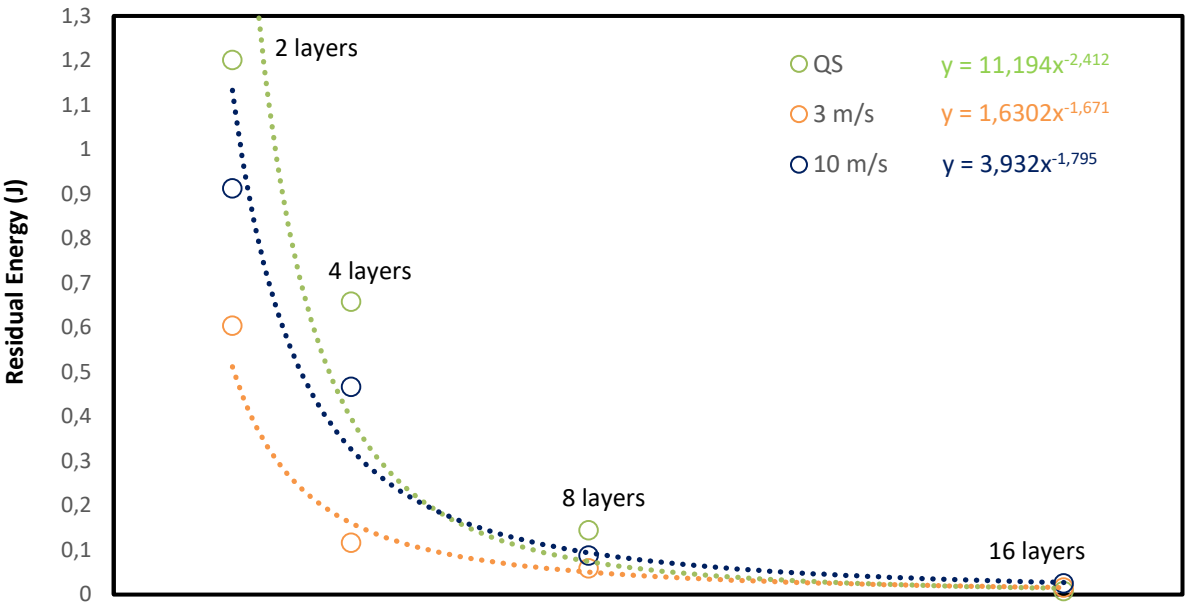

Figure 4.15 - Evolution of the residual energy with the ply number for quasi-static, low strain rate (3m/s) and high strain rate (10m/s) conditions with impregnated aramids.

Comparing both results of residual energy for dynamic loads (the *quasi-static* conditions are similar to both types of aramids, so it is irrelevant to compare them), it is shown in figure 4.18 that the impregnated aramids display, as explained before, considerable inferior values than the dry aramids, particularly for fewer layers and high strain rates. Also interesting to highlight that the difference is meaningful in such a way that the residual energy at 3m/s with dry aramid fabric is superior than 10m/s condition with impregnated ones. Proving that the STF agent has an increasing significant impact on energy absorption capabilities of aramid fabric materials for higher strain rate conditions at relatively low ply numbers.

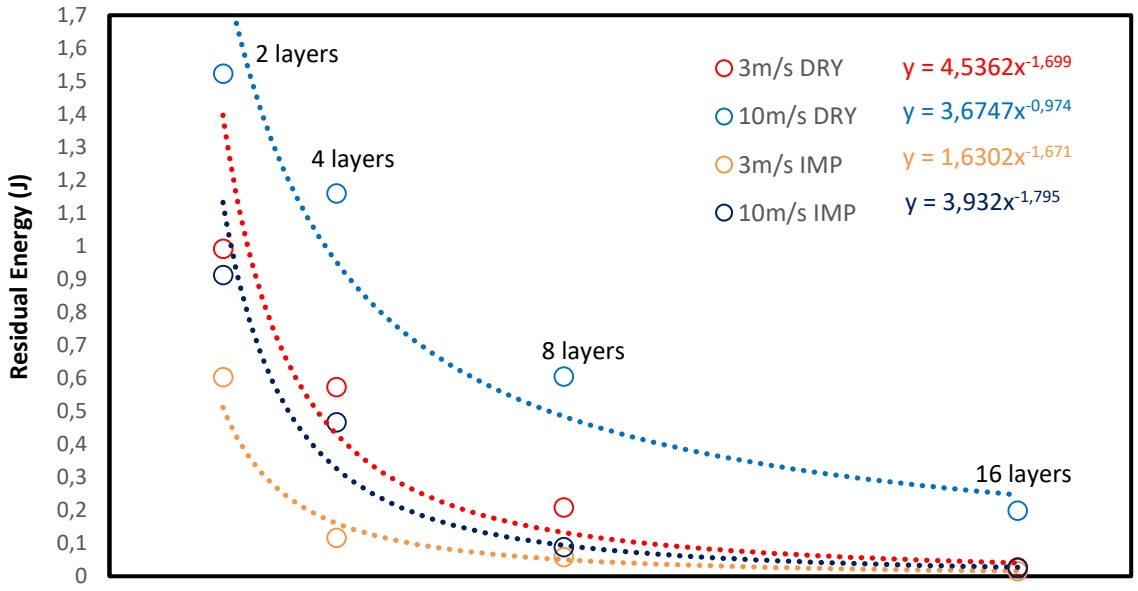

Figure 4.16 - Comparison between dry and impregnated aramids residual energy for low strain rate (3m/s) and high strain rate (10m/s).

5. Conclusions and Future Perspectives

This chapter seeks to highlight the key points of experimental work as well as the conclusions drawn from the experimental results and the importance of cognitive development of this matter both in the engineering and military perspective. It is also mentioned possible improvements and some suggestions that may be made in the SHPB experimental apparatus in order to improve its efficiency and results, as has been practiced in IST over the years. Likewise, the experimental methods can still be improved for better measurements and results

5.1. Conclusions

The project and construction of an impact and compression-testing machine, based on a split-Hopkinson pressure bar, allowed testing the impact and compression behaviour of different materials between plates in dynamic and *quasi-static* conditions, with distance, velocity and load sensors, allowing the detection the impact velocity, the load applied to the sample and its strain.

The results from the experiments executed on the machine allow the draw of some conclusions related to the relation between the aramid material type and the characteristics of the terminal ballistic moment.

The experiments consist in the analysis of the compressive behaviour of dry and impregnated plain-woven aramid fabrics at low and high strain rates and *quasi-static* conditions and layer sets of 2, 4, 8 and 16 layers. The results showed that, for dry aramids, the increase of peak force with the ply number was only observed for *quasi-static* conditions, unlike dynamic impacts, where the peak force remains constant. Although, the impregnated aramids displayed considerably smaller peak force in dynamic impact values, as variations within the ply-numbers, due to the STF effect in which the material becomes stiff and increases its high resistant on impact.

Despite the strain rate conditions, the increase of the ply number showed a higher energy absorption capability in both dry and impregnated aramids by displaying smaller residual energy values. The impregnated aramids, naturally, displayed smaller values of residual energy due to the STF effect explained previously.

It was also observed, especially with impregnated aramids, that the strain rate sensitivity was more pronounced in smaller ply numbers, becoming negligible at higher layer sets.

The behavior of the residual energy curves showed an asymptotic behaviour that allows the establishment of empirical models that describe in a simpler way the influence of the impact parameters in the residual energy.

5.2. Future Perspectives

Given the follow-up to experimental studies developed from a SHPB based machine, several changes were made, described throughout the work, which allowed impacts with higher energy, higher velocities, better analysis of results, etc. However, changes in the apparatus and methods developed in this study are not disregarded, in order to address existing flaws and other needs or adaptations.

In the development of the split-Hopkinson pressure bar based machine, it was sought to extend the variety of the tests with the introduction of a muffle that increased the surrounding environment temperature of the specimen. However, with the introduction of coils and the support structure of the high-speed camera, the use of muffle became incompatible. The development of a system allows the compatibility between these components will be one of the future challenges in order to follow up the improvement of the project, such as the restructuring of the camera support.

The projectile velocity sensor is designed to connect to a two-input oscilloscope, which ultimately occupies a significant space and makes it impractical to measure velocities. The reformulation of the electrical circuit of the receptor photodiodes by placing them in parallel, with one output only, allows the existence of one signal only that is variable with the passage of the projectile by the two pairs of sensors. The period between these two signal variations will allow the calculation of the projectiles velocity. In this configuration the use of a smaller oscilloscope (with only one BNC input), turns measurements in a more practical procedure.

The machine was also built to allow the setup of a muffla in order to change the temperature conditions of the sample during the impact. This can be extremely useful when the considered real environment has a temperature higher than the room temperature. A set of changes in the impact zone can allow the assemble of that muffla in a way that will permit the impact tests within its chamber.

The projected machine allows for the characterization of bulletproof vests materials respecting the impact of projectiles. However, the development of this method should allow not only the characterization of a bulletproof vest material, but the structure as whole. For that, it is required to build a support mechanism that could hold the vest in place so it could be submitted to the same load the samples were in these experiments, in different points of the vest, allowing to identify the strongest and weakest points of it.

6. References

[1] Martins, P., Rodrigues, J., Tecnologia Mecânica: Tecnologia da Deformação Plástica. Volumes I e II, Escolar Editora, 2005.

[2] Silva, Carlos, "Caracterização Mecânica e à fratura de materiais aplicada a processos de deformação plástica e corte", PhD in Mechanical Engineering, Instituto Superior Técnico, Universidade Técnica de Lisboa, 2013.

[3] https://www.dupont.com/why-kevlar.html (consultado a 17/11/2019).

[4] P. da S. Monteiro, *Avaliação do Desempenho de Blindagens na Protecção de Pessoas e Equipamentos*, Instituto Superior Técnico, 2007.

[5] K. Bilisik, "Three-dimensional braiding for composites: a review**",** Text Res J, 83 (13), pp. 1414-1436, 2013.

[6] Zhang, D.; Sun, Y.; Chen L.; Zhang, S.; Pan, N., *Influence of fabric structure and thickness on the ballistic impact behavior of Ultrahigh molecular weight polyethylene composite laminate*, Materials & Design 54, 315-322, 2014.

[7] A. B. de Morais, A. G. de Magalhães, and M. F. de S. F. Moura, *Materiais Compósitos - Materiais, Fabrico e Comportamento Mecânico*, Vol. 2. Porto: Publindústria, Edições Técnicas, 2011.

[8] Kumar, Bandaru Aswani e Suhail Ahmad., "Numerical simulation of progressive damage in laminated composites due to ballistic impact". Em *Safety, Reliability, Risk and Life-Cycle Performance of Structures and Infrastructures*, 4375-4382. CRC Press, 2013.

[9] J.Santos, "Métodos de Análise de Impactos Balísticos", Faculdade de Engenharia da Universidade do Porto, Fevereiro 2016.

[10] Bernardi, S., "Avaliação do comportamento de materiais compósitos de matrizes cimentícias reforçadas com fibra de aramida Kevlar". Dissertação (mestrado em engenharia civil) UFRGS, Porto Alegre, 2003.

[11] Yang, H. H., *Kevlar aramid fiber*. John Wiley & sons Ltd, 1993.

[12] "HOSDB Body Armour Standards for UK Police (2007), Part 3: Knife and Spike Resistance 39-07-C", The Home Office, 2016.

[13] Pike, John. "Personnel Armor System for Ground Troops (PASGT) Vest", 2017.

[14] http://www.cbc.com.br/ (Accessed: 18/11/2019).

[15] https://www.forgottenweapons.com/ (Accessed: 05/02/2020).

[16]http://www2.dupont.com/Kevlar/en_US/assets/downloads/KEVLAR_Technical_Guide.pdf(Accessed: 02/12/2019).

[17] Johannes Karl Fink, *High Performance Polymers*, 2nd ed., 2014.

[18] Y.Abdin, A.Jain, S.V.Lomov, V.Carvelli, *Fatigue analysis of carbon, glass and other fibers*, 29 May 2015.

[19] F. Duarte,"Caracterização e Modelação do Comportamento de Blindagens Balísticas", Instituto Superior Técnico, 2019.

[20] J.Mestre, "Análise Numérico-Experimental de Blindagens Balísticas", Instituto Superior Técnico, Novembro 2015.

[21] J. A. et al. Zukas, *Impact Dynamics*, J. Wiley, 1982.

[22] J.Justo, "Estudo do Comportamento ao Impacto de Alta Velocidade de Estruturas em Materiais Compósitos", Faculdade de Engenharia da Universidade do Porto, 1996.

[23] S. S. Morye, P. J. Hine, R. A. Duckett, D. J. Carr, and I. M. Ward, "Modelling of the energy absorption by polymer composites upon ballistic impact," in *Composites Science and Technology*, Leeds: Elsevier, p. Pages 2631-2642, 2000.

[24] SILVA, Ten. Cor. Cav. Rodrigues da, *Munições de Armas Ligeiras*, Elementos de Armamento, Academia Militar, 2004/2005.

[25] J. M. d. C. R. Pereira, *Desenvolvimento e fabrico de compósitos de matriz polimérica com fibras naturais*, 2017.

[26] I. G. Crouch, "4 - Laminated materials and layered structures," *Sci. Armour Mater. Woodhead Publ.*, pp. 167–201, 2017.

[27] D. J. Carr and C. M. Crawford, "4 - Fabrics and composites for ballistic protection A2 - Chen, X," in *Advanced Fibrous Composite Materials for Ballistic Protection*, Woodhead, pp. 109–119, 2016.

[28] M. Pasquali, C. Terra, and P. Gaudenzi, "Analytical modelling of high-velocity impacts on thin woven fabric composit targets," in *Composite Structures*, pp. 951–965, 2015.

[29] Naik, N. K., S. Kumar, D. Ratnaveer, M. Joshi e K. Akella. "An energy-based model for ballistic impact analysis of ceramic-composite armors". *International Journal of Damage Mechanics* no. 22 (2):145-187, 2013.

[30] "Wadley Research Group - UVA", 2016.

[31] https://www.nts.com/services/testing/defense/ballistics/ (Accessed: 12/01/2020).

[32] Kneubuehl, B.P., *Ballistic Protection*, Switzerland, 2003.

[33] Carlucci, D.E.; Jacobson, S.S., *Ballistics: theory and design of guns and ammunition*. CRC Press, 2010.

[34] MIL-STD-662F, MILITARY STANDARD: V50 BALLISTIC TEST FOR ARMOR (18 DEC 1997).

[35] Cunniff, P. M., "Dimensionless parameters for optimization of textile-based body armor systems.", 18th International Symposium on Ballistics: 1303–1310, 1999.

[36] J.Pinto, “Avaliação do Comportamento Mecânico de Blindagens Balísticas”, Instituto Superior Técnico, Setembro 2009.

[37] STANAG 4190, *Test Procedures for Measuring Behind–Armour Effects of Anti–Armour Ammunition*, 1999.

[38] http://www.defenshield.com/pdf/NIJ010104.pdf (Accessed: 02/02/2020).

[39] T. L. Chu, C. Ha-Minh, and A. Imad, “Analysis of local and global localizations on the dailure phenomenon of 3d interlock woven fabrics under ballistic impact,” *Compos. Struct.*, pp. 267–277, 2016.

[40] N. Nayak, A. Banerjee, and T. R. Panda, “Numerical study on the ballistic impact response of aramid fabric-epoxy laminated composites by armor piercing projectile,” *Procedia Eng.*, pp. 230–237, 2016.

[41] https://www.luckygunner.com/labs/self-defense-ammo-ballistic-tests/ (Accessed: 05/02/2020).

[42] Mohotti, Damith, Tuan Ngo, Sudharshan N. Raman e Priyan Mendis. "Analytical and numerical investigation of polyurea layered aluminium plates subjected to high velocity projectile impact". *Materials & Design* no. 82:1-17, 2015.

[43] http://www.hpwhite.com/resources/ (Accessed: 10/02/2020).

[44] R. Zaera, T. Liu, N. He, and G. Jia, “Analytical modelling of two finite element modelling approaches for ballistic impact response of composite laminates.,” *Int. J. Impact Eng.*, pp. 133–148, 1998.

[45] M. A. G. Silva, C. Cismaşiu, and C. G. Chiorean, “Numerical simulation of ballistic impact on composite laminates,” *Int. J. Impact Eng.*, vol. 31, no. 3, pp. 289–306, 2004.

[46] V. Bodepati, K. Mogulanna, G. S. Rao, and M. Vemuri, “Numerical simulation and experimental validation of e-glass/epoxy composite material under ballistic impact of 9mm soft projectile,” *Procedia Eng.*, pp. 740–746, 2016.

[47] T.Pires, “Barra de Pressão de Hopkinson Conceção e Desenvolvimento de um Projeto de uma Barra de Pressão de Hopkinson para Realização de Ensaios Mecânicos”, Escola Naval, Alfeite, 2016.

[48] https://www.relinc.com/pt/split-hopkinson-bar-kolsky-bars/split-hopkinson-bar/ (Accessed: 20/02/2020).

[49] R.Kist, “Dimensionamento de uma Barra de Hopkinson para Ensaios de Alta Velocidade de Deformação em Plásticos Dúcteis”, Porto Alegre, Julho 2014.

[50] Chen, W., & Song, B., *Split Hopkinson (Kolsky) Bar Design, Testing and Applications.* New York: Springer. 2011.

[51] Ramesh Kaliat T. *High Rates and Impact Experiments.* Springer Handbook of Experimental Solid Mechanics, 2008.

[52] Ferreira, F. J., *Análise do Comportamento Dinâmico de Componentes Estruturais sob Solicitações Generalizadas.* Porto: Tese de Doutoramento apresentada na Faculdade de Engenharia da Universidade do Porto, 2003.

[53] *Split Hopkinson Pressure Bar Apparatus - An Historic Mechanical Engineering Landmark.,* San Antonio, Texas: Southwest Research Institute, 2006.

[54] Gray, G.T. III. An Investigation of the Mechanical Properties of Materials at High Rates of Loading, ASM *Handbook,* Vol.8, pp. 462-476, 1998.

[55] A.Gregório, "Ensaios de Impacto e Elevadas Velocidades de Deformação", Instituto Superior Técnico, 2017.

[56] A. G. Bazle, J. W. Gillespie, "Numerical Hopkinson bar analysis: uni-axial stress and planar bar-specimen interface conditions by design", Report MD 21005–5069, ARL-CR-553, Army Research Laboratory, Aberdeen Proving Ground, 2004.

[57] P. Santos, "Ensaios de Compressão Uniaxial: Desenvolvimento de Máquina e Aplicação a Metais e Ligas Metálicas", Instituto Superior Técnico, 2019.

[58] Tanveer Malik & Shyam Barhanpurkar, "*Ballistic Protection Fabric*", Department of Textile Technology Shri Vaishnav Institute of Technology and Science, 2018.

[59] Zhenquian Lu, Zishun Yuan, Xiaogang Chen, Jiawen Qiu, "*Evaluation of ballistic performance of STF impregnated fabrics under high velocity impact*", 2019.

[60] Y.S. Lee, E.D. Wetzel, N.J. Wagner "*The ballistic impact characteristics of Kevlar® woven fabrics impregnated with a colloidal shear thickening fluid*", J Mater Sci, 38, pp. 2825-2833, 2003.

[61] I.R. Peters, S. Majumdar, H.M. Jaeger, "*Direct observation of dynamic shear jamming in dense suspensions***"** Nature, 532, 2016.

[62] E. Brown, H.M. Jaeger, "*Shear thickening in concentrated suspensions: phenomenology, mechanisms and relations to jamming***"**, Rep. Prog. Phys., 77, 2014.

[63] T.A. Hassan, V.K. Rangari, S. Jeelani, "*Synthesis, processing and characterization of shear thickening fluid (STF) impregnated fabric composites*" Mater Sci Eng A, 527 (12), pp. 2892-2899, 2010.

[64] M.J. Decker, C.J. Halbach, C.H. Nam, N.J. Wagner, E.D. Wetzel, "*Stab resistance of shear thickening fluid (STF)-treated fabrics*", Compos Sci Technol, 67 (3–4), pp. 565-578, 2007.

[65] Z. Lu, L. Wu, B. Gu, B. Sun, "*Numerical simulation of the impact behaviors of shear thickening fluid impregnated warp-knitted spacer fabric*", Compos Part B Eng, 69, pp. 191-200, 2015.

[66] E. Brown, N.A. Forman, C.S. Orellana, H. Zhang, B.W. Maynor, D.E. Betts, *et al., "Generality of shear thickening in dense suspensions***"**, Nat Mater, 9 (3), pp. 220-224, 2010.

[67] Y. Lee, N. Wagner, "*Dynamic properties of shear thickening colloidal suspensions***",** Rheol Acta, 42 (3), pp. 199-208, 2003.

[68] T. Kang, K. Hong, M. Yoo, "*Preparation and properties of fumed silica/Kevlar composite fabrics for application of stab resistant material***"**, Fibers Polym, 11 (5), pp. 719-724, 2010.

[69] SEAS Fuel cell and fuel system. Available at: *http://www.formula1dictionary.net/fuel_cell.html* (Accessed: 18/05/2020).

[70]*https://www.goodyear.com/images/tireImages/goodyear/media/Wrangler_All_Terrain_Adventure_Cutaway1_2732.jpg* (Accessed: 18/05/2020).

[71] *http://www.applied-fiber.com/kevlar-rope-assemblies/kevlar-cable* (Accessed: 18/05/2020).

[72] Mulat Alubel Abtew, François Boussu, Pascal Bruniaux, Carmen Loghin, Irina Cristian, "*Ballistic Impact Mechanisms – A Review on Textiles and Fibre-reinforced Composites Impact Responses*", September 2019.

[73] H. Talebi, S.V. Wong, A.M.S. Hamouda, "*Finite element evaluation of projectile nose angle effects in ballistic perforation of high strength fabric***",** Compos Struct, 87 (4), pp. 314-320, 2009.

[74] A. Rajagopal, N.K. Naik, "*Oblique ballistic impact behavior of composites***"**, Int J Damage Mech, 23 (4), pp. 453-482, 2014.

[75] B.A. Cheeseman, T.A. Bogetti, "*Ballistic impact into fabric and compliant composite laminates***",** Compos Struct, 35 (18), pp. 161-173, 2003.

[76] C.K. Chu, Y.L. Chen, G.C. Hseu, D.G. Hwang, "*The study of obliquity on the ballistic performance of basket fabric composite materials***",** J Compos Mater, 41 (13), pp. 1539-1558, 2007.

[77] N.V. David, X.-L. Gao, J.Q. Zheng, "*Ballistic resistant body armor: contemporary and prospective materials and related protection mechanisms***",** Appl Mech Rev, 62 (5), Article 050802, 2009.

[78] R.E. Wittman, R.F. Rolsten, "*Armor, – of Men and Aircraft***",** 12th National SAMPE Symposium, SAMPE, 1967**.**

Attachments

A.1 – Table of properties of different brands of fibers of ballistic vests [Duarte, 2019].

	Density (kg/m³)	***Modulus of Elasticity (GPa)***	***Rupture Tension (MPa)***	**Rupture deformation (%)**
Kevlar®29	1440	60	3000	3,6
Kevlar®49	1450	129	3000	1,9
Twaron®	1440	60	2600	3
Spectra®1000	970	145	3000	3,2
Spectra®900	970	115	2500	4
Dyneema® SK60	970	89	2700	3,5
Dyneema® SK65	970	95	3000	3,6
Dyneema® SK66	970	99	3200	3,7

A.2 - Ballistic protection levels STANAG 4569 [Monteito, 2007].

Level	**Threat**	**Projectile**	**Distance (m)**	**Speed (m/s) (±20m/s tolerance)**
I	Shotgun	7.62x51 NATO Ball (Ball M80) 5.56x45 NATO SS109 5.56X45 M193	30	833 (M80) 900 (SS109) 937 (M193)
II	Shotgun	7.62x39API BZ	30	695
III	Shotgun	7.62x51 AP(WC core) 7.62x54R B32 API (Dragunov)	30	930 (51 AP) 854 (54R)
IV	Heavy machine gun	14.5x114AP/B32	200	911
V	Autocannon	25mm APDS-TM-791 ou TLB 073	500	1258
VI	Autocannon	30mm: APFSDS ou AP	500	1430

A.3 - Classification of ballistic vests by protection level according to NIJ0101.04 (*Defenseshield – NIJ0101.04*).

NÍVEL DE PROTEÇÃO	TIPO DE MUNIÇÃO calibres	CARACTERÍSTICA DA MUNIÇÃO				CONDIÇÕES DE USO
		Peso		Velocidade		
		g	gr.	m/s	ft/s	
NÍVEL IIA	9 mm FMJ RN	8.0	124	341	1120	USO PERMITIDO
	.40 S&W fmj	11.7	180	322	1055	
NÍVEL II	9 mm FMJ RN	8.0	124	367	1205	
	.357 MAG JSP	10.2	158	436	1430	
NÍVEL IIIA	9 mm FMJ RN	8.2	124	436	1430	
	.44 MAG JHP	15.6	240	436	1430	
NÍVEL III	7.62 mm NATO FMJ	9.6	148	838	2780	USO RESTRITO Somente para o Exército
NÍVEL IV	.30 M2 AP	10.8	166	869	2880	

A.4 - *Classification of ballistic vests by protection level according to NIJ0101.04 (Kneubuehl, 2003).*

Type of weapon	Caliber	Projectile weight (g)	Test speed (m/s)	Energy (J)	Energy density (J/mm^2)
Short Arms	9mm Luger	8,0	410	670	10,5
	357 Magnum	10,2	430	940	14,8
	44 Rem. Mag.	15,5	440	1500	15,2
Long Weapons	5,56mm NATO	4,0	935	1750	72,8
Armed Forces	7,62mm NATO	9,5	830	3270	71,8
	7,5mm GP 11	11,3	780	3440	76,8
Long Weapons	7mm Rem.Magnum	10,5	960	4840	125,7
Hunting	8x68S	12,7	920	5375	106,9
Rifles	12/70	31,4	425	2860	10,6

Operating conditions of variac TDGC2 - 10KVA

- Relative humidity 90% at 25ºC;
- Room temperature from -15°C to +40°C;
- Must be installed in places free of moisture, dust and away from explosive or corrosive chemicals;
- Must be stored, transported and installed in level places free of excessive vibration or collision;
- Sheltered use.
- Due to the current intensity limit provided by the network, the voltage used by variac should not exceed 120V.

Figure 1 - variac TDGC2 - 10KVA.Pa

Oven KONN GmbH - Procedure

1. For safety reasons, the variac must have the voltage value at 0 before making any connection;

2. The oven is connected to the variac TDGC2 – 10KVA, which in turn is connected to the mains using a single-phase 16A plug. The connections between the variac and the oven must be made by connecting the oven cables (brown and blue) to the right (OUTPUT) and the power plug on the left (INPUT) - see Figure 2. Make sure that the orientation of the cables of different colors is correct as shown in figure.

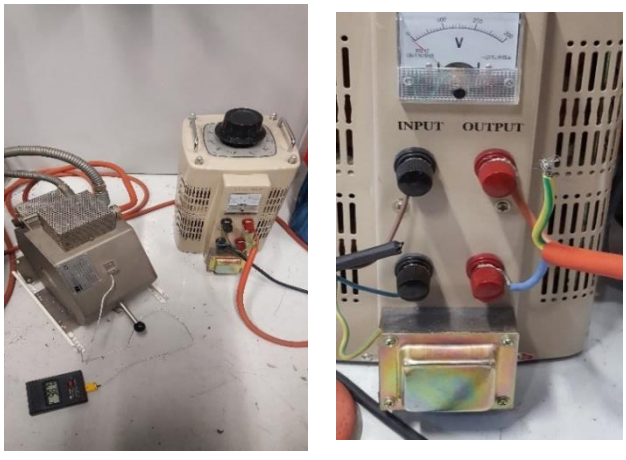

Figure 2 - Mounting diagram between the variac and the

3. When the connections between the oven and the variac are made it is safe to connect the power plug taking care not to touch the terminals while it is connected;

4. The temperature variation of the oven must be made through the variation of voltage of the variac, serving as orientation the calibration curve presented in Figure 3**;**

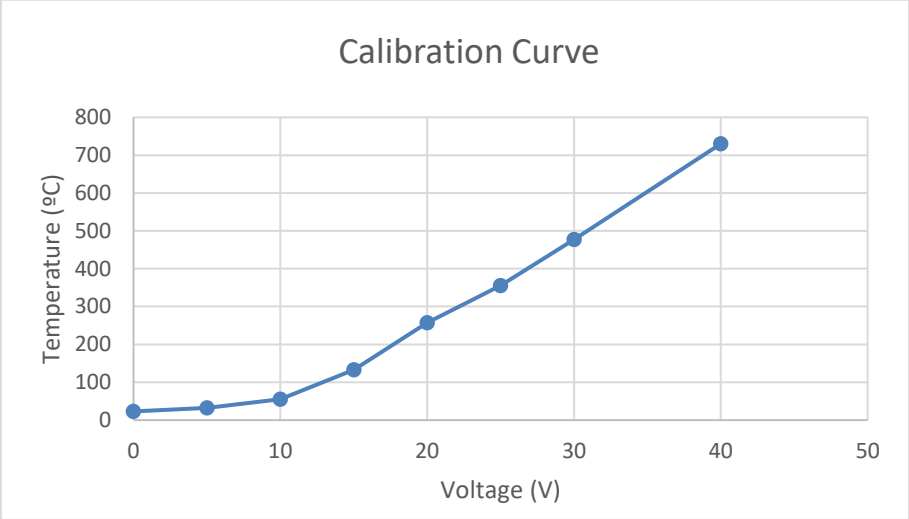

Figure 3 - Variac voltage calibration curve with the oven temperature.

5. The variac voltage should never exceed 120V to prevent the switchboard to be “turned down”.

6. When the test is complete, set the variac voltage to zero and disconnect the power plug, placing it near the variac so that the cables are not interlaced or interfere with the other connections of the variac.

NOTE: The tests for the construction of the calibration curve were carried out in a time interval of 5 minutes from room temperature (21-25ºC) at a given voltage by measuring the temperature inside the oven at the end of that time intervlo with a thermocouple.

Time Measurement in Agilent Technologies Oscilloscope, Model DSO1004A

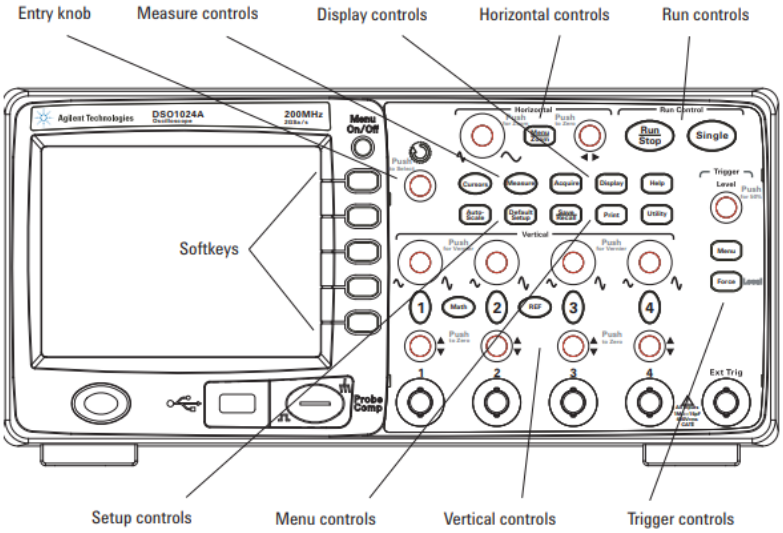

In order to capture the voltage variations on the oscilloscope screen and measure the time period between two voltage variations of different channels, the following steps should be followed, assuming that the device is connected to the electric current and activated:

1) When channel 1 and 2 are connected, adjust the position of the signals in "Position knobs" on the screen to be easily distinguished and adjust the voltage range in "Scale knobs" so that voltage variations are easily visible.

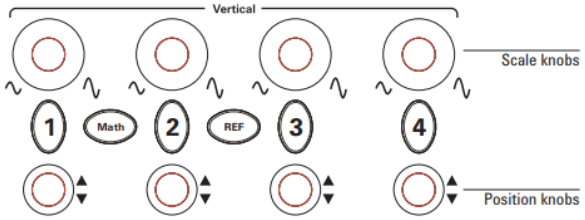

2) Adjust the range of the wave period in "Scale knob" and its position in "Position knob" to be indicated for measurements.

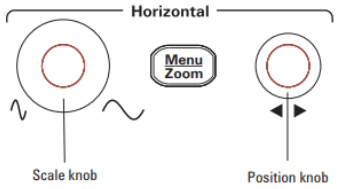

3) Press "Menu" to set "Trigger" conditions.

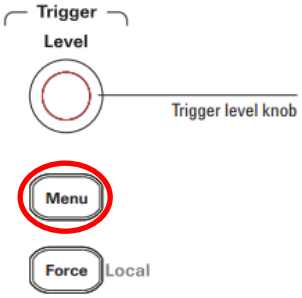

4) Select on screen (using softkeys) in "Slope", "Falling edge" and "Sweep", "Normal".

	Rising edge.
	Falling edge.
	Both rising and falling edges.

5) Considering the "Trigger level knob", adjust the trigger level to one of the signals so that when the voltage variation in this signal occurs, it exceeds this level so that the oscilloscope captures that moment.

6) When ready to perform the test, press the "Single" button to prepare the equipment for the occurrence of.

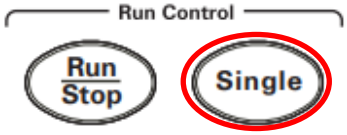

7) As soon as the voltage variations on both signals are detected, the image of the signals is captured. To measure the amount of time between them, press the "Cursors" button.

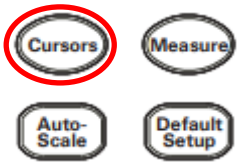

8) Select on screen (using softkeys) under "Mode", "Manual".

9) Two bars will appear on the screen, as shown in the figure below (left) in red. Select "Cur A: ↻" and "Cur B: ↻" depending on the line you want to move. To move the lines, rotate the button/wheel next to the "Cursors" and "Auto-Scale" buttons, as shown below (right) in red. Align the bars so that they are about the moment of voltage variance of each of the signals

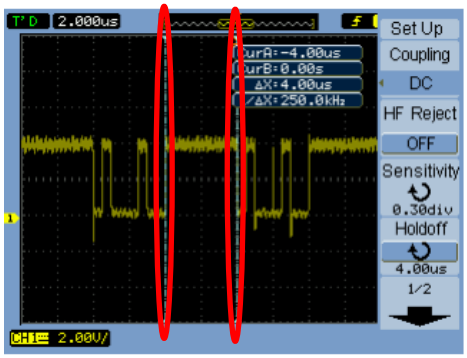

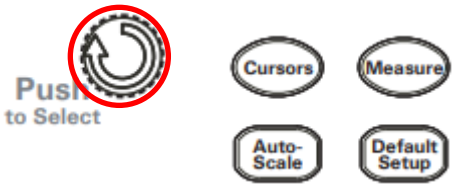

10) Finally, you get the value of $|\Delta x|$ on the image screen above, which represents the period of time between the signal variation in channel 1 and the signal variation in channel 2, i.e., the time period between the time the projectile interrupts the beam of light that reaches the first receiving photodiode and the moment it interrupts the second, thus determining the time it takes for the projectile to travel a known distance, calculating the speed of the projectile